University of Surrey
Faculty of Engineering and Physical Sciences
Department of Computing

Computing Sciences Report
PhD Thesis

# Estimation of Single Trial ERPs and EEG Phase Synchronization with Application to Mental Fatigue

by

## Delaram Jarchi

Supervisor: Dr Saeid Sanei

Surrey, 2011

*To my parents who grew me up without any expectation*

# Abstract

Monitoring mental fatigue is a crucial and important step for prevention of fatal accidents. This may be achieved by understanding and analysis of brain electrical potentials. Electroencephalography (EEG) is the record of electrical activity of the brain and gives the possibility of studying brain functionality with a high temporal resolution. EEG has been used as an important tool by researchers for detection of fatigue state. However, their proposed methods have been limited to classical statistical solutions and the results given by different researchers are somehow conflicting. Therefore, there is a need for modification of the existing methods for reliable analysis of mental fatigue and detection of fatigue state. In addition to the raw EEG, event related potentials (ERPs), which are direct measures of brain responses to the specified stimuli, have been used in mental fatigue analysis since the attention related ERPs have shown to be effective for detection of fatigue state. In this study we aim to extend and further develop the existing signal processing methods for EEG- and ERP-based mental fatigue analysis.

First, a new approach is proposed for measuring synchronization of EEG oscillations in different frequency bands across brain regions. The approach is used to find the relevant and effective features for detection of the fatigue state. It uses adaptive methods such as empirical mode decomposition (EMD) and adaptive line enhancer (ALE) for extracting and de-noising the EEG oscillations. Then, Hilbert transform (HT) is used for computing the linear and non-linear synchronization measures. A new method based on particle filtering (PF) is proposed for direct estimation of instantaneous phase of an oscillation. This method can be developed more in future studies for phase synchronization analysis of the EEG oscillations before and during the fatigue state.

ERP subcomponents are estimated using PF. Based on the proposed method, ERP subcomponents are separated in temporal domain across different trials and their inter-trial variability is tracked using a coupled PF. The method is applied to mental fatigue data to show the potential use of the method in ERP subcomponent estimation for detection of fatigue state. Then, a new spatio-temporal filtering is designed for estimation of the correlated ERP subcomponents. The method is robust against both temporal and spatial correlations of the ERP subcomponents. It is compared to the existing methods in different scenarios and its superiority is confirmed by using simulated signals. It is also applied to real data to show its potential use in ERP subcomponent estimation.

Finally, an auditory based paradigm is implemented to evaluate the effectiveness of the designed mental fatigue detection system. By applying the proposed methods for estimation of single trial P300 subcomponents and EEG phase synchronization, it is demonstrated that the proposed auditory paradigm can be effectively used in a mental fatigue detection system.

# Acknowledgements

I would like to thank Dr. Sanei, my supervisor, for his many valuable suggestions and continuous support during this research. His enthusiastic supervision, invaluable input, great encouragement have provided a wonderful basis for the present study. I very much appreciate his support from the beginning in all the aspects.

I am thankful to Prof. Principe at University of Florida and Dr. Lorist at Groningen University, Netherland for their valuable comments about ERP detection and mental fatigue analysis respectively. I am also thankful to Mr Dean at the Department of Psychology, University of Surrey, for his help in EEG recording. I am also thankful to the Leverhulme Trust for its financial support.

Guildford, Surrey
June 2011

Delaram Jarchi

# Table of Contents

# List of Publications

## Journal

[1] **D. Jarchi**, S. Sanei, J. C. Principe and B. Makkiabadi, "A new spatiotemporal filtering method for single-trial estimation of correlated ERP subcomponents", IEEE Transactions on Biomedical Engineering, Volume 58, Issue 1, January 2011.

[2] **D. Jarchi**, S. Sanei, H. R. Mohseni, and M. M. Lorist, "Coupled particle filtering: A new approach for P300-based analysis of mental fatigue", Journal of Biomedical Signal Processing and Control, Volume 6, Issue 2, April 2011.

## Conference

[1] **D. Jarchi**, B. Makkiabadi, and S. Sanei, "Instantaneous phase tracking of oscillatory signals using EMD and Rao-blackwellised particle filtering", In proc. IEEE International Conf. on Acoustic, Speech and Signal Processing, ICASSP 2011, Prague, Czech Republic.

[2] **D. Jarchi**, B. Makkiabadi, and S. Sanei, "A new spatiotemporal filtering method for single trial ERP subcomponent estimation", In proc. European Signal Processing Conference, EUSIPCO 2010, Aalborg, Denmark.

[3] **D. Jarchi**, B. Makkiabadi, and S. Sanei, "Mental fatigue analysis by measuring synchronization of brain rhythms incorporating empirical mode decomposition", In proc. 2nd International Workshop on Cognitive Information Processing, CIP 2010, Elba, Italy.

[4] **D. Jarchi**, B. Makkiabadi, and S. Sanei, "Estimation of trial to trial variability of P300 subcomponents by coupled Rao-blackwellised particle filtering", In proc. IEEE Workshop on Statistical Signal Processing, SSP 2009, Cardiff, UK.

[5] **D. Jarchi**, and S. Sanei, "Source Localization of Brain Rhythms by Empirical Mode Decomposition and Spatial Notch Filtering" In proc. European Signal Processing Conference, EUSIPCO 2009, Glasgow, Scotland.

[6] **D. Jarchi**, B. Makkiabadi, and S. Sanei, "Separating and tracking ERP subcomponents using constrained particle filter," In proc. 16th Int. Conf. on Digital Signal Processing, DSP 2009, Santorini, Greece.

# Contribution as Co-author

# Journal

[1] J. Escudero, S. Sanei, **D. Jarchi**, D. Abasolo and R. Hornero, "Regional coherence evaluation in mild cognitive impairment and Alzheimer's disease based on adaptively extracted magnetoencephalogram rhythms", Physiological measurement, Volume 32, Issue 8, August 2011.

# Conference

[1] B. Makkiabadi, **D. Jarchi** and S. Sanei, "Simultaneous localization and separation of biomedical signals by tensor factorization", In proc. IEEE Workshop on Statistical Signal Processing, SSP 2009, Cardiff, UK.

[2] B. Makkiabadi, A. Sarrafzadeh, **D. Jarchi**, V. Abolghasemi and S. Sanei, "Semi-blind signal separation and channel estimation in MIMO communication systems by tensor factorization", In proc. IEEE Workshop on Statistical Signal Processing, SSP 2009, Cardiff, UK.

[3] V. Abolghasemi, **D. Jarchi**, and S. Sanei, "A robust approach for optimization of measurement matrix in compressive sensing", In proc. 2nd International Workshop on Cognitive Information Processing, CIP 2010, Elba, Italy.

[4] B. Makkiabadi, **D. Jarchi**, V. Abolghasemi, and S. Sanei, "A Time Domain Geometrically Constrained Multimodal Approach for Convolutive Blind Source Separation", In proc. EUSIPCO 2011, Barcelona, Spain.

[5] B. Makkiabadi, **D. Jarchi** and S. Sanei, "Blind Separation and Localization of Correlated P300 Subcomponents Subcomponents from Single Trial Recordings using Tensor Model", In proc. EMBC 2011, Boston , MA, USA.

# List of Tables

# List of Figures

# List of Abbreviations

| | |
|---|---|
| **ALE** | Adaptive Line Enhancer |
| **ApEn** | Approximate Entropy |
| **BCI** | Brain-Computer Interface |
| **BSS** | Blind Source Separation |
| **CRBPF** | Coupled RBPF |
| **ECoG** | Electrocorticography |
| **EEG** | Electroencephalography |
| **EMD** | Empirical Mode Decomposition |
| **EOG** | Electro-oculogram |
| **ERP** | Event Related Potential |
| **ERS** | Event Related Synchronization |
| **fMRI** | Functional Magnetic Resonance Imaging |
| **HMM** | Hidden Markov Model |
| **HS** | Hilbert Spectrum |
| **HT** | Hilbert Transform |
| **IA** | Instantaneous Amplitude |
| **ICA** | Independent Component Analysis |
| **IF** | Instantaneous Frequency |
| **IMF** | Intrinsic Mode Function |
| **IP** | Instantaneous Phase |
| **Kc** | Kolmogorov Complexity |
| **KF** | Kalman Filtering |
| **KPCA** | Kernel Principal Component Analysis |

| | |
|---|---|
| **LMS** | Least Mean Square |
| **MAP** | Maximum A Posteriori |
| **MEG** | Magnetoencephalography |
| **MSE** | Mean Square Error |
| **PCA** | Principal Component Analysis |
| **PET** | Positron Emission Tomography |
| **PF** | Particle Filtering |
| **RBPF** | Rao-Blackwellized Particle Filtering |
| **RF** | Random Forests |
| **SNR** | Signal to Noise Ratio |
| **SQUID** | Super Conducting Interference Device |
| **SVD** | Singular Value Decomposition |
| **WGN** | White Gaussian Noise |

# Nomenclatures

| | |
|---|---|
| $a_i(t)$ | Instantaneous amplitude of $i^{th}$ IMF at time $t$ |
| $a_t(i)$ | Instantaneous amplitude of $i^{th}$ IMF at time $t$ |
| $a_k(i)$ | Amplitude of $i^{th}$ subcomponent at trial $k$ |
| $a_k^i$ | Amplitude of P3a in $k^{th}$ trial of $i^{th}$ RBPF |
| $a_t^{(n)}$ | Instantaneous amplitude of $n^{th}$ particle at time (trial) $t$ |
| $a_k^{(n)_i}$ | $n^{th}$ particle for amplitude of P3a in $k^{th}$ trial of $i^{th}$ RBPF |
| $\mathbf{a}_k^i$ | Linear state of $i^{th}$ RBPF at trial $k$ |
| $\mathbf{a}_1$ | Scalp projection of ERP subcomponent |
| $\mathbf{a}_2$ | Scalp projection of ERP subcomponent |
| $\widetilde{a}_k^i$ | Amplitude of P3b in $k^{th}$ trial of $i^{th}$ RBPF |
| $\widetilde{a}_k^{(n)_i}$ | $n^{th}$ particle for amplitude of P3b in $k^{th}$ trial of $i^{th}$ RBPF |
| $b_k(i)$ | Latency of $i^{th}$ subcomponent at trial $k$ |
| $b_k^i$ | Latency of P3a in $k^{th}$ trial of $i^{th}$ RBPF |
| $b_k^{(n)_i}$ | $n^{th}$ particle for latency of P3a in $k^{th}$ trial of $i^{th}$ RBPF |
| $\mathbf{b}_k$ | $k^{th}$ principal component |
| $B$ | Number of frequency bins |
| $\mathbf{B}_{k-1}(\mathbf{x}_{k-1}^1)$ | State transition for linear state variable of RBPF |
| $\widetilde{b}_k^i$ | Latency of P3b in $k^{th}$ trial of $i^{th}$ RBPF |
| $\widetilde{b}_k^{(n)_i}$ | $n^{th}$ particle for latency of P3b in $k^{th}$ trial of $i^{th}$ RBPF |
| $c$ | Normalizing constant for Gamma waveform |
| $c_i(t)$ | Analytic version of $i^{th}$ IMF at time $t$ |
| $\mathbf{C}_k(\mathbf{x}_k^1)$ | Observation transition for linear state variable of RBPF |
| $d_i(t)$ | $i^{th}$ IMF at time $t$ |
| $d_t(i)$ | $i^{th}$ IMF at time $t$ |
| $diff(.)$ | Differences between adjacent elements |
| $e(t)$ | Adaptation error of ALE at time $t$ |

| | |
|---|---|
| $exp(.)$ | Exponential function |
| $\mathrm{E}\{.\}$ | Expected value |
| $f$ | Observation transition function of PF |
| $f$ | State transition function of RBPF |
| $f_k$ | General non-linear function |
| $freq_t^{(n)}$ | Instantaneous frequency of $n^{th}$ particle at time (trial) $t$ |
| $\mathbf{F}_k$ | State transition matrix in KF |
| $\widetilde{f}$ | State transition function of RBPF |
| $G$ | Observation transition function of RBPF |
| $\widetilde{G}$ | Observation transition function of RBPF |
| $G'$ | Non-linear function |
| $h_k$ | General non-linear function |
| $h_i(k,t)$ | Hilbert transform of $i^{th}$ IMF at time $t$ and $k^{th}$ frequency bin |
| $\mathbf{H}_k$ | Observation transition matrix in KF |
| $\mathbf{H}_d[.]$ | Discrete Hilbert transform |
| $J$ | $\sqrt{-1}$ |
| $k$ | Shape parameter for Gamma waveform |
| $k_{max}$ | Number of trials |
| $\mathbf{K}_k$ | Kalman gain |
| $log(.)$ | Logarithm function |
| $M$ | Number of IMFs |
| $N_s$ | Number of particles |
| $\mathbf{n}_{k-1}$ | State noise of KF and PF |
| $\mathcal{N}(\mathbf{m},\mathbf{P})$ | Gaussian distribution with mean $\mathbf{m}$ and covariance matrix $\mathbf{P}$ |
| $\mathcal{N}(\mathbf{x};\mathbf{m},\mathbf{P})$ | Gaussian distribution with mean $\mathbf{m}$ and covariance matrix $\mathbf{P}$ evaluated at $\mathbf{x}$ |
| $p$ | Number of ERP subcomponents |
| $\mathbf{P}_k$ | Covariance matrix of linear state vector variable of RBPF at trial $k$ |
| $p(.)$ | Probability density function |
| $p(.\|.)$ | Conditional probability density function |
| $P_{signal}$ | Power of signal |
| $P_{noise}$ | Power of noise |
| $q(.)$ | Importance density function |

| | |
|---|---|
| $\mathbf{Q}_{k-1}^{w(\rho i)}$ | Covariance matrix of state noise of non-linear state variable of $i^{th}$ RBPF |
| $\mathbf{Q}_{k-1}^{w(ai)}$ | Covariance matrix of state noise of linear state variable of $i^{th}$ RBPF |
| $\mathbf{Q}_{t-1}^{w}$ | Covariance matrix of state noise of RBPF |
| $\mathbf{Q}_{t}^{v}$ | Covariance matrix of measurement noise of RBPF |
| $\mathbf{Q}_{k-1}^{n}$ | Covariance matrix of the state noise of KF |
| $\mathbf{Q}_{k}^{v}$ | Covariance matrix of the measurement noise of KF and RBPF |
| $\mathbf{Q}_{k-1}^{w}$ | Covariance matrix of state noise for linear state variable of RBPF |
| $\mathbf{r}_1$ | Temporal reference signal for ERP subcomponent |
| $\mathbf{r}_2$ | Temporal reference signal for ERP subcomponent |
| $Real(.)$ | Real part of a complex variable |
| $s_k^i$ | Width of P3a in $k^{th}$ trial of $i^{th}$ RBPF |
| $s_k^{(n)_i}$ | $n^{th}$ particle for width of P3a in $k^{th}$ trial of $i^{th}$ RBPF |
| $s_k(i)$ | Width of $i^{th}$ subcomponent at trial $k$ |
| $\widetilde{s}_k^i$ | Width of P3b in $k^{th}$ trial of $i^{th}$ RBPF |
| $\widetilde{s}_k^{(n)_i}$ | $n^{th}$ particle for width of P3b in $k^{th}$ trial of $i^{th}$ RBPF |
| $t_{max}$ | Number of time points (trials) |
| $T_s$ | Sampling period |
| $\mathbf{u}(t-\Delta)$ | input vector of ALE at time $t$ |
| $unwrap(.)$ | Phase unwrapping |
| $\mathbf{v}_k$ | Measurement noise of KF, PF and RBPF |
| $\mathbf{v}_t$ | Measurement noise of RBPF |
| Var | Variance |
| $\mathbf{w}(t)$ | Coefficient vector of ALE at time $t$ |
| $w_k^{(n)_i}$ | Weight of $n^{th}$ particle of $i^{th}$ RBPF at trial $k$ |
| $w_t^{(n)}$ | Weight of $n^{th}$ particle of RBPF at at time (trial) $t$ |
| $w_k^{(i)}$ | Weight of $i^{th}$ particle at trial $k$ |
| $\mathbf{w}_{k-1}^{\rho i}$ | State noise of non-linear state variable of $i^{th}$ RBPF |
| $\mathbf{w}_{k-1}^{a}$ | State noise of linear state variable of $i^{th}$ RBPF |
| $\mathbf{w}_{k-1}^{2}$ | State noise for linear state variable of RBPF |
| $\mathbf{w}_{t-1}$ | State noise of RBPF |
| $x(t)$ | Signal (time series) value at time $t$ |
| $\mathbf{x}_k^1$ | Non-linear state of RBPF at trial $k$ |
| $\mathbf{x}_k^2$ | Linear state of RBPF at trial $k$ |
| $\mathbf{x}_k$ | State of KF, PF and RBPF at trial $k$ |

| | |
|---|---|
| $\mathbf{x}_k^i$ | $i^{th}$ particle at trial $k$ |
| $\mathbf{X}$ | Mixture matrix |
| $\mathbf{z}_k$ | Measurment at trial $k$ |
| $(.)^T$ | Transpose operation |
| $\delta(.)$ | Dirac delta function |
| $\mu$ | Step size in ALE |
| $\Vert.\Vert_2$ | Frobenious norm |
| $\theta_i(t)$ | Instantaneous phase of $i^{th}$ IMF at time $t$ |
| $\theta_t(i)$ | Instantaneous phase of $i^{th}$ IMF at time $t$ |
| $\chi_{i,j}(k)$ | Cross spectrum of the $i^{th}$ and $j^{th}$ IMFs at $k^{th}$ frequency bin |
| $\psi_i(k)$ | Marginal power spectra of $i^{th}$ IMF at $k^{th}$ frequency bin |
| $\zeta_{ij}(k)$ | Coherence of $i^{th}$ and $j^{th}$ IMFs at $k^{th}$ frequency bin |
| $\gamma_{ij}$ | Phase synchronization of $i^{th}$ and $j^{th}$ IMFs |
| $\frac{\partial(.)}{\partial \mathbf{w}^T}$ | Gradient with respect to $\mathbf{w}^T$ |
| $\theta_t^{(n)}$ | Instantaneous phase of $n^{th}$ particle at time (trial) $t$ |
| $\rho_t^1(i)$ | Non-linear state of RBPF for $i^{th}$ IMF at time (trial) $t$ |
| $\rho_t^2(i)$ | Linear state of RBPF for $i^{th}$ IMF at time (trial) $t$ |
| $\boldsymbol{\mu}_k$ | Mean of linear state vector variable of RBPF at trial $k$ |
| $\boldsymbol{\rho}_t$ | State of RBPF at time (trial) $t$ |
| $\boldsymbol{\rho}_t^1$ | Non-linear state of RBPF at time (trial) $t$ |
| $\boldsymbol{\rho}_t^2$ | Linear state of RBPF at time (trial) $t$ |
| $\boldsymbol{\rho}_t(i)$ | State of RBPF for $i^{th}$ IMF at time (trial) $t$ |
| $\boldsymbol{\rho}_k^i$ | Non-linear state of $i^{th}$ RBPF at trial $k$ |
| $\boldsymbol{\rho}_k^{(n)_i}$ | $n^{th}$ particle of $i^{th}$ RBPF at trial $k$ |
| $\theta$ | Scale parameter for Gamma waveform |
| $\theta_{estimate}(t)$ | Estimated phase at time $t$ |
| $\theta_{actual}(t)$ | Actual phase at time $t$ |
| $\Delta$ | Prediction depth of ALE |
| $\pi$ | Ratio of any circle's circumference to its diameter (3.14159) |
| $\omega_i(t)$ | Instantaneous frequency of $i^{th}$ IMF at time $t$ |

# Chapter 1

# Introduction

Mental Fatigue refers to a state of the brain that is accompanied by reduced mental performance. It has been a major cause for many accidents especially in transportation (among drivers) and the aviation area such as military aviation. Therefore, detection of fatigue state of a human operator is necessary for prevention of disastrous accidents. Invention of electroencephalography (EEG) for recording brain electrical activity has made it possible to have a deep and comprehensive understanding of brain functionality. EEG is used as a technique for analysing physiological based changes of the brain in the fatigue state [1]. However, evaluating EEG signal for mental fatigue analysis has been limited to the classical signal processing methods. The development of signal processing methods for a better detection of fatigue state from EEG signals is therefore necessary. One research direction in this thesis is to extend and further develop the existing signal processing methods for mental fatigue analysis using the EEG signal.

There is a subgroup of electric signals from the brain using the EEG systems called event related potentials (ERPs). ERPs are responses of the brain to specifically designed stimuli. Extracting and evaluating the ERPs lead to understanding of various brain functions. For mental fatigue analysis, different ERP components and subcomponents are evaluated before and during the fatigue state. It is reported that attention related ERPs can be helpful for identification of the fatigue state [1]. Traditionally, ERPs are averaged over a number of trials because of their low signal to noise ratio (SNR). However averaging ERPs over a number of trials leads to the loss of information related to inter-trial variability of ERPs. Inter-trial variability of ERPs can provide useful information for detecting the fatigue state. Also, in the case of having correlated ERP subcomponents in temporal or spatial domain the classical methods such as principal component analysis (PCA), which is used for separation of correlated ERP subcomponents, fail. Therefore, another direction in this thesis is provision of new methods for effective extraction of ERPs which exploit the inter-trial variability of ERPs and overcome the problem of temporal/spatial correlation between the ERP subcomponents. Then, the estimated ERPs can be used for detection of fatigue state.

## 1.1 Aim and Objectives

In this thesis we aim to develop signal processing methods which are helpful for better estimation of ERPs and EEG phase synchronization. The new insights provided by the proposed methods for estimation of ERPs and EEG phase synchronization are new effective basis for mental fatigue analysis and detecting the fatigue state. Therefore, the main objective of this thesis has been on proposing new methods to be used for reliable detection of the fatigue state. This thesis represents significant contribution in the following areas:

- Estimation of EEG phase synchronization using combination of empirical mode decomposition (EMD) and adaptive line enhancer (ALE) with application to mental fatigue for extracting the relevant features.
- Proposing a new method for phase tracking of the oscillatory signals based on particle filtering (PF).
- Separation and tracking of P300 subcomponents overlapped in temporal domain using a new formulation of PF.
- Proposing a new spatio-temporal filtering method for estimation of correlated ERP subcomponents.

## 1.2 Thesis Outline

The layout of the thesis is as follows. In Chapter 2, the EEG recording procedure is briefly described. Then, the EEG advantages and disadvantages in comparison with other data acquisition modalities for recording brain activities are provided. Some EEG specifications such as EEG rhythmic activities are also provided in Chapter 2. Finally ERPs, particularly P300, are explained.

In Chapter 3, first, fatigue and its research motivation are described. Then, two directions based on EEG and ERP for mental fatigue analysis including the existing and newly proposed approaches are explained. This chapter ends with description of the fundamentals of PF and Kalman filtering (KF) which are then used in the next two chapters for two different purposes.

In Chapter 4, a new approach for EEG phase synchronization is proposed. This approach combines EMD and ALE for extracting and denoising EEG rhythmic activity and then computes the linear and non-linear synchronization measures. As an application the approach is applied to mental fatigue data in order to find and extract the effective features which can be employed for full mental fatigue analysis in future studies. In addition, a new phase tracking method is proposed at the end of this chapter. The new method can be used for tracking the instantaneous phase of an EEG oscillation. The method should be refined more and exploited for measuring synchronization of different EEG oscillations for mental fatigue analysis in future studies.

In Chapter 5 a new temporal method for separation and tracking the variability of P300 subcomponents across different trials based on coupled particle filtering is proposed. The method imposes physiological based constraints on the PF for a more reliable estimation. Using the simulated signals, the performance of the method is tested in different situations. The method is then applied to a sample mental fatigue data to show its potential use for mental fatigue analysis where the effects of each P300 subcomponent can be analysed separately in the fatigue state.

In Chapter 6, a new spatio-temporal filtering method for ERP subcomponent estimation is proposed. The proposed method is based on deflating one of the correlated subcomponents in spatial domain while extracting another subcomponent in the temporal domain. Considering the mathematical framework of the method and also based on the simulation results, it is shown that the method is robust against both temporal and spatial correlations between the ERP subcomponents. The performance of the method is compared with those of different methods such as spatial PCA and temporal PCA in different situations using simulated data and its superiority is demonstrated. Finally, the method is applied to a real data sample to show its potential use in ERP subcomponent estimation. The method can be used in different applications such as differentiating schizophrenic patients and healthy subjects or determination of fatigue state in mental fatigue analysis.

In Chapter 7 an auditory based paradigm is used and implemented when the EEG is recorded before and during fatigue state. Then, the proposed methods in Chapters 4 and 6 are used for estimation of single trial P300 subcomponents and EEG phase synchronization before and during fatigue state. The results demonstrate the potential use of the extracted features obtained in the auditory based paradigm for detection of mental fatigue state.

# Chapter 2

# Overview of EEG and ERP

In this chapter, first, EEG along with its recording procedure and specifications are explained. Then, ERPs particularly one of the main ERP components, namely P300, are briefly described.

## 2.1 Electroencephalography

EEG is the recorded electrical activity of the brain over the scalp which is produced by the firing of neurons in the brain. EEG has been found to be useful in the diagnosis of epilepsy, coma, encephalopathies, brain death and monitoring the depth of anaesthesia [2]. In addition to the conventional and clinical use of EEG, it is used for many other purposes such as brain-computer interface (BCI) which aims at improving the life style of disabled people.

### 2.1.1 EEG Recording

In conventional recording of EEG from scalp, the electrodes are placed on the scalp with a conductive gel or paste. In most systems each electrode is attached to an individual wire. Usually in most clinical and research applications, the international 10-20 system is used for specifying electrode locations and names. The electrode locations of a 75-electrode EEG recording system using the extended 10-20 electrode positioning and their labels are illustrated in Fig. 2.1.

The recorded EEG signal is filtered in the preprocessing stage to remove the noise and other artefacts. Normally, the EEG is highpass filtered with a cutoff frequency between 0.5-1 Hz and is lowpass filtered with a cutoff frequency between 35-70 Hz. The highpass filter is useful for filtering out the slow artefacts like electrogalvanic signals and movement artefact [2] while lowpass filter is useful for filtering out the high-frequency artefact like electromyographic interferences [2, 3].

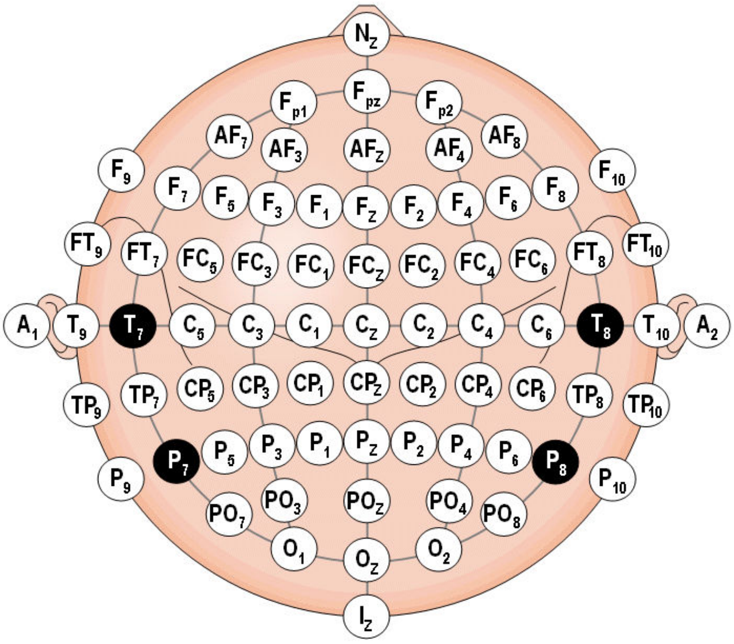

Figure 2.1: 75-pin electrode positions based on extended 10-20 system [http://www-psych.nmsu.edu/ jkroger/lab/principles.html].

Sometimes it is necessary to place the electrodes near the surface of the brain as it is typically needed for epilepsy surgery. These electrodes are referred to as electrocorticography (ECoG), intracranial EEG (I-EEG) or subdural EEG (SD-EEG) electrodes [2]. The ECoG signal is processed in the same way as the scalp EEG. Since the subdural signal is composed of predominance of higher frequency components, the ECoG is usually recorded at higher sampling rates than scalp EEG to meet the Nyquist criterion. However since many of the artefacts which affect scalp EEG do not have impact on ECoG, its filtering in the preprocessing stage is not required. Most of the times an additional notch filtering is applied in order to remove the artefacts which are generated by electrical power lines (60 Hz in the United States and 50 Hz in many other countries including United Kingdom).

One of the most common types of artefact is eye blink. EEG signal is usually contaminated with eye blink artefact. For removal of the eye blink artefact, conventionally independent component analysis (ICA) [4] is applied to the EEG signal. Then, one of the resulted components which corresponds to the eye blink is set to zero and all the components are projected back to the electrode space. In this way a new set of EEG signals are generated which is free of eye blink artefact.

Electric potentials are measured with respect to a reference which is an arbitrary chosen zero level. There are different choices for the reference which depend on the recording purpose. In referential montage, the recorded potential at each channel is the difference between the potential at that channel and a specified reference electrode. There is not a unique and standard location for the reference, however the reference should be in a different position than the recording electrodes. Typically, the midline positions are used for reference since they do not amplify the signal in one hemisphere of the head versus the other hemisphere. There is another common reference called *linked ears*. This reference is a physical or mathematical average of the channels attached to both earlobes or mastoids [2].

### 2.1.2 EEG versus fMRI, PET and MEG

EEG as a non-invasive, convenient and inexpensive tool which is used for analysing brain activity. The main advantage of EEG is its high temporal resolution. However one limitation of EEG is its poor spatial resolution. Other methods such as positron emission tomography (PET) [5] and functional magnetic resonance imaging (fMRI) [6] have better spatial resolution while their temporal resolution is low. The difference between EEG and these methods (PET and fMRI) is that EEG directly measures the brain activity while fMRI records the changes in blood flow and PET measures the changes in metabolic activity, both of which are indirect markers of the brain activity. EEG can be recorded simultaneously with the fMRI. In this case a high temporal resolution data is recorded at the same time with a high spatial resolution data. However there are some difficulties in such a multi-modal recording. One difficulty is that the data derived from each of the tools occur at different times, therefore they do not necessarily relate to the same brain activity.

Magnetoencephalography (MEG) is an imaging technique which is used to measure the magnetic fields produced by the electrical activity in the brain. The MEG is recorded using an extremely sensitive device such as super conducting interference devices (SQUIDs) [7]. Magnetic fields are less distorted by the resistivity of the skull and scalp in comparison with electrical fields used in EEG. Therefore, MEG is less distorted by non-linearity of the head tissues but is more noisy than EEG due to complexity of the measurements. The temporal resolution of EEG is higher than MEG. EEG can also be recorded at the same time as MEG so the recorded data benefit from the high temporal resolution of EEG.

### 2.1.3 EEG Rhythmic Activities

EEG is usually described with respect to its rhythmic activities. The rhythmic activity is typically characterized by the frequency bands. It is noted that the EEG rhythmic activity in a certain frequency interval (band) has a certain scalp distribution and/or a certain biological importance. Traditionally spectral methods are used in order to extract EEG rhythmic activity in a certain frequency band. In the following the six most important EEG rhythmic activities in different frequency bands are briefly described.

- Delta is a rhythmic activity in the range of 0.5-4 Hz which was found and introduced by Walter [8] as a rhythmic activity below 8 Hz. However later Walter and Dovey [9] established the rhythmic activity below 4 Hz as the delta rhythmic activity. Delta rhythm contains the high amplitude waves. It is usually seen in babies, adults in sleep and during some sustained attention [10]. The location of the delta wave is in the frontal part of the adult brain and posterior parts of the children brain. Delta rhythmic activity is prominent over the anterior regions of the brain in the deep stage of sleep [2].

- Theta is a rhythmic activity in the range of 4-8 Hz that was introduced by Walter and Dovey [9]. It is usually seen in children and in the state of drowsiness or arousal of the older children and adults. It also has been found to be associated with the inhibition of the elicited responses [10]. It has been shown in [9] that theta activity is associated with emotional processes and it appears at the interruption of a pleasurable stimulus. Theta activity in the range of 6-7 Hz over the frontal regions of the brain has been found to be correlated with mental activities [11, 12, 13].

- Alpha is a rhythmic activity in the range of 8-13 Hz. It has been found in the state of relaxing, closing eyes, and relative mental inactivity [14]. Posterior parts of the head are the main generators of the alpha rhythm. The alpha rhythm is expected to be blocked or attenuated by attention, visual, and mental effort [14]. However, there are some reports that in most cases the alpha rhythm is not attenuated or blocked by mental efforts such as solving arithmetics [15]. Other factors such as difficulty of the task, motivation of the subject to please the examiners play an important role on blocking of alpha rhythm [2].

- Mu is a rhythmic activity in the range of 8-13 Hz. It is almost in the same frequency as alpha rhythm and is sometimes confused with that. However it is different from alpha rhythm in terms of topography and physiological significance [2]. Mu rhythm is seen over the sensorimotor cortex. It is significantly suppressed during contralateral motor acts [16, 17]. It is shown that Mu rhythm is suppressed in somatic areas of the cortex when an epileptic patient is observing the moving body parts [18].

- Beta is a rhythmic activity in the range of 13-30 Hz. It contains low amplitude waves which are mostly evident in frontal and central parts of the brain. The distribution of the beta rhythm is symmetrical and in both sides of the head. The beta rhythm is most evident when the brain is active, busy or in the state of concentration. Like Mu rhythm, beta rhythm can be attenuated with the movement, especially contralateral movement, and even with the thinking about carrying out the movement [2].
- Gamma is a rhythmic activity in the range of 30-100 Hz. The amplitude of gamma rhythm is usually very low and its appearance is rare. The gamma rhythmic activities around 40 Hz over brain central regions have been observed around movement onset [19] which is associated with event related synchronization (ERS). The ERS of gamma wave is used in [20] to demonstrate the locus for right and left index finger movement, right toes, and bilateral area for finger movement.

Effective and adaptive extraction of EEG rhythmic activities for estimation of their synchronization across different brain regions and frequency bands is exploited in Chapter 4.

## 2.2 Event Related Potentials

ERP is often considered as any stereotyped electrophysiological response to an external or internal stimulus [21]. Although ERPs can be measured with EEG, since EEG reflects thousands of simultaneously ongoing brain responses ERPs are not usually visible in the EEG recording from a single trial. One conventional method to extract ERPs is to average EEG over a large number of trials which are the brain responses to the stimulus so that the non-ERP related activities are filtered out and ERPs will become visible.

ERPs are useful for analysis of brain functional and mental abnormalities [2]. Single trial ERPs are of particular interest since the dynamics of brain responses can be followed. Therefore, there has been a great interest in estimation of ERPs. Estimation of single trial ERPs are considered in this thesis in Chapters 5 and 6.

### 2.2.1 P300

P300 is one of the main component of ERPs. It is a positive wave around 300 ms after the stimulus onset. It usually occurs after an auditory, visual, or somatosensory stimulus. The acquisition of P300 is easy. P300 often has a large amplitude (5-20$\mu$V). Amplitude of P300 is denoted as the largest peak of ERP waveform within a time window around 300 ms. Latency of P300 is denoted at the time from the stimulus onset to the timing of the largest positive peak of P300 (e.g. P300 amplitude) [22]. P300 amplitude is usually larger in parietal electrode sites [23].

P300 is typically elicited using an oddball paradigm. There are different variations of the oddball task. In an oddball task which contains only one stimulus type, the infrequent stimulus is presented as the target. In a typical two-stimulus oddball a number of infrequent targets are presented in a background of frequent stimuli. In a typical three-stimulus oddball, a number of infrequent target are presented in a background of frequent stimuli and also a number of infrequent distractor stimuli.

In all types of oddball paradigms, the task of the subject is to respond to the target stimulus often by pressing a button or by counting the number of target stimuli. In single and two-stimulus oddball, the response of the subject to the infrequent target stimulus does elicit a P300 [22]. However in the three-stimulus oddball, the response of the subject to the infrequent target does elicit P3b and the infrequent distractor causes elicitation of P3a [22].

P3a and P3b are subcomponents of P300. The scalp distribution of P3a usually has maximum amplitude in frontal/central regions while for P3b the scalp distribution is maximum in parietal regions of the brain. P3a and P3b can also be obtained by decomposing the P300 obtained in a single or two-stimulus oddball paradigm to its constituent subcomponents. One popular method which initially applied for decomposing P300 in a two-stimulus oddball paradigm is principal component analysis (PCA) method [22]. Considering the inter-trial variability of P300 and its subcomponents, the existence of correlated noise, the temporal/spatial correlation between the P300 subcomponents, PCA method is not a reliable method for estimation of P3a and P3b. Therefore, there is a need for a reliable and robust method for single trial estimation of P300 subcomponents that is one of the main objectives in this thesis and is exploited in Chapters 5 and 6.

## 2.3 Summary

In this chapter a brief introduction about EEG and ERPs, which will be useful in development of the rest of the thesis, is provided. The EEG recording procedure is briefly described. Then, EEG is compared with other techniques such as fMRI, PET, MEG. In addition, an important characteristic of EEG which is its rhythmic activity is explored. Finally, ERPs including P300 subcomponents are briefly described.

# Chapter 3

# Recognition of Mental Fatigue: Tools and Algorithms

In this chapter first fatigue and the motivation for its recognition and monitoring are described. Then, two main approaches for mental fatigue analysis that are used in literature are explained. These approaches include ERP and EEG based analysis of mental fatigue. New directions in both ERP and EEG based methods for analysis of mental fatigue, which are the main objectives of this thesis, are suggested. Since PF and KF approaches are used in two chapters for two different purposes, their fundamentals are provided in the last section of this chapter.

## 3.1 Fatigue and its Research Motivation

FATIGUE is a common phenomenon that exists in our everyday life. It is defined in medicine as “that state, following a period of mental or bodily activity, characterized by a lessened capacity for work and reduced efficiency of accomplishment, usually accompanied by a feeling of weariness, sleepiness, or irritability” [24]. Therefore, fatigue can have physical or mental components. The concept of mental fatigue is introduced in [25] where it is clearly distinguished from physical fatigue. Based on [25], physical fatigue is assumed to be related to reduced muscular system performance while mental fatigue is related to reduced mental performance and alertness. Based on some research on driver fatigue, it has been found that there is a cortical deactivation in the mental fatigue state [26, 27, 28].

There are many occupations in aviation, military, aerospace, transportation, medicine, and industrial settings in which the operators continuously perform complex or exhaustive tasks. The state of reduced performance of the operators as a result of fatigue has caused many disasters, mostly not well known to the public. These disasters include the nuclear plant accidents at Three-Mile Island and Chernobyl and grounding of the oil tanker Exxon Valdez that was a transport disaster [29, 30]. There are also other evidences that the fatigued individuals have contributed to the major incidents and accidents in industrial operations. Recent investigation of crash data has provided a new insight which shows the risk involved for the driver under fatigue is more than when using alcohol or cellphone [31]. Therefore, scientific interests in monitoring, assessing and predicting the fatigued operator have been increasing recently.

As it is mentioned above, fatigue can be classified as physical and mental fatigues. The focus in this thesis is on mental fatigue. Mental fatigue can be analysed using EEG signals. Assessment of mental fatigue based on the recorded EEG can be performed from two main directions. One is EEG-based analysis of mental fatigue. Physiological based changes of EEG signal in the fatigue state have been reported in mental fatigue analysis. This direction is explained in Section 3.2. Another direction is to evaluate the changes in ERP waves (which should be first separated from background EEG) usually in a time-locked experiment about one second after stimulus onset in the fatigue state. This direction is explained in Section 3.3.

## 3.2 EEG-based Analysis of Mental Fatigue

Using EEG, it is possible to examine the physiological changes related to mental fatigue [1]. EEG is the electrical activity of the brain that enables the study of brain functions with a high time resolution, although the spatial resolution is relatively modest [32].

In traditional EEG-based analysis of mental fatigue, power spectrum of EEG in different frequency bands is considered as the key EEG feature [1]. Then, the observed changes of power spectrum of EEG in certain frequency bands and in certain brain regions are reported for quantification of mental fatigue.

One of the most common findings in EEG studies of mental fatigue is that when the level of alertness drops, the EEG signal contains more slow and high amplitude waves than fast and low amplitude waves. More specifically, when the level of arousal decreases, the low-frequency theta and alpha activities continuously increase which can be due to the decrease in cortical activation [33, 34].

When subjects become fatigued, it is expected that the level of arousal drops and this can be related to the increase in alpha and theta power spectrum [35, 36, 37, 38, 39]. Therefore, based on most previous studies, the amount of alpha and theta power spectrum can provide an index of the level of mental fatigue that subjects experience.

However, the reports of previous research on EEG changes regarding the mental fatigue are varying and even are conflicting [40]. This can be due to methodological limitation since most of them use classic statistical analysis, or can be due to different experimental setup. Therefore, there is a challenge to design an appropriate task and extract the key EEG features for EEG-based monitoring and identification of mental fatigue.

Mental fatigue is assumed to be associated with cortical deactivation of the functional lobes of the brain. This usually results in mis-communication between brain regions [41]. Therefore, the experimental setup for monitoring mental fatigue should satisfy several criteria in order to be able to examine brain changes and mechanism of the modulating deactivation, activation, and information processing between the functional lobes of the brain. The following criteria are found to be effective [40]:

(i) The task should contain as many functional lobes as possible,
(ii) The task performance should be dependent on the correct information processing such as decision making of the pre-frontal brain lobe and correct communication among different functional brain lobes (e.g. working memory).
(iii) The task should require the subjects to attain constant attention and alertness but contain little skill and learning effect.

In a three-hour experiment in [1] the increases in alpha, theta, and beta powers were observed. In addition, the subjective measures acquired from the subjects indicated that they became more fatigued during the task performance. In [38] it has been discussed that the increase in lower-alpha power can be related to increased efforts by the subjects to remain alert. In [1] it is reported that observed increase in lower-alpha power has shown to be significantly correlated with the increase in the level of fatigue reported by the subjects.

Since the development of machine learning algorithms, it has also been possible to benefit from the recently developed algorithms for monitoring mental fatigue. Random Forests (RF) has shown superior performance for classification and feature selection in many practical applications [42, 43]. In [44], the EEG-based monitoring of fatigue in multi levels has been performed by exploiting RF. Therefore, RF is used in [44] for extracting key EEG features and multi-level monitoring of mental fatigue. The initial features are extracted by considering the calculated power spectral density in the four standard frequency bands (delta, theta, alpha, beta) from 19 channels using fast Fourier transform with Hanning window [45]. After feature reduction and classification, 17 key features are found which most of them correspond to the electrodes in the frontal and occipital regions of the brain. These key EEG features are related to all four standard frequency bands. Therefore, all frequency bands play a role in monitoring multi-level mental fatigue.

In a recent study on EEG-based analysis of mental fatigue, approximate entropy (ApEn) and Kolmogorov complexity (Kc) [46, 47, 48] are used in order to quantify the complexity of EEG signal under two mental fatigue states [49]. Then, kernel principal component analysis (KPCA) [50, 51] and Hidden Markov Model (HMM) [52] are combined to classify the two mental fatigue states.

A functional relationship between different brain regions is generally associated with synchronous electrical activities in these regions [53]. Recorded EEGs can be used for measuring synchronization of different brain regions. Analysis of mental fatigue from EEG perspective in this thesis is devoted to measurement of the linear and non-linear synchronization of different brain regions by exploiting adaptive methods such as EMD [54] and ALE [55] algorithms. The synchronization measures can reveal useful information about the changes in the functional connectivity of brain regions during the fatigue state which are evaluated in Chapter 4.

## 3.3 ERP-based Analysis of Mental Fatigue

One conventional approach to extraction and analysis of the ERP components is by averaging the time-locked single trial ERPs. This approach assumes that the ERP wave remains constant across trials and averaging over time-locked single trials attenuates the background EEG which is considered as a random process. In many real applications, this assumption is not realistic. For example, changes in the degree of mental fatigue, habituation, or the level of attention, can affect the ERP waveform; therefore, the inter-trial variability of ERP components would be ignored by averaging the ERPs over a number of trials. Trial to trial variability of ERP components is also an important key in order to investigate some brain abnormalities such as schizophrenia and depression [56, 57].

An effective analysis of ERPs should thus be based on single trial estimation. Several methods based on statistical signal processing including Wiener [58], maximum a posteriori (MAP) [59] and KF approaches [60, 61] have been used in single trial estimations. Other popular methods are proposed in [4, 62] and [63] which are based on PCA and ICA. These methods are not suitable in low SNRs or when there are possible dependency or correlation between the components.

Sparse component analysis also has been used for estimation of ERP components [64]. The main focus of most of the above methods has been on single trial estimations of ERP components. These methods often fail in many situations because of very low signal to background noise power ratios and inter-trial variability of the recorded ERPs.

Inter-trial variability of ERPs has been considered in some other studies [65, 66, 67]. In [67] single trial parameters of the ERP and the autoregressive representation of the ongoing activity are obtained simultaneously. A recent work in [68] formulates wavelet coefficients of the time-locked measured ERPs in the state space and then estimates the ERP components by applying PF. It is shown that the formulated PF outperforms KF. Although in these methods inter-trial variability of ERP components are taken into account, they are appropriate only for single trial estimation. These methods however fail in estimation of the ERP subcomponents particularly when they overlap in temporal domain. In the following it is explained that ERP subcomponents such as P300 subcomponents are very useful and important for mental fatigue analysis. Therefore, some new methods for ERP subcomponent estimation are demanded which consider the correlations between the ERP subcomponents and enable their separation over the temporal/spatial domain.

As explained in the previous chapter, one of the main ERP components is P300 that contains two subcomponents; P3a and P3b. These subcomponents usually have temporal correlation and overlap over the scalp [22]. The P300 component has been found to be useful in identifying the depth of cognitive information processing [69]. It has been reported that the P300 amplitude elicited by mental task loading decreases with an increase in the perceptual/cognitive difficulty of the task and its latency increases when the stimulus is cognitively difficult to process [22, 70, 71, 72, 73, 74]. Therefore, extracting and analysing P300 before and during fatigue state have been of great interest among mental fatigue researchers. However, in more recent researches in mental fatigue analysis in [69] and [70], it has been suggested to detect and evaluate the P300 subcomponents before and during fatigue state because it has been shown that the averaged P300 does not always correspond to manifestation or appearance of mental fatigue. Therefore, analysis of mental fatigue based on ERP must be performed from multiple aspects using not only P300 amplitude and latency but also feature parameters related to its subcomponents such as P3a and P3b.

Some research has been carried out using blind source separation (BSS) and PCA for the estimation of P300 subcomponents [69, 75, 76, 77, 78] for decomposition of the P300 into its subcomponents. In some studies PCA has been applied to the averaged ERP [79, 80, 81]. These methods are suitable for stationary data and therefore, not recommended for separation of ERP subcomponents, which are generally non-stationary. The major problem with these methods is that when there is a high temporal correlation between the subcomponents, low signal to noise ratio ERPs or in the case of existence of correlated noise, they fail to produce correct results. In some cases they are able to estimate only one of the subcomponents. Therefore, a more reliable method for single trial estimation of the P300 subcomponents which can be effectively used in mental fatigue analysis is highly demanded.

One of the main directions in this thesis is to estimate P300 subcomponents in single trial recordings. In Chapter 5, PF is used to track P300 subcomponents in different trials. The proposed method is applied to a subject which goes under fatigue in a visual based experiment. The method considers the temporal variations of the P300 subcomponents in different trials. Therefore, some auxiliary methods should be employed in order to estimate spatial distribution of the P300 subcomponents. In [82], a spatial notch filter is used to localize the ERP subcomponents in the brain. In this approach although the correlation between the desired ERP component and the background EEG has been exploited, the correlation between the ERP subcomponents is ignored. This motivated us to introduce a new spatio-temporal filtering method in Chapter 6 for robust single trial estimation of the spatially or temporally correlated ERP subcomponents. The method can be effectively used for P300 based analysis of mental fatigue in future studies.

In this thesis PF is used for separation and tracking of P300 subcomponents in single trials and also for phase tracking of oscillations in EEG signals. Therefore, in the next section, fundamentals of PF, KF, and Rao-Blackwellised particle filtering (RBPF) are explained.

## 3.4 Fundamentals of KF, Basic PF, and RBPF

In this study Basic PF (called PF from now on) and RBPF approaches are used for proposing new methods for ERP subcomponent tracking and EEG phase tracking. Since RBPF uses KF in order to estimate the linear state variables, in this section PF, KF, and RBPF are explained. PF usually is suitable for non-linear state space while KF is appropriate for a linear state space. RBPF, on the other hand, is useful for the case that it is possible to partition the state variables into linear and non-linear parts. The RBPF then estimates the linear part by KF and the non-linear part by PF. In the following first in Section 3.4.2 KF is described. Then, PF and RBPF are explained in Sections 3.4.3 and 3.4.4 respectively.

### 3.4.1 Problem Formulation in State Space

In order to define and formulate the problem of tracking [83], the state sequence $\{\mathbf{x}_k, k \in N\}$ of a target can be considered as:

$$\mathbf{x}_k = f_k(\mathbf{x}_{k-1}, \mathbf{n}_{k-1}) \tag{3.1}$$

where $f_k$ is generally a non-linear function of the state $\mathbf{x}_{k-1}$ and $\{\mathbf{n}_{k-1}, k \in N\}$ is an i.i.d. noise sequence. The objective of tracking is to use all available observations $\mathbf{z}_k$ and recursively estimate $\mathbf{x}_k$:

$$\mathbf{z}_k = h_k(\mathbf{x}_k, \mathbf{v}_k) \tag{3.2}$$

where $h_k$ is the non-linear function and $\{\mathbf{v}_k, k \in N\}$ is an i.i.d. measurement noise sequence. In particular, we search for the filtered estimates of $\mathbf{x}_k$ based on all available measurements $\mathbf{z}_{1:k} = \{\mathbf{z}_i, i = 1, ..., k\}$ up to time $k$. Using the Bayes theorem and assuming that the state $\mathbf{x}_k$ and observation $\mathbf{z}_k$ are Markov processes, the observation at time iteration $k$ which is $\mathbf{z}_k$ is used in order to recursively update the posterior density of the state:

$$p(\mathbf{x}_k|\mathbf{z}_{1:k}) = \frac{p(\mathbf{z}_k|\mathbf{x}_k)p(\mathbf{x}_k|\mathbf{z}_{1:k-1})}{p(\mathbf{z}_k|\mathbf{z}_{1:k-1})} \tag{3.3}$$

Assuming that $p(\mathbf{x}_{k-1}|\mathbf{z}_{1:k-1})$ at iteration $k-1$ is available, $p(\mathbf{x}_k|\mathbf{z}_{1:k})$ can be computed using the Chapman-Kolmogorov as:

$$p(\mathbf{x}_k|\mathbf{z}_{1:k-1}) = \int_{all\ \mathbf{x}_{k-1}} p(\mathbf{x}_k|\mathbf{x}_{k-1})p(\mathbf{x}_{k-1}|\mathbf{z}_{1:k-1})d\mathbf{x}_{k-1} \tag{3.4}$$

In equation (3.3), $p(\mathbf{z}_k|\mathbf{z}_{1:k-1})$ is a normalizing constant and it only depends on the observation model in equation (3.2) and the statistics of the noise $\mathbf{n}_k$:

$$p(\mathbf{z}_k|\mathbf{z}_{1:k-1}) = \int_{all\ \mathbf{x}_k} p(\mathbf{z}_k|\mathbf{x}_k)p(\mathbf{x}_k|\mathbf{z}_{1:k-1})d\mathbf{x}_k \tag{3.5}$$

Tracking and estimation of the state of the system is possible by solving the above equations and recursions. However in real world applications, usually it is difficult to compute the normalizing constant $p(\mathbf{z}_k|\mathbf{z}_{1:k-1})$, the marginal posterior density $p(\mathbf{x}_k|\mathbf{z}_{1:k-1})$ and consequently the posterior density $p(\mathbf{x}_k|\mathbf{z}_{1:k})$. The computations should be conducted in high-dimensional complex integrals. Therefore, much effort has been done in order to solve the recursions in the above equations. KF and PF are among popular approaches. As it is stated in the beginning of the section, the KF is useful for analysis of linear systems and PF for analysis non-linear systems. In the following subsections both of them are described. Finally, the RBPF is explained briefly.

### 3.4.2 Kalman Filtering

In KF the state space is assumed to be linear and by making a number of assumptions which are explained below, the posterior density becomes Gaussian [83]. Therefore, only the mean and covariance matrices are calculated in each step. First, it is assumed that the state transition and observation functions are known and linear functions. Therefore, equations (3.1) and (3.2) can be rewritten as:

$$\mathbf{x}_k = \mathbf{F}_k \mathbf{x}_{k-1} + \mathbf{n}_{k-1} \tag{3.6}$$

$$\mathbf{z}_k = \mathbf{H}_k \mathbf{x}_k + \mathbf{v}_k \tag{3.7}$$

$\mathbf{n}_{k-1}$ and $\mathbf{v}_k$ are assumed to be mutually independent and are drawn from Gaussian distributions. They are considered to be white Gaussian noise (WGN) with known covariances $\mathbf{Q}^n_{k-1}$ and $\mathbf{Q}^v_k$ respectively. The initial distribution (prior distribution) $p(\mathbf{x}_0) = \mathcal{N}(\mathbf{x}; \mathbf{m}_0, \mathbf{P}_0)$ is assumed to be Gaussian with known mean $\mathbf{m}_0$ and covariance matrix $\mathbf{P}_0$, $\mathcal{N}(\mathbf{x}; \mathbf{m}, \mathbf{P})$ refers to a Gaussian distribution of $\mathbf{x}$ with mean $\mathbf{m}$ and covariance $\mathbf{P}$. Based on the above assumptions, the KF is reduced to the following recursive equations:

$$\begin{aligned} p(\mathbf{x}_{k-1}|\mathbf{z}_{k-1}) &= \mathcal{N}(\mathbf{x}_{k-1}; \mathbf{m}_{k-1,k-1}, \mathbf{P}_{k-1,k-1}) \\ p(\mathbf{x}_k|\mathbf{z}_{k-1}) &= \mathcal{N}(\mathbf{x}_k; \mathbf{m}_{k,k-1}, \mathbf{P}_{k,k-1}) \\ p(\mathbf{x}_k|\mathbf{z}_k) &= \mathcal{N}(\mathbf{x}_k; \mathbf{m}_{k,k}, \mathbf{P}_{k,k}) \end{aligned} \tag{3.8}$$

where $\mathbf{m}_{i,j}$ and $\mathbf{P}_{i,j}$ are the mean and covariance of the conditional density $p(\mathbf{x}_i|\mathbf{x}_j)$. The used parameters (mean and covariance in the above equations) are calculated in two steps, namely KF prediction and update steps, as:

- Prediction step:

$$\begin{aligned} \mathbf{m}_{k,k-1} &= \mathbf{F}_k \mathbf{m}_{k-1,k-1} \\ \mathbf{P}_{k,k-1} &= \mathbf{Q}^n_{k-1} + \mathbf{F}_k \mathbf{P}_{k-1,k-1} \mathbf{F}^T_k \end{aligned} \tag{3.9}$$

- Update step:

$$\begin{aligned} \mathbf{m}_{k,k} &= \mathbf{m}_{k,k-1} + \mathbf{K}_k (\mathbf{z}_k - \mathbf{H}_k \mathbf{m}_{k,k-1}) \\ \mathbf{P}_{k,k} &= \mathbf{P}_{k,k-1} - \mathbf{K}_k \mathbf{H}_k \mathbf{P}_{k,k-1} \end{aligned} \tag{3.10}$$

where

$$\begin{aligned}\mathbf{S}_k &= \mathbf{H}_k \mathbf{P}_{k,k-1} \mathbf{H}_k^T + \mathbf{Q}_k^v \\ \mathbf{K}_k &= \mathbf{P}_{k,k-1} \mathbf{H}_k^T \mathbf{S}_k^{-1}\end{aligned} \tag{3.11}$$

are the covariance of the innovation term $\mathbf{z}_k - \mathbf{H}_k \mathbf{m}_{k,k-1}$ and the Kalman gain, respectively. Also, in the above equations $(.)^T$ denotes matrix transpose operation. If all the assumptions are hold for a system, the KF results in an optimal solution. Therefore, in the linear Gaussian system where the state distribution is Gaussian, KF is the best estimator.

### 3.4.3 Particle Filtering

PF is a powerful technique for sequential signal processing which has variety of applications in array and video processing and target tracking. The key idea behind PF is to represent the required posterior density function $p(\mathbf{x}_k|\mathbf{z}_{1:k})$ by a set of random samples with their associated weights and then compute the estimates based on these samples and weights. Therefore, the posterior distribution can be approximated by particles $\{\mathbf{x}^{(n)}, n = 1, \ldots, N_s\}$ and their associated weights $\{w^{(n)}, n = 1, \ldots, N_s\}$ as [83]:

$$p(\mathbf{x}_k|\mathbf{z}_{1:k}) \propto \sum_{i=1}^{N_s} w_k^{(i)} \delta(\mathbf{x}_k - \mathbf{x}_k^{(i)}) \tag{3.12}$$

Since it is not feasible to draw samples from the posterior density before it is estimated, the samples are drawn from a so called importance density. This is the principle of importance sampling [84] in which the samples are easily generated from the importance density. Then, the weights in equation (3.12) are defined by:

$$w_k^{(i)} = \frac{p(\mathbf{x}_k^i|\mathbf{z}_{1:k})}{q(\mathbf{x}_k^i|\mathbf{z}_{1:k})} \tag{3.13}$$

where $q(.)$ is the importance density. If the importance density is chosen such that it can be factorized to:

$$q(\mathbf{x}_k|\mathbf{z}_{1:k}) = q(\mathbf{x}_k|\mathbf{x}_{k-1}, \mathbf{z}_{1:k}) q(\mathbf{x}_{k-1}|\mathbf{z}_{1:k-1}) \tag{3.14}$$

then it is possible to obtain samples $\mathbf{x}_k^i \sim q(\mathbf{x}_k|\mathbf{z}_{1:k})$ by augmenting each of the existing samples $\mathbf{x}_{k-1}^i \sim q(\mathbf{x}_{k-1}|\mathbf{z}_{1:k-1})$ with the new state $q(\mathbf{x}_k|\mathbf{x}_{k-1}, \mathbf{z}_{1:k})$. Via the Bayes rule $p(\mathbf{x}_k|\mathbf{z}_{1:k})$ is first expressed in terms of $p(\mathbf{x}_{k-1}|\mathbf{z}_{1:k-1})$, $p(\mathbf{z}_k|\mathbf{x}_k)$, and $p(\mathbf{x}_k|\mathbf{x}_{k-1})$ in order to derive the weight update equation [83]:

$$p(\mathbf{x}_k|\mathbf{z}_{1:k}) \propto p(\mathbf{x}_{k-1}|\mathbf{z}_{1:k-1}) p(\mathbf{z}_k|\mathbf{x}_k) p(\mathbf{x}_k|\mathbf{x}_{k-1}) \tag{3.15}$$

By substituting equations (3.15) and (3.14) into equation (3.13), the weight update equation can be obtained as:

$$\begin{aligned} w_k^{(i)} &\propto \frac{p(\mathbf{x}_{k-1}^{(i)}|\mathbf{z}_{1:k-1})p(\mathbf{z}_k|\mathbf{x}_k^{(i)})p(\mathbf{x}_k^{(i)}|\mathbf{x}_{k-1}^{(i)})}{q(\mathbf{x}_k^{(i)}|\mathbf{x}_{k-1}^{(i)},\mathbf{z}_{1:k})q(\mathbf{x}_{k-1}^{(i)}|\mathbf{z}_{1:k-1})} \\ &= w_{k-1}^{(i)}\frac{p(\mathbf{z}_k|\mathbf{x}_k^{(i)})p(\mathbf{x}_k^{(i)}|\mathbf{x}_{k-1}^{(i)})}{q(\mathbf{x}_k^{(i)}|\mathbf{x}_{k-1}^{(i)},\mathbf{z}_{1:k})} \end{aligned} \tag{3.16}$$

The most popular choice for the importance density is the prior density. Selecting the prior density as the importance density is simple and intuitive, however, this selection leads to higher error in estimation in some applications especially when low number of particles are used. Therefore, in [83] it is suggested to draw the samples from the likelihood (rather than prior density) where applicable. In this research a reasonable number of particles are used and therefore, the prior density is used as the importance density:

$$q(\mathbf{x}_k^{(i)}|\mathbf{x}_{k-1}^{(i)},\mathbf{z}_{1:k}) = p(\mathbf{x}_k^{(i)}|\mathbf{x}_{k-1}^{(i)}) \tag{3.17}$$

Substitution of equation (3.17) into equation (3.16) yields:

$$w_k^{(i)} \propto w_{k-1}^{(i)}p(\mathbf{z}_k|\mathbf{x}_k^{(i)}) \tag{3.18}$$

Based on the above equation the weight of each particle is obtained from its weight in the previous trial multiplied by the likelihood of the observation given the current state by the corresponding particle. In the subsequent trials, the weight of a large number of particles can become small. The contribution of these particles to the estimation of posterior density is very trivial while large computations are performed in order to update the weights of these particles. The resampling technique [83] is proposed to avoid such situations by eliminating the particles with small weights and replicating those with large weights. The initial values for particle weights are usually the same and the particles are generated randomly. However it can be useful to initialize the particles in order to place them into the right part of the posterior density. Particle initialization is effective in the case of having high dimensional state space. This can also improve the speed of convergence.

### 3.4.4 Rao-Blackwellised Particle Filtering

The RBPFs are an extension of the PFs for which the state space is conditionally linear. The RBPF reduces the size of the state space by marginalizing out some of the variables analytically. Therefore, a reduced number of particles are needed for the RBPF to achieve the same performance as for the PF. Consider the case that it is possible to partition the state vector $\mathbf{x}_k$ as:

$$\mathbf{x}_k = \begin{bmatrix} \mathbf{x}_k^1 \\ \mathbf{x}_k^2 \end{bmatrix} \tag{3.19}$$

where $\mathbf{x}_k^1$ denotes the non-linear state variable and $\mathbf{x}_k^2$ denotes the state variable with conditionally linear dynamics. In order to see how RBPF works, consider the following linear Gaussian state space [85]:

$$\mathbf{x}_k^1 \sim p(\mathbf{x}_k^1|\mathbf{x}_{k-1}^1) \tag{3.20}$$

$$\mathbf{x}_k^2 = \mathbf{B}_{k-1}(\mathbf{x}_{k-1}^1)\mathbf{x}_{k-1}^2 + \mathbf{w}_{k-1}^2 \tag{3.21}$$

$$\mathbf{z}_k = \mathbf{C}_k(\mathbf{x}_k^1)\mathbf{x}_k^2 + \mathbf{v}_k \tag{3.22}$$

where $\mathbf{x}_k^1$ is a Markov process, $\mathbf{w}_{k-1}^2 \sim \mathcal{N}(0, \mathbf{Q}_{k-1}^w), \mathbf{v}_k \sim \mathcal{N}(0, \mathbf{Q}_k^v)$ and $\mathcal{N}(\boldsymbol{m}, \mathbf{P})$ is a Gaussian pdf of mean $\boldsymbol{m}$ and covariance $\mathbf{P}$. In equation (3.21), $\mathbf{B}_{k-1}(\mathbf{x}_{k-1}^1)$ represents a state transition for the linear state variable. In equation (3.22), $\mathbf{C}_k$ is a function of non-linear state variable that can be combined with the linear state variable to model the observation. Subject to a given $\mathbf{x}_k^1, \mathbf{x}_k^2$ is a linear Gaussian state space model.

Suppose the posterior density $p(\mathbf{x}_k^1, \mathbf{x}_k^2|\mathbf{z}_{1:k})$ can be factorized as:

$$p(\mathbf{x}_k^1, \mathbf{x}_k^2|\mathbf{z}_{1:k}) = p(\mathbf{x}_k^2|\mathbf{x}_k^1, \mathbf{z}_{1:k})p(\mathbf{x}_k^1|\mathbf{z}_{1:k}) \tag{3.23}$$

Here $p(\mathbf{x}_k^2|\mathbf{x}_k^1, \mathbf{z}_{1:k})$ is analytically tractable and can be computed by the KF. In addition, $p(\mathbf{x}_k^1|\mathbf{z}_{1:k})$ can be estimated using PF [83]. The RBPF results in a lower variance of the estimates compared with that of the commonly used PF. Given a conditionally linear Gaussian state space model and using the KF, the mean ($\boldsymbol{\mu}_k$) and covariance ($\mathbf{P}_k$) of the linear state variable $\mathbf{x}_k^2$ can be estimated as follows [85]:

$$\boldsymbol{\mu}_{k|k-1} = \mathbf{B}_{k-1}(\mathbf{x}_{k-1}^1)\boldsymbol{\mu}_{k-1} \tag{3.24}$$

$$\boldsymbol{\mu}_k = \boldsymbol{\mu}_{k|k-1} + \mathbf{K}_k(\mathbf{z}_k - \mathbf{C}_k(\mathbf{x}_k^1)\boldsymbol{\mu}_{k-1}) \tag{3.25}$$

$$\mathbf{P}_k = \mathbf{P}_{k|k-1} - \mathbf{K}_k\mathbf{C}_k(\mathbf{x}_k^1)\mathbf{P}_{k|k-1} \tag{3.26}$$

$$\mathbf{K}_k = \mathbf{P}_{k|k-1}\mathbf{C}_k^T(\mathbf{x}_k^1)(\mathbf{C}_k(\mathbf{x}_k^1)\mathbf{P}_{k|k-1}\mathbf{C}_k^T(\mathbf{x}_k^1) + \mathbf{Q}_k^v)^{-1} \tag{3.27}$$

$$\mathbf{P}_{k|k-1} = \mathbf{B}_{k-1}(\mathbf{x}_{k-1}^1)\mathbf{P}_{k-1}\mathbf{B}_{k-1}^T(\mathbf{x}_{k-1}^1) + \mathbf{Q}_{k-1}^w \tag{3.28}$$

## 3.5 Summary

In this chapter the tools and algorithms for mental fatigue analysis considering two directions based on EEG and ERP signals are explained in which new approaches for mental fatigue analysis are also suggested. These approaches are exploited in the following chapters. Finally the fundamentals of PF, KF, and RBPF are explained. These tracking based algorithms are used in the following chapters for specific purposes.

# Chapter 4

# Estimation of EEG Phase Synchronization with Application to Mental Fatigue

## 4.1 Introduction

EEG is the recorded electrical activity of the brain that enables the study of brain functions and it is a valuable source of information for the study of mental fatigue. As it is stated in Chapter 3, Section 3.2, recorded EEGs can be used for measuring synchronization of different brain regions and therefore evaluation of mental fatigue. These measurements represent the connectivity among various brain lobes. In this chapter we seek to measure the linear and non-linear synchronization of different brain regions by exploiting EMD algorithm [54]. Then, a new and effective approach for mental fatigue analysis based on phase synchronization and coherence is presented.

EMD as a fully adaptive and data-driven method for analysing non-linear systems and non-stationary time series, is presented for decomposing the single-channel EEG signal into its oscillations. Based on the proposed approach, first a brain region is selected and then the EMD algorithm, as a signal-dependent decomposition method, is applied to one channel of the EEG time series in the selected region to decompose it to a number of waveforms modulated in amplitude and frequency. The iterative extraction of these components called intrinsic mode functions (IMFs), is based on local representation of the signal as sum of a local oscillating component and a local trend.

The IMFs can be considered as the reference signals for the brain rhythmic activities. The EMD algorithm is applied to the desired channel and each time, based on the resulted instantaneous frequencies as explained in Section 4.5.1, one of the extracted IMFs is considered as the EEG activity in a certain frequency band. One important issue is that the extracted IMFs might be noisy. This noise is more destructive for signals of higher frequencies since the noise distorts zero-crossings of the signals, which are crucial in IMF estimation. In some researches, some conventional filtering techniques are suggested to remove the noise from the IMFs. This may result in loss of phase information which is crucial for our application.

Among filtering methods, ALE is an established adaptive approach for restoration of cyclic signals [86]. Here, we apply the ALE to the resulted IMF which may contain wide-band noise. Since the ALE exploits the cyclic nature of the IMFs, enhancement of the IMF by ALE is more effective than filtering it using conventional filtering even if the filter is zero-phase. Therefore, the IMFs can be filtered by an ALE algorithm. In addition, the superiority of using ALE to conventional filtering has been tested using simulated signals.

Then, by applying Hilbert transform (HT) to several enhanced IMFs from different parts of the brain, the linear and non-linear synchronization measures are estimated. These measures can be estimated using the selected IMFs in different brain regions for the subject before and during fatigue state. These measures are important for detecting and evaluating the mental fatigue in real world applications. The changes in linear and non linear synchronization levels are estimated for determination of the fatigue state.

The remainder of the chapter is structured as follows. In Section 4.2 the EMD is described. Then, in Section 4.3 the ALE method is briefly explained and in Section 4.4, the linear and non-linear synchronization measures are explained. Experimental results using EMD enhancement followed by the estimation of synchronization measures are discussed in Section 4.5. In Section 4.6 a new method for estimation and tracking of instantaneous phase (IP) of the EEG oscillations is proposed. This method should be further developed in the future studies in order to make it applicable for mental fatigue analysis. Finally, Section 4.7 concludes the chapter.

## 4.2 Empirical Mode Decomposition

EMD [54] is a non-linear technique which is applied to non-stationary signals in order to represent them as sum of their IMFs. Each resulted IMF by the EMD method satisfies two basic conditions: (i) in the complete data set, the number of extrema and the number of zero crossings must be the same or differ at most by one, (ii) at any point, the mean value of the envelope defined by the local maxima and the envelope defined by the local minima is zero. The EMD algorithm [87] for the signal $z(t)$ can be summarized as follows:

1. *Set* $g_1(t) = z(t)$
2. *Detect the extrema (both local maxima and local minima) of* $g_1(t)$
3. *Generate the upper and lower envelopes* $e_m(t)$ *and* $e_l(t)$ *respectively by connecting the maxima and minima separately with cubic spline interpolation* [88]
4. *Determine the local mean as:* $m(t) = \frac{e_m(t)+e_l(t)}{2}$
5. *IMF should have zero local mean; subtract m(t) from the original signal as:* $g_1(t) = g_1(t) - m(t)$
6. *Decide whether* $g_1(t)$ *is an IMF or not by checking the two basic conditions as described above*
7. *Repeat step 2 to 6 and stop when an IMF* $g_1(t)$ *is obtained.*

Once the first IMF is derived, define $d_1(t) = g_1(t)$, which is the smallest temporal scale in $z(t)$. For obtaining the rest of the IMF components, generate the residue $r_1(t)$ of the data by subtracting $d_1(t)$ from the signal as: $r_1(t) = z(t) - d_1(t)$. $r_1(t)$ is considered as the new data and subjected to the sifting process (steps 1 to 5) as explained above. Here, the stopping criterion (for the sifting process) proposed in [89] has been used. The process of extracting IMFs is terminated when the final residue is a constant, monotonic function, or a function with only one maxima and one minima that no more IMF can be obtained. At the end of the decomposition the signal $z(t)$ is represented as:

$$z(t) = \sum_{p=1}^{M} d_p(t) + r_M(t) \tag{4.1}$$

where $M$ is the number of IMFs and $r_M(t)$ is the final residue. The EMD algorithm is applied to one channel of EEG data each time to decompose it to different rhythms. In some cases, especially for the first generated IMFs, the IMF is noisy and contains some wide-band noise. Here, it is suggested to use the ALE in order to enhance the IMF. In the next section the adaptive line enhancer algorithm is described briefly.

## 4.3 Adaptive Line Enhancer

The aim of an ALE is to retain the narrow-band components in the observed data with the aim of reducing or removing any broadband components [86]. The only assumption that is required for operation of the ALE is that the signal of interest should be narrow-band [86]. Since the ALE is adaptive, it is able to track non-stationary signals. There are many applications such as sonar, biomedical, and speech signal processing which make use of ALE. A block diagram of an ALE system considering its usage in our application, for denoising and enhancing the

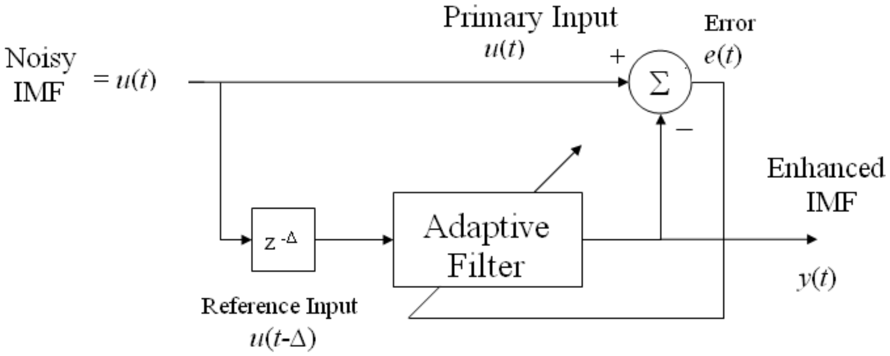

Figure 4.1: Block diagram of an adaptive line enhancer system for denoising and enhancing an IMF.

IMF, is shown in Fig. 4.1. The ALE can be considered as a degenerate form of the adaptive noise canceller. The reference signal in the ALE, instead of being generated separately as in the adaptive noise canceller, is a delayed version of the input signal [55].

Therefore, the delay $\Delta$ is considered as the prediction depth of the ALE and is measured in units of the sampling period. A transversal filter is used to process the reference input $u(t-\Delta)$ for generating the error signal $e(t)$, which is defined as the difference between the actual input $u(t)$ and the ALE's output. In our application $\Delta$ is equivalent to a multiple of the cycle period of the desired IMF. The error signal is used in the adaptive algorithm to adjust the weights of the transversal filter, mainly according to Widrow's least mean square (LMS) algorithm [55]. The tap-weight adaptation can be written as:

$$\mathbf{w}(t+1) = \mathbf{w}(t) + \mu\mathbf{u}(t-\Delta)e(t) \tag{4.2}$$

where $\mathbf{w}(t)$ is the coefficient vector at time $t$, $\mu$ is the step size, $e(t)$ is the adaptation error and $\mathbf{u}(t-\Delta)$ is the input vector, respectively, at time $t$. In the case of a fixed step size LMS algorithm, $\mu$ is chosen as a constant. The extracted IMFs by the EMD algorithm applied to the EEG signals, each varies around certain frequency. So they are narrow-band. The mode change may cause shift in the frequencies between nearby IMFs which still makes the IMF narrow-band. Therefore, we can apply the ALE to those extracted IMFs which are noisy. After applying the ALE to the IMFs, it is possible to compute the synchronization measures of the different enhanced IMFs obtained from different parts of the brain. In the next section the linear and non-linear synchronization measures are explained.

## 4.4 Synchronization Measures

### 4.4.1 Linear Measure of Synchronization

Suppose we have two IMFs simultaneously obtained from different channels. Every IMF is a real valued signal. The discrete HT [54] is used to compute the analytic signal for an IMF. The discrete HT denoted by $\mathbf{H}_d[.]$ of signal $x(t)$ is defined as:

$$\mathbf{H}_d[x(t)] = \sum_{\substack{\delta=-\infty \\ \delta\neq t}}^{+\infty} \frac{x(\delta)}{t-\delta} \tag{4.3}$$

The analytic version of the $i^{th}$ IMF $d_i(t)$ is defined as:

$$c_i(t) = d_i(t) + J\mathbf{H}_d[d_i(t)] = a_i(t)e^{J\theta_i(t)} \tag{4.4}$$

where $J = \sqrt{-1}$ and $a_i(t)$ and $\theta_i(t)$ are the instantaneous amplitude (IA) and IP of the $i^{th}$ IMF respectively. The analytic signal is used for determining the instantaneous quantities such as energy, phase, and frequency. The discrete time instantaneous frequency (IF) of the $i^{th}$ IMF is then defined as the derivative of the phase $\theta_i(t)$ calculated at $t$:

$$\omega_i(t) = \frac{d\theta_i(t)}{dt} \tag{4.5}$$

Distribution of the signal energy as a function of time and frequency is represented by the Hilbert Spectrum (HS). If we partition the frequency range into $k$ frequency bins, then, HS of the $i^{th}$ IMF can be defined as the IA of the IMF at the $k^{th}$ frequency bin:

$$h_i(k,t) = a_i(t)v_i^k(t) \tag{4.6}$$

where the $v_i^k(t)$ takes the value 1 if $\omega_i(t)$ falls within $k^{th}$ band, otherwise, $v_i^k(t) = 0$. The marginal spectrum corresponding to the HS $h_i(k,t)$ of the $i^{th}$ IMF is defined as:

$$\psi_i(k) = \sum_{t=1}^{T} h_i(k,t) \tag{4.7}$$

where $T$ is the length of the data. Using this information, the coherence function, which gives a measure of linear synchronization between the two IMFs, can be defined as:

$$\zeta_{ij}(k) = \frac{|\chi_{i,j}(k)|^2}{\psi_i(k)\psi_j(k)}; k = 1, 2, ..., B \tag{4.8}$$

where $B$ is the number of frequency bins, $\chi_{i,j}(k)$ is the cross spectrum of the $i^{th}$ and $j^{th}$ IMFs, $\psi_i(k)$ and $\psi_j(k)$ are the marginal power spectra of the $i^{th}$ IMF and $j^{th}$ IMF respectively. $\zeta_{ij}(k)$ is a quantitative measure of how much the $i^{th}$ IMF is correlated with the $j^{th}$ IMF.

### 4.4.2 Non-linear Measure of Synchronization

It is possible that two dynamic systems have synchronized phases while their amplitudes are uncorrelated [90]. Therefore, it is useful to consider phase synchronization as a non-linear measure of synchronization. Two signals are phase synchronized if the $(n, m)$ difference between their phases remains constant across time [91]. For simplicity, it is possible to assume that $m$ and $n$ are equal to 1. After finding the IP of the $i^{th}$ and $j^{th}$ IMFs, the phase synchronization measure can be defined as:

$$\gamma_{ij} = |\langle e^{J\theta_{ij}(t)}\rangle_t| = \sqrt{\langle cos\theta_{ij}(t)\rangle_t^2 + \langle sin\theta_{ij}(t)\rangle_t^2} \tag{4.9}$$

where $\langle . \rangle$ denotes average over time, $\theta_{ij}(t) = \theta_i(t) - \theta_j(t)$, and $\theta_i(t)$ is the IP of the $i^{th}$ IMF obtained by HT. In this case, $\gamma_{ij}$ will be zero if the phases are not synchronized at all and will be one when the phase difference is constant (perfect synchronization). The key feature of $\gamma_{ij}$ is that it is only sensitive to phases, regardless of the amplitude of each signal.

## 4.5 Experimental Results

In this section, first the validity and superiority of the enhanced EMD algorithm using ALE to the conventional filtering have been tested for a set of simulated data. Then, a set of real EEG data of a subject which goes under fatigue is analysed in order to detect the changes of synchronization during the fatigue state.

### 4.5.1 Simulated Data

To simulate a single channel EEG, four frequency and amplitude modulated sine waves belonging to four different frequency bands were generated and added together.

Then, the Gaussian noise was added to the generated signal. The SNR for the generated signal is approximately 7dB. This noisy mixture signal is plotted in Fig. 4.2(a). We have applied the EMD to the simulated EEG signal. In order to show the effectiveness of the method, the ALE was applied to the extracted IMFs. Since using the average of instantaneous frequencies the second extracted

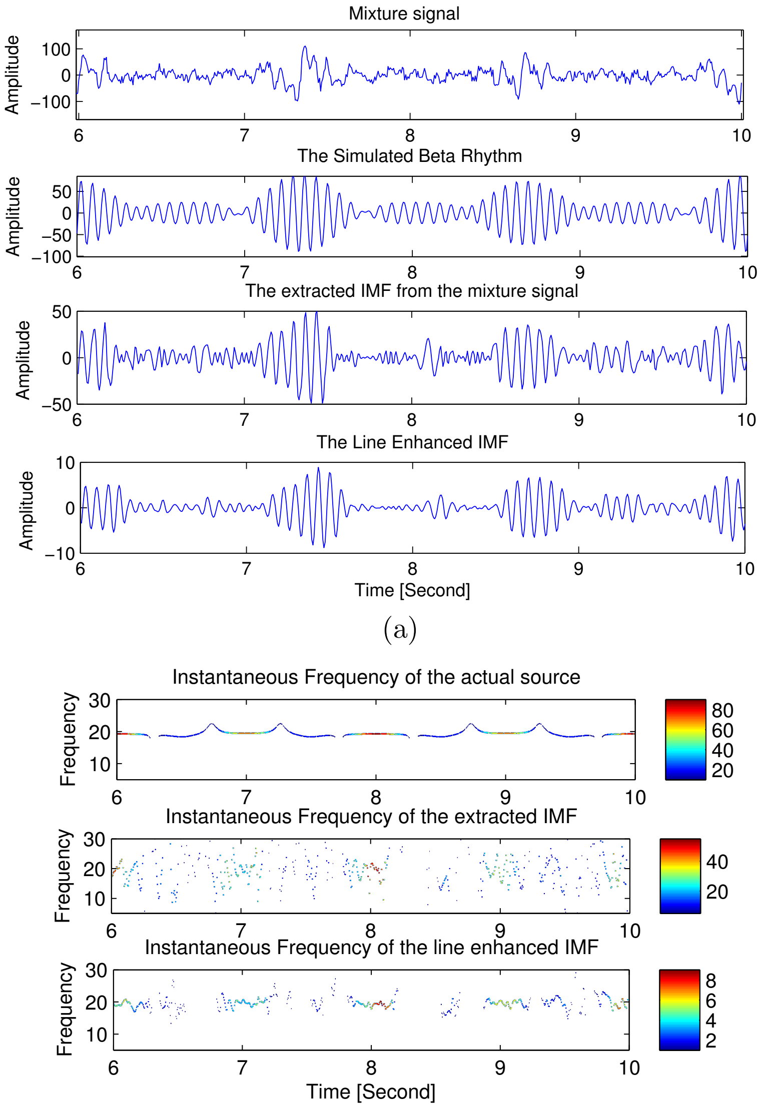

(a)

(b)

Figure 4.2: (a) The noisy mixture signal (first), actual EEG oscillation in beta frequency band (second), the extracted IMF (third), and the line enhanced IMF (fourth). (b) The resulted HS of the actual source (top), extracted IMF (middle) and the line enhanced IMF (bottom). The colour bar represents the instantaneous amplitude.

IMF belonged to the beta frequency band range around 20 Hz, we selected that IMF as beta rhythm and plotted its HS in Fig. 4.2(b). From the HS it can be seen that the IMF contains some wide-band components. We then applied the ALE algorithm to the extracted IMF and computed the HS again and plotted the results. Since a number of iterations are needed at the beginning for the algorithm to converge, the ALE is applied to a window of longer size then the resulted signal by the ALE is truncated. The HS of the actual EEG oscillation in beta frequency band, extracted IMF, and the enhanced IMF are shown in Fig. 4.2(b). From the plots in this figure it is evident that using the proposed approach the wide-band noise has been reduced.

We calculated the correlation coefficient of the original simulated oscillation with both the IMF and the enhanced IMF. In addition, we used a Butterworth filter and a zero-phase filter of different degrees to filter the extracted IMF and computed the correlation coefficients of the filtered IMF and the original oscillation. The highest correlation coefficient of 0.9137 was obtained by the IMF which was filtered using the ALE. In the next section, we apply the enhanced EMD algorithm to different channels and compute the synchronization measures of the brain lobes before and during fatigue state in order to evaluate the corresponding synchronization changes.

### 4.5.2 Real Data

The EEG data were recorded from participants who reported to be non-smokers, to have normal sleep patterns, not to work night shifts, and not to use any prescribed medication. From previous studies it is known that the participants become more distracted by the information presented at irrelevant spatial locations with increasing mental fatigue (e.g. see [92]). Therefore, in each trial a horizontal array of three uppercase letters was presented to the subjects in which the central one was the relevant target letter and the remaining letters were distractors. The participants were instructed to make a left-hand response as quickly as possible if the target letter was an H and a right-hand response if the central letter was an S and to ignore distractors. The letter array remained on the screen until a response was given.

In the case that there was no response from the participants, the letter array disappeared after 1200 ms. The focus of attention can be manipulated by advance information [93]. To examine whether individuals still use available information to prepare for upcoming activities after a prolonged task performance, an explicit cue was presented for 150 ms, 1000 ms before appearance of the three letters specifying either the color of the target letter (the Dutch word for ‘red’ or ‘green’) or the response hand (the Dutch word for ‘left’ or ‘right’). The hand

and color cues were presented randomly with equal probability.

In half of the trials the distractors had the same identity and color as the target letter (e.g., HHH or SSS: compatible) while in the other half of the trials they had a different identity and color than the target letter (e.g., SHS or HSH: incompatible). The stimuli of different types were presented randomly with equal probability. During each trial a fixation mark remained visible on the screen (an asterisk of 0.5 × 0.5 cm). The interval between the initial response to one trial and the beginning of cue presentation on the following trial varied randomly between 900 and 1100 ms. The subjects were instructed to have a fast and accurate response and minimize the eye movements and blinking during the task performance.

The task lasted as a two-hour experimental block without breaks preceded by a practice block of 80 trials. EEG data was recorded from 22 scalp positions, using Sn electrodes attached to an electrode cap. Electrode positions based on extended 10-20 system were F7, F3, Fz, F4, F8, T7, C3, Cz, C4, T8, P7, P3, Pz, P4, P8, O1, Oz, and O2. Additional intermediate positions were FC5, FC1, FC2, and FC6. The electrodes were referenced to electronically linked earlobes. Electro-oculograms (EOG) were recorded bipolarly with Sn electrodes from the outer canthi of both eyes and from above and below the left eye. By adding gel, electrode impedances were reduced to less than $5k\Omega$. The signals were lowpass filtered with the cutoff frequency set at 30 Hz and sampled at a rate of 100 Hz.

Fifteen healthy young women with age ranging from 19 to 25 years participated in the experiment. The EEG data of one of the subjects is selected. Then, two separate segments of data from the first half an hour and last half an hour are extracted. These segments are respectively, the representations of alert and fatigue states. Each segment is analysed separately to measure the linear synchronization (coherence) and non-linear synchronization (phase synchronization) between the left and right hemispheres. F7, FC5, P7 channels from the left hemisphere and F4, FC6, P8 from the right hemisphere are selected. The alpha rhythm is extracted from F7 and F4, beta rhythm is extracted from FC5 and FC6 and theta rhythm is extracted from P7 and P8. The overlapped windows with the length of 4 seconds are considered for applying the HT and estimating the coherence and phase synchronization.

Selection of the channels in each hemisphere for extracting each rhythm is based on the HT of the resulted IMFs in several electrodes in the right and left part of the brain. The IMF is selected from the channel that its resulted IMF (in a certain frequency band) has frequency traces in time-frequency distribution which are more continuous. Since the resulted beta rhythm was rather noisy, the ALE was used to enhance it.

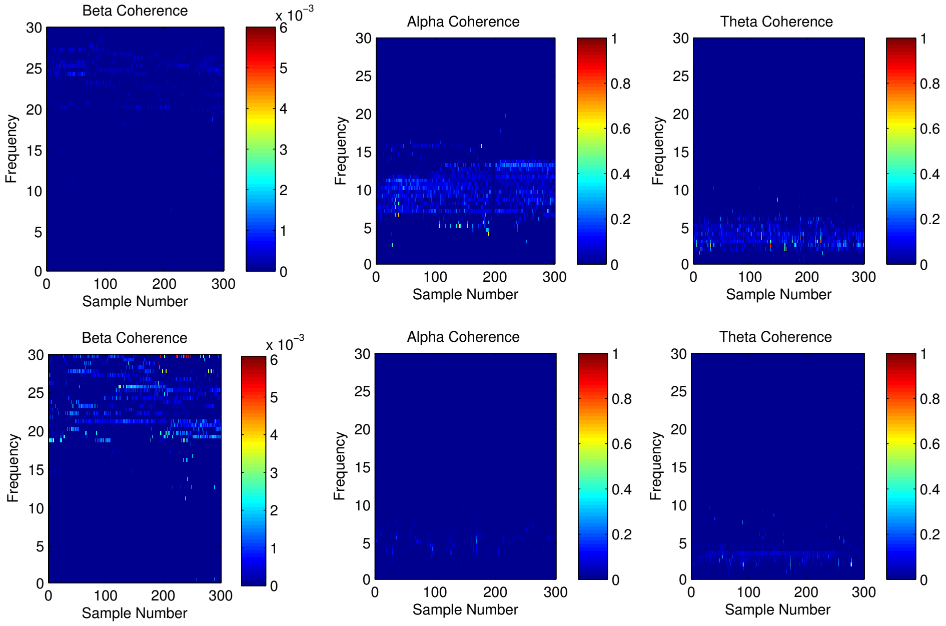

Figure 4.3: Interhemisphere coherence of beta, alpha and theta rhythms, the top row corresponds to the fatigue state and the bottom row corresponds to the alert state.

The results of the estimated coherence and phase synchronization values for the two segments of the data are shown in Fig. 4.3 and Fig. 4.4. The algorithm is repeated over more trials for alert and fatigue states. Approximately, in all of the trials the coherence of beta rhythms between the left and right hemisphere decreases and the coherencies for alpha and theta rhythms increase from the alert to fatigue state. The estimated phase synchronization values between rhythms have been shown to be different across different trials especially for theta rhythm. However in most trials, the phase synchronization of beta rhythms decreases while for alpha rhythms it increases from the alert to fatigue state.

In addition, we measured the phase synchronization and coherence around stimulus onset before and during fatigue state. Since the segment of data around stimulus onset is considered for measuring phase synchronization and coherence, the length of the data segment is reduced to only one second before stimulus onset and one second after stimulus onset. However for applying the EMD a longer window size is considered while for measuring phase synchronization the window size is reduced since the timing between the consecutive stimuli is very short (from 1 second to 2 seconds).

We considered 3 seconds of the data segment after stimulus onset and applied the EMD. For beta rhythm, ALE is applied to the resulted IMF. One second

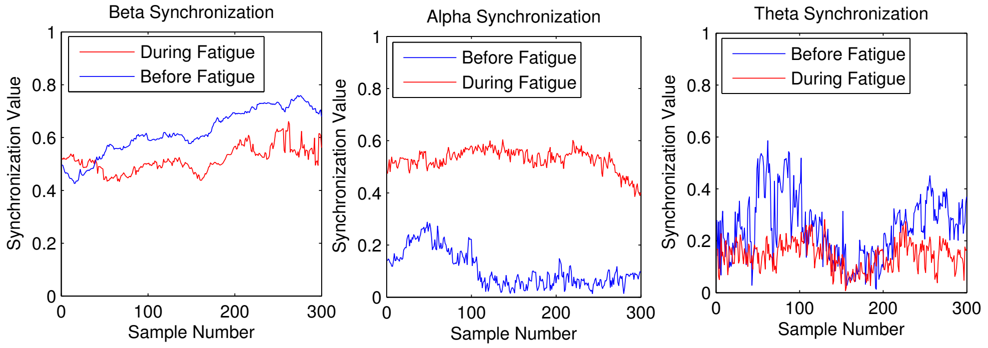

Figure 4.4: Interhemisphere phase synchronization of beta (left), alpha (middle), and theta (right) rhythms.

of data segment before stimulus onset and one second after stimulus onset are considered for measuring phase synchronization. Beta and theta rhythms are extracted from F3 and F4 channel and alpha rhythm is extracted from C3 and C4 channels. The phase synchronization is measured for five trials one second before and after stimulus onset. The results are shown in Fig. 4.5. The averaged phase synchronization is also depicted as the thick line. From these figures it can be seen that the best discrimination is obtained considering phase synchronization of the alpha rhythm. Also as the frequency of the rhythm decreases (e.g. from beta to theta rhythm) the variance of the consecutive measured phase synchronization across time increases. The coherence of beta, alpha, and theta rhythms are measured around the stimulus onset for five trials and the averaged coherence for all the rhythms are shown in Fig 4.6, Fig 4.7 and Fig 4.8.

It can be seen from these figures that there is not a good discrimination in coherence before and during fatigue state. Therefore, considering the above experiments, the window length size plays an important role. Reduced window length size (e.g. one second) is not effective when measuring coherence. The best discrimination with respect to phase synchronization is obtained for the alpha rhythm. However all the phase synchronization measures can have an important role for detecting the fatigue state. This can be done by selecting a regression or a classification method and using the extracted phase synchronization in different frequency bands from different regions of the brain. The coherence measure, if included, should not be considered around the stimulus onset and the window size should not be small (e.g. one second).

In the next section, a new method is developed for estimation and tracking the IP of the EEG oscillations. This method is in the initial stage and should be improved in the future to be applied for estimation of EEG phase synchronization with application to mental fatigue analysis.

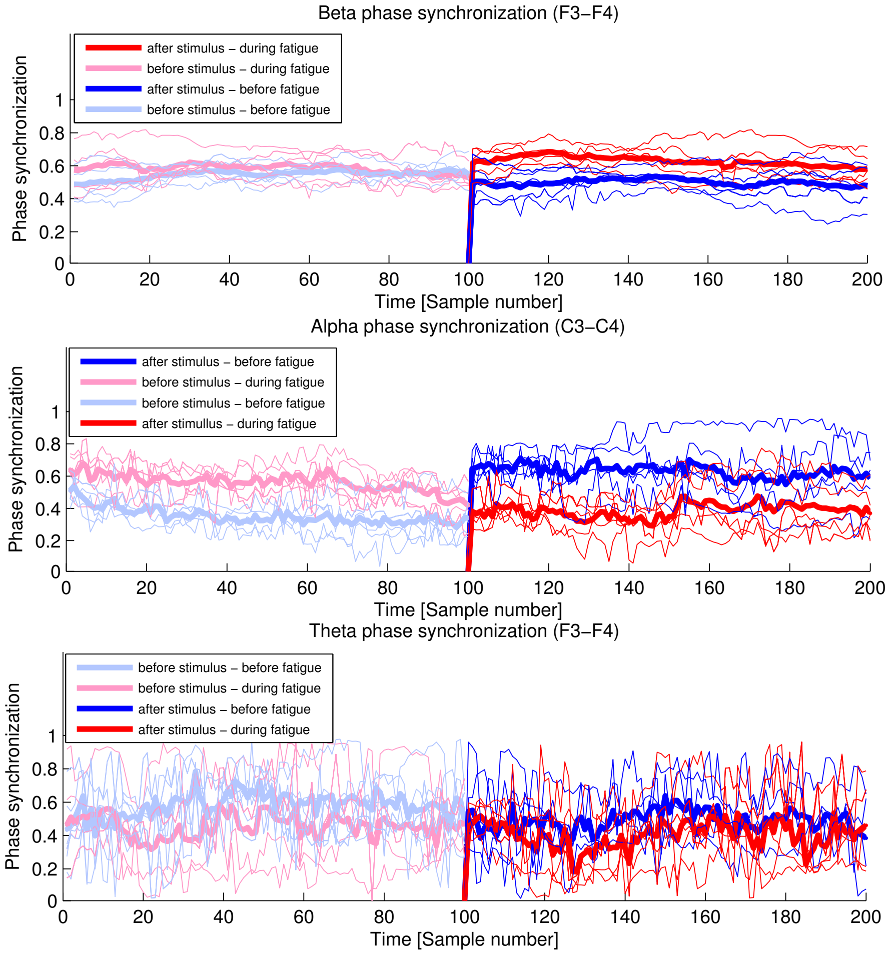

Figure 4.5: Phase synchronization of beta (top), alpha (middle), and theta (bottom) rhythms around stimulus onset.

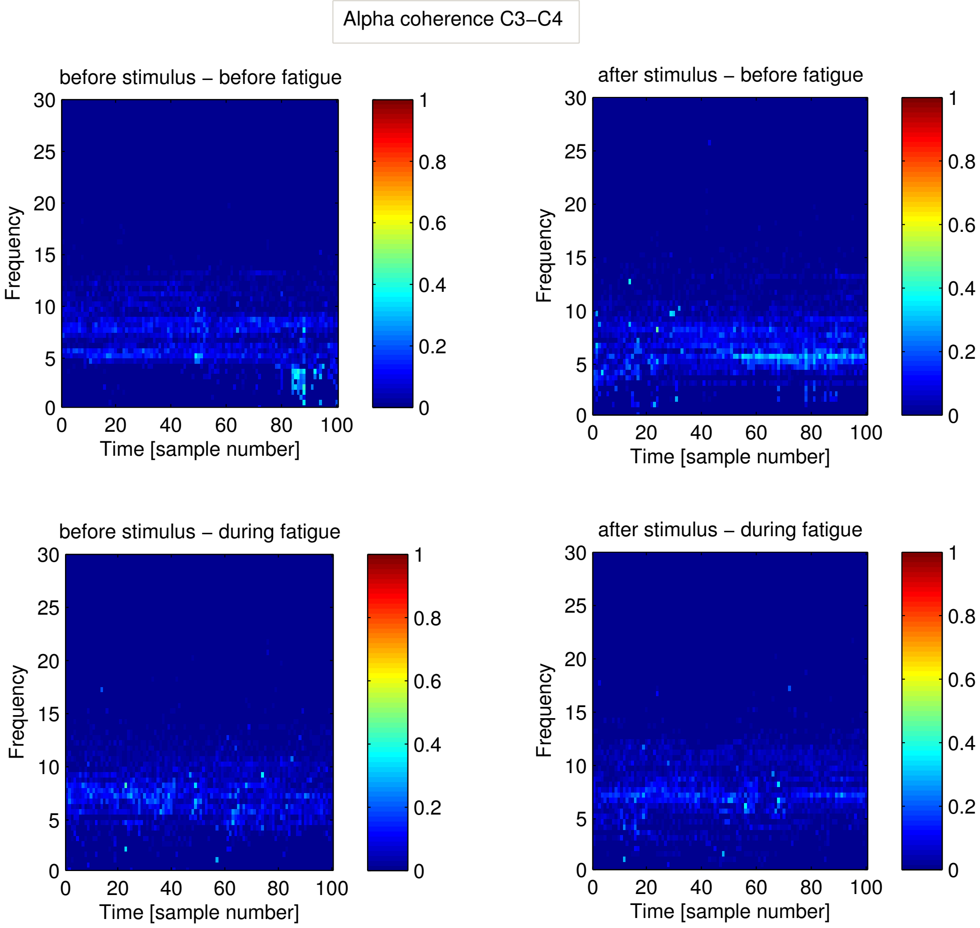

Figure 4.6: Coherence of alpha rhythm around stimulus onset for before fatigue (top row) and during fatigue (bottom row). Dark blue colour presents lack of coherence and dark red colour presents the maximum coherence.

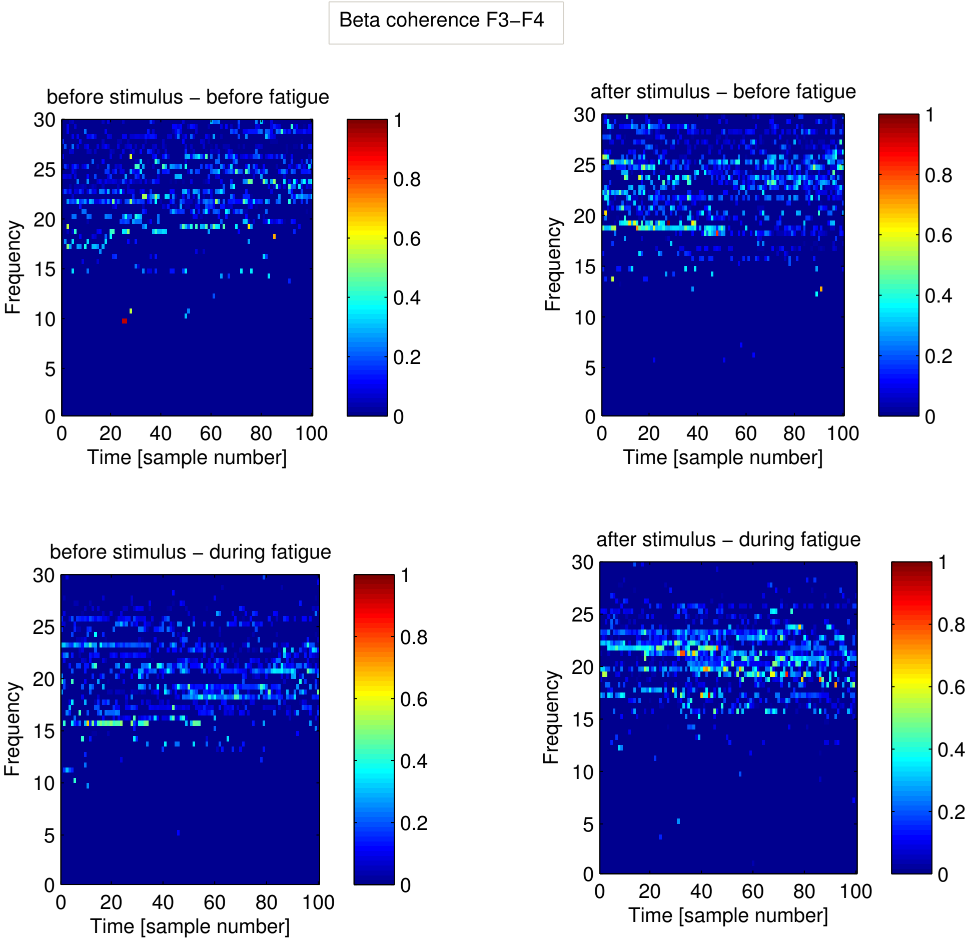

Figure 4.7: Coherence of beta rhythm around stimulus onset for before fatigue (top row) and during fatigue (bottom row). Dark blue colour presents lack of coherence and dark red colour presents the maximum coherence.

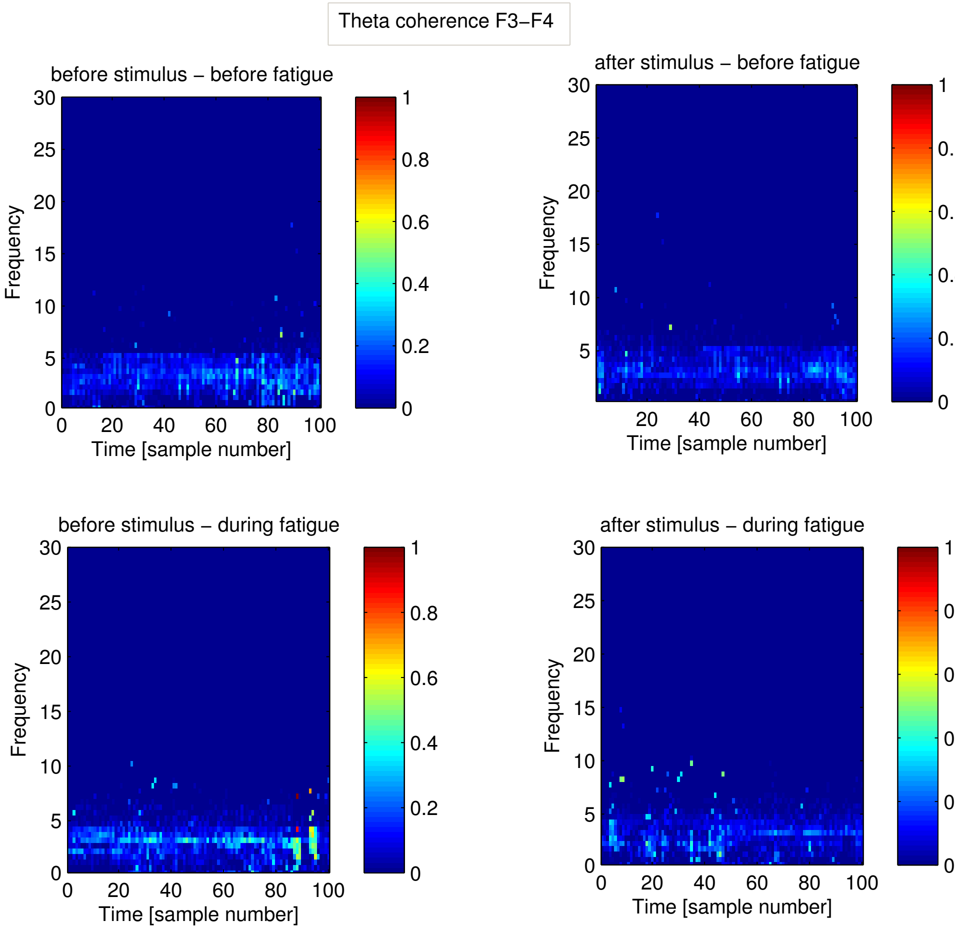

Figure 4.8: Coherence of theta rhythm around stimulus onset for before fatigue (top row) and during fatigue (bottom row). Dark blue colour presents lack of coherence and dark red colour presents the maximum coherence.

## 4.6 Instantaneous Phase Tracking of EEG Oscillations using EMD and RBPF

In this section, a new method for IP tracking of oscillatory signals in a narrow band frequency range is proposed. EMD as an adaptive and data-driven method for analysing non-linear and non-stationary time series, is applied to a mixture of signals. Then, one of the resulted IMFs is used for estimating the IP of the signal in a certain frequency band.

Since by applying EMD to the noisy signal, the noise is distributed over the IMFs, the RBPF is used to track the actual IP of the noisy IMF. The formulated RBPF operates based on smoothing the IF traces in Hilbert domain and denoising the signal in time domain. Finally, the method is able to track the IP across consecutive time points. The method is applied to both simulated and real data. As an application, in future it can be used for mental fatigue analysis based on the changes in phase synchronization of different brain rhythms in different brain regions before and during the fatigue state.

Decomposition of signals into their constituent oscillatory components has wide applications in various fields. This may be efficiently performed using EMD and often to restore the resulted IMFs from noise. As stated in the first section of this chapter, in some previous research conventional filtering is suggested for removing the noise from the IMF which usually results in deteriorating the phase information. In [94] a number of EMD-based denoising inspired by the standard wavelet thresholding is proposed. In the previous section ALE was proposed and applied to the IMF in order to enhance and de-noise it. HT is then used for estimation of IP. In this section we propose a new method based on RBPF in order to directly estimate the IP of the IMF. The method can be used as a general de-noising algorithm but the focus in this section is to estimate the IP from the noisy IMF. Since the algorithm requires setting a few parameters, for measuring phase synchronization using the proposed method, the parameters should be selected carefully.

EMD is applied to the EEG signal in order to extract its different oscillations. Our proposed method in the first step uses the EMD in order to decompose the EEG into the IMFs. The method tries to smooth the frequency traces in Hilbert domain and estimate the phase. In the next subsections, first the problem formulation using RBPF is provided and then the simulation and real data results are presented.

### 4.6.1 Problem Formulation using RBPF

Suppose that EMD is applied to the mixture signal $\mathbf{x}$ to decompose it to its corresponding IMFs. Then the HT is used to compute the analytic signal for the IMFs (having the IMF as the real part and its HT as the imaginary part, see equation (4.4)) as:

$$d_t(i) + J\mathbf{H}_d[d_t(i)] = a_t(i)e^{J\theta_t(i)} \quad i = 1, ..., M \tag{4.10}$$

where $J = \sqrt{-1}$ and $a_t(i)$ and $\theta_t(i)$ are the IA and IP of the $i^{th}$ IMF respectively, $\mathbf{H}_d[.]$ denotes the HT, and $M$ is the number of IMFs. Then, the mixture signal can be reconstructed as:

$$x(t) = \sum_{i=1}^{M} d_t(i) = Real(\sum_{i=1}^{M} a_t(i)e^{J\theta_t(i)}) \tag{4.11}$$

Now, it is possible to formulate the IA and IP of each IMF as the state variables of the PF [83] and the mixture signal as the observation. Therefore, the state transition and observation equations of the PF can be expressed as:

$$\boldsymbol{\rho}_t = [\theta_t(1) \quad a_t(1) \quad \dots \quad \theta_t(M) \quad a_t(M)] \tag{4.12}$$

$$\boldsymbol{\rho}_t = f(\boldsymbol{\rho}_{t-1}) + \mathbf{w}_{t-1} \tag{4.13}$$

$$x(t) = G(\boldsymbol{\rho}_t) + \mathbf{v}_t \tag{4.14}$$

where $x(t)$ is the mixture signal, $\mathbf{v}_t, \mathbf{w}_{t-1}$ are WGN with known covariance matrices $\mathbf{Q}_t^v$ and $\mathbf{Q}_{t-1}^w$ respectively, $M$ is the number of IMFs and

$$G(\boldsymbol{\rho}_t) = Real(\sum_{i=1}^{M} a_t(i)e^{J\theta_t(i)}) \tag{4.15}$$

From the above equations it can be seen that it is possible to partition the state variables into linear and non-linear parts. Therefore, we formulate the problem using the concept of RBPF [85]. The RBPF marginalizes out the linear state variables in order to reduce the size of the state space. Therefore, a reduced number of particles are required for the RBPF to achieve the same performance as for the PF. We rewrite equation (4.12) as:

$$\boldsymbol{\rho}_t = [\boldsymbol{\rho}_t^1 \quad \boldsymbol{\rho}_t^2] \tag{4.16}$$

$$\boldsymbol{\rho}_t^1 = [\theta_t(1) \quad \dots \quad \theta_t(M)] \tag{4.17}$$

$$\boldsymbol{\rho}_t^1 = [a_t(1) \quad \dots \quad a_t(M)] \tag{4.18}$$

where $\boldsymbol{\rho}_t^1$ is the non-linear state variable and $\boldsymbol{\rho}_t^2$ is the linear state variable. Then, the state transition and observation equations can be written in the vector form as:

$$\begin{aligned} \boldsymbol{\rho}_t &= f(\boldsymbol{\rho}_{t-1}) + \mathbf{w}_{t-1} \\ x(t) &= G(\boldsymbol{\rho}_t) + \mathbf{v}_t \\ G(\boldsymbol{\rho}_t) &= \boldsymbol{\rho}_t^2 G'(\boldsymbol{\rho}_t^1) \\ &= [a_t(1) \quad \dots \quad a_t(M)] \begin{bmatrix} Real(e^{J\theta_t(1)}) \\ \dots \\ Real(e^{J\theta_t(M)}) \end{bmatrix} \end{aligned} \tag{4.19}$$

$\boldsymbol{\rho}_t^2$ is estimated using KF [83] and $\boldsymbol{\rho}_t^1$ is estimated by PF. Considering the above equations, if the state transition function $f$ were available, it would be possible to track the IA and IP of each IMF and de-noise the mixture signal using RBPF. However, the state transition function is not known and especially for phase it cannot be modelled simply using a Markov process. Therefore, first we utilize the RBPF in order to formulate the problem and then several equations and constraints are employed to the RBPF algorithm in order to track the IP effectively.

Here we focus on the phase tracking from one IMF. In future, the method can be extended to track the IP and IA of multiple IMFs at each time point. Suppose that we applied EMD to one channel of EEG signal as $x(t)$. Usually the first and second IMFs are noisy since they contain the highest frequency available in the signal. If we compute the analytic signal using equation (4.10), the IF of the IMF can be estimated using derivative of the phase (see equation (4.5)). In the following it is shown that for the noisy IMF, the frequency trace across time points is not smooth and the effect of wide band noise can be clearly seen when there is a jump in the estimated IF of the time samples. We select the $i^{th}$ IMF which is noisy. Therefore, the state variables, state transition, and observation function can be considered as:

$$\boldsymbol{\rho}_t(i) = [\theta_t(i) \quad a_t(i)],\ \rho_t^1(i) = \theta_t(i),\ \rho_t^2(i) = a_t(i) \tag{4.20}$$

$$\begin{aligned} \boldsymbol{\rho}_t(i) &= \widetilde{f}(\boldsymbol{\rho}_{t-1}(i)) + \mathbf{w}_{t-1} \\ imf_t(i) &= \widetilde{G}(\boldsymbol{\rho}_t(i)) + \mathbf{v}_t \\ \widetilde{G}(\boldsymbol{\rho}_t(i)) &= a_t(i) Real(e^{J\theta_t(i)}) \end{aligned} \tag{4.21}$$

Our proposed method tries to smooth the IF traces in Hilbert domain and then estimate the IP using the information provided by the IF. Each IMF belongs to a specified frequency band. So, it is possible to determine the minimum and maximum frequencies for the band in which IMF belongs to. By generating some simulated signals, applying the EMD, and evaluating the IP of the IMF using HT, it is evident that the phase sign suddenly changes across time points. However, if we consider the absolute value of the phase, the phase change is not significant. The IA is smooth across all time samples.

As shown in equation (4.20), we formulated the phase as the non-linear state variable and the amplitude as the linear state variable of the RBPF. Both of them are considered as the Markov process. We also save one variable as the estimated IF. This variable does not have a direct role in estimating the phase, however it is useful in updating the weight of some particles and deciding on the phase transition. When we generate new particles corresponding to the IP from the previous time point, we need to generate two phases. One phase is obtained from the phase in the previous time sample plus the state noise. Another phase is obtained from the negative of the phase in the previous time sample plus noise. Then, we calculate IFs for both generated phases. We select the generated phase in which the estimated IF smooths the frequency traces across time samples (using the stored IF estimate in the previous time point).

When we tried to test and develop the method using simulated signal, there was a situation that the phase in one time sample was close to zero and the phase in the next time sample was also close to zero. In this case the calculated frequency went out of the frequency range and became negative in the later time samples. Although in consecutive time points, the IF traces return to the actual track before becoming negative or going beyond the frequency range. In this situation the method is not able to distinguish the correct generated phase based on the frequency traces. We used some if-then-rules and detected the situation that the estimated phase is close to zero. Therefore in that situation the phase selection stems from considering the observation and the estimated amplitude by KF.

Before deciding on the generated phase (from positive/negative of the phase in previous time sample) we estimate the IA for both generated phases using KF. We update the weight of each particle using two scales. One scale relates to the frequency transition, the other scale relates to the weight given by using the observation and the amplitude estimated by KF. In the case where the generated frequency is out of band but still is a valid frequency and not related to noise (i.e. due to the phase transition around zero), we estimate another frequency from previous time point in order not to lose the frequency track.

Therefore, we cannot have an equivalent scale for frequency transition like the case that frequency is inside the specific band. However, we set the second scale equal to 1 to have better phase transition. Then, we select the generated phase in which the estimated weight is higher. We do not store the generated frequency which is negative or out of the frequency band. Instead, we generate a new frequency which is equal to the stored frequency in the previous time sample plus a Gaussian random generated number. In this case we do not lose the frequency track inside the band in the later time points and have better phase transition near zero.

In addition, our method involves some constraints. When the selected phase is larger than $\pi$ or smaller than $-\pi$ the weight of the particle will be set to zero in order not to have any contribution to the estimation of the posterior density. In addition, when the estimated frequency is out of the frequency band range, we set the weight of that particle to zero.

The pseudo-code of the proposed method for IP tracking of one IMF is shown in Algorithm 4.1. $\tau$ is the threshold to determine when the phase transition is near zero. In our simulation this was set to 0.15. We consider a window of length $T + 1$ and apply the EMD. After one noisy IMF is selected, the HT is applied to that IMF. We use the estimated IF, IP, and IA of the noisy IMF at the first time point and initialize the particles. This initialization moves the particles into the right part of posterior density and is helpful to speed up the convergence of the RBPF. The method is applied to the rest of $T$ time samples.

Algorithm 4.1 Pseudo-code for phase tracking of one IMF

```
select $i^{th}$ IMF as $d_t(i)$,   $n = 1, ..., N_s$, $N_s$ is the number of particles.
set $t = 0$ and generate random numbers $\theta_0^{(n)}$,$freq_0^{(n)}$
according to random uniform distribution considering the HT of the IMF.
Initialize $\sigma, \sigma_1$, $min_f$, $max_f$, $T_s$ (Sampling period),  $\tau$
for $\{t = 1$ to $t_{max}\}$ $\{t_{max}$ is the number of all time samples$\}$
  - generate random numbers $w_{t-1}^{\rho(n)_1}$,$w_{t-1}^{\rho(n)_2}$ and $q_{t-1}^{\rho(n)}$
  - set $\hat{\theta}_t^{(n)} = \theta_{t-1}^{(n)} + w_{t-1}^{\rho(n)_1}$
  - set $\breve{\theta}_t^{(n)} = -\theta_{t-1}^{(n)} + w_{t-1}^{\rho(n)_2}$
  - Calculate $freq1 = diff(unwrap\ [\theta_{t-1}^{(n)} \quad \hat{\theta}_t^{(n)}])/Ts/(2 \times \pi)$
  - Calculate $freq2 = diff(unwrap\ [\theta_{t-1}^{(n)} \quad \breve{\theta}_t^{(n)}])/Ts/(2 \times \pi)$
  - Estimate frequency $freq = freq_{t-1}^{(n)} + q_{t-1}^{\rho(n)}$
  - Set $\hat{\theta}_t^{(n)}$ as the phase, estimate amplitude $a_t^{(n)_1}$ by Kalman filtering
  - Set $f_1 = a_t^{(n)_1} \times Real(e^{J\hat{\theta}_t^{(n)}})$,
    $ws1 = exp\ (-(d_t(i) - f_1) \times (d_t(i) - f_1)/(2 \times \sigma_1^2))$
  - Set $\breve{\theta}_t^{(n)}$ as the phase, estimate amplitude $a_t^{(n)_2}$ by Kalman filtering
  - Set $f_2 = a_t^{(n)_2} \times Real(e^{J\breve{\theta}_t^{(n)}})$,
    $ws2 = exp\ (-(d_t(i) - f_2) \times (d_t(i) - f_2)/(2 \times \sigma_1^2))$
  - if $(|\hat{\theta}_t^{(n)}| < \tau$ and $|\theta_{t-1}^{(n)}| < \tau)$ or $(|\breve{\theta}_t^{(n)}| < \tau$ and $|\theta_{t-1}^{(n)}| < \tau)$
    $weight1 = ws1$, $weight2 = ws2$
    $freq1 = freq$ , $freq2 = freq$, $ws1 = 1$, $ws2 = 1$
  - else
    -$weight1 = exp\ (-(freq - freq1) \times (freq - freq1)/(2 \times \sigma^2))$
    -$weight2 = exp\ (-(freq - freq2) \times (freq - freq2)/(2 \times \sigma^2))$
  - end if
  - if $weight1 > weight2$
    $\theta_t^{(n)} = \hat{\theta}_t^{(n)}$,$a_t^{(n)} = a_t^{(n)_1}$, $freq_t^{(n)} = freq1$, $w_t^{(n)} = w_{t-1}^{(n)} \times ws1 \times weight1$
  - else
    $\theta_t^{(n)} = \breve{\theta}_t^{(n)}$,$a_t^{(n)} = a_t^{(n)_2}$, $freq_t^{(n)} = freq2$, $w_t^{(n)} = w_{t-1}^{(n)} \times ws2 \times weight2$
  - end if
  - if $(\theta_t^{(n)} > \pi)$ or $(\theta_t^{(n)} < -\pi)$   $w_t^{(n)} = 0$
  - if $(freq_t^{(n)} > max_f)$ or $(freq_t^{(n)} < min_f)$   $w_t^{(n)} = 0$
  - Normalize particle weights $w_t^{(n)} = w_t^{(n)}/\sum_{n=1}^{N}(w_t^{(n)})$
  - Resample
- end for
```

### 4.6.2 Application

#### 4.6.2.1 Simulated Results

Four frequency and amplitude modulated sine waves which belong to four different frequency bands are generated and WGN is added to sum of the sine waves. The available signal to noise power is measured by SNR in dB unit which is defined as:

$$\text{SNR} = 10log_{10}(\frac{P_{signal}}{P_{noise}}) \tag{4.22}$$

We generated two simulated signals in which the SNR for the first and second signal obtained as 3.0445dB and 7.2167dB respectively. Next, the EMD method is applied to decompose the generated signals into a number of IMFs. In both simulated signals, the second IMF belonged to the frequency range around 20Hz. Since, the resulted IMF was noisy, the proposed method in this section is applied to the IMF in order to track the actual IP of the signal in the frequency range around 20Hz.

We computed the IP, IA, and IF of the actual generated sine wave using HT. Then, we compared the results of tracking the IP, IA, and IF using our method with the results obtained by the HT applied to the noisy IMF. The results are provided in Fig. 4.9 and Fig. 4.10. The mean square error (MSE) of the phase is calculated using the following equation and is shown in Table 4.1 for both SNR levels.

$$\text{MSE} = 1/T \sum_{t=1}^{T} (\theta_{estimate}(t) - \theta_{actual}(t))^2 \tag{4.23}$$

where $T$ is the number of time samples. It can be seen from Fig. 4.10 that around the $10^{th}$ time sample (the corresponding phase in Fig. 4.9 is around 0) the actual frequency decreases, becomes negative, and then it returns to the previous track. However, our method can detect these changes in frequency which is not related to the noise and smooths the frequency such that it does not much affect the phase estimation. Therefore, in this case although we cannot estimate the actual frequency we keep the frequency in a track that will not be lost inside the specified frequency band and it can remove the wide-band noise in other time points as well. In addition, since the estimated frequency does not

Table 4.1: MSE of the phase in two SNR levels.

| | SNR=3.0445dB | SNR=7.2167dB |
|---|---|---|
| Proposed method | 3.7634 | 2.6952 |
| HT of the noisy IMF | 5.7522 | 3.5871 |

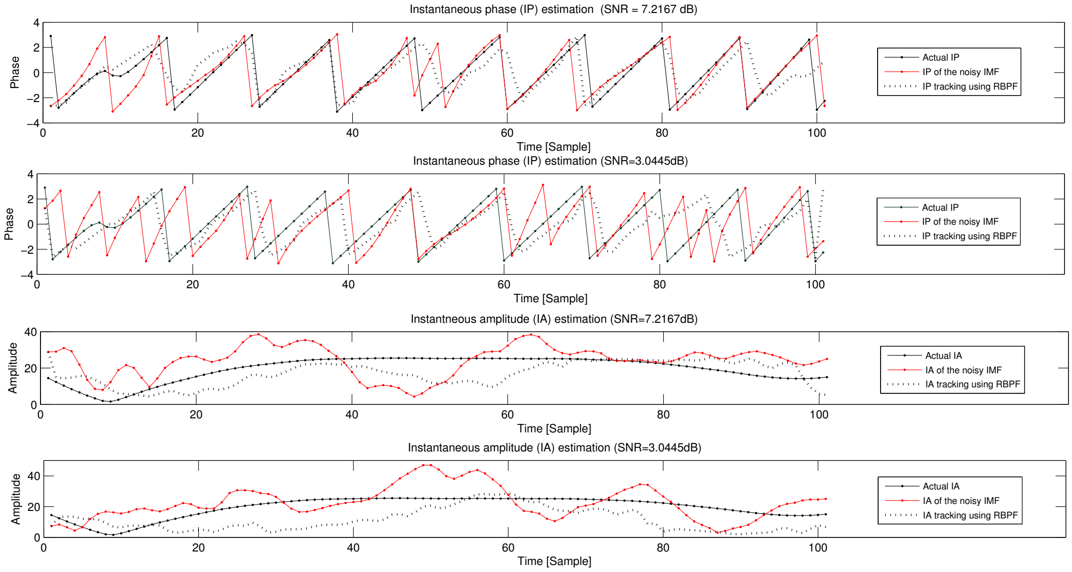

Figure 4.9: IP (top two rows) and IA (bottom two rows) estimation using the proposed and HT methods in two SNR levels.

have direct impact on phase estimation, still the phase estimation around zero is very promising. It can be seen from the figures that when the SNR is lower, the error in estimation is higher. However the overall performance of the method depends also on the operation of EMD.

#### 4.6.2.2 Real Data Results

The real EEG data of a subject in a continuous visual experiment, explained in Section 4.5.2, is used to apply the proposed phase tracking method. Using lowpass interpolation algorithm the sampling frequency was increased to 200Hz. The corresponding algorithm is explained in [95]. We selected the C3 channel and applied the EMD algorithm. The first IMF belonging to beta frequency range was selected and the method applied. The results are provided in Fig. 4.11 and Fig. 4.12.

Therefore, the new proposed phase tracking method uses the IMF given by the EMD algorithm in order to remove the wide-band noise by applying a constrained version of RBPF. As a result, the frequency traces of the IMF become smoother and a better estimation for the IP is achieved. The proposed method is very demanding in order to better estimate the IP of the beta rhythm of the EEG signal, which is usually noisy and contains wide-band noise. The changes in phase synchronization of beta rhythm among different brain regions

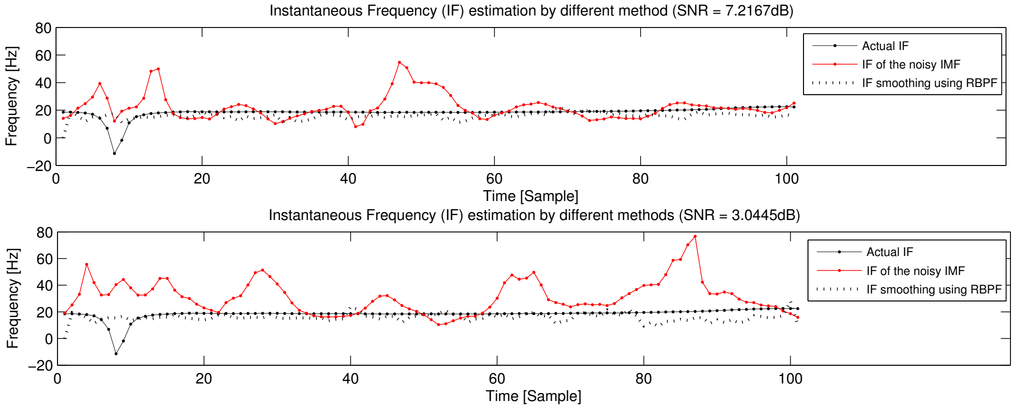

Figure 4.10: IF estimation using the proposed (dotted line) and HT (bold red line) methods in two SNR levels of 7.2dB (top) and 3dB (bottom).

before and during fatigue state, can play an important role in analysis of mental fatigue. Another application of the method is in speech analysis. When the EMD is applied to speech signals, the noise at each time point will be distributed to the IMFs. Therefore, for enhancing several IMFs simultaneously and de-noising the speech signal at each time point, the method should be extended and effectively applied. Further, the method can be developed more in order to solve the mode mixing problem in the EMD algorithm.

## 4.7 Conclusions

In this chapter a new approach for mental fatigue analysis is presented which considers synchronization of brain lobes in different frequency bands. In order to measure the synchronization, the EEG oscillations are extracted from the EMD algorithm. Because often the first few extracted IMFs contain noise, it is suggested to enhance the IMFs by using an ALE. By applying the proposed method to the EEG data of a subject which goes under fatigue, changes in the coherence and phase synchronization of the left and right brain hemispheres in different frequency bands are detected.

In addition, a new method based on RBPF is proposed for IP estimation of an oscillatory waveform. The proposed method can be used for measuring phase synchronization of two oscillations in mental fatigue analysis. However since the method uses RBPF and several constraints and parameters, there is a need for optimal selection of the parameters. Therefore, the method needs to be improved in future for more reliable analysis of mental fatigue based on the changes in the estimated phase synchronization. In the next two chapters, two

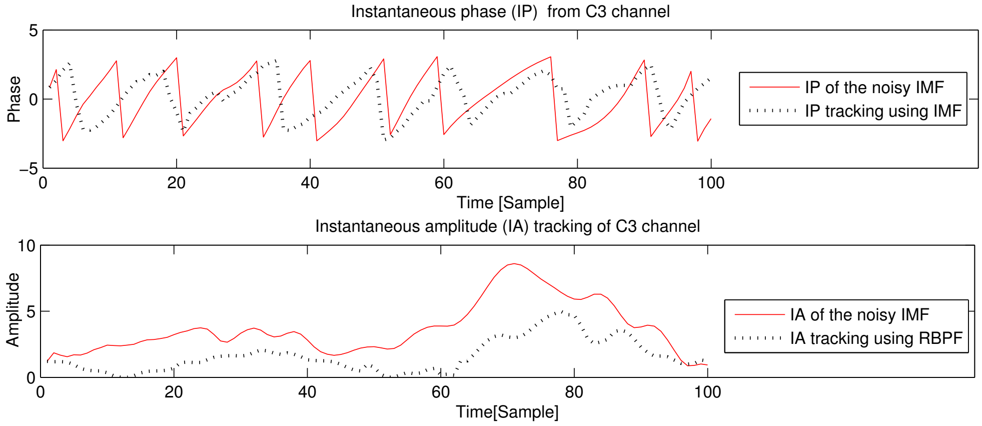

Figure 4.11: IP (tow row) and IA (bottom row) estimation of C3 channel using the proposed method.

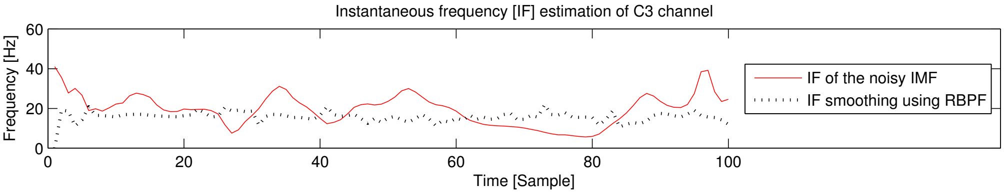

Figure 4.12: IF estimation of C3 channel using the proposed method.

new methods for ERP tracking and detection are proposed. The first method exploits the RBPF and tracks the temporal changes of P300 subcomponents and in the second method a new spatio-temporal filtering method is proposed for estimation of the ERP subcomponents.

# Chapter 5

# Coupled RBPF for Single Trial Estimation of ERPs in Temporal Domain with Application to Mental Fatigue

## 5.1 Introduction

In this chapter a new method for investigating mental fatigue based on P300 variability is presented. Based on this approach a new coupled PF for tracking variability of P300 subcomponents i.e. P3a and P3b, is developed for single trial recordings. Some research has been carried out using BSS and PCA for decomposition of P300 into its subcomponents [69, 75, 76, 77, 78]. In some studies PCA has been applied to the averaged ERP [79, 80, 81]. The PCA method used in these studies is suitable for stationary data disregarding their trial-to-trial variations. The major problem with these methods is that when there is a high temporal correlation between the subcomponents, low signal to noise ratio ERPs, or correlated noise, they may fail to produce correct results. In some cases they are able to estimate only one of the subcomponents. A recent work for single trial estimation of ERP components in [68] formulates wavelet coefficients of the time-locked measured ERPs in the state space and then estimates the ERP components using PF. It is shown that the formulated PF outperforms KF. The method however fails to estimate ERP subcomponents (such as P300 subcomponents). Therefore, a new modelling of ERP subcomponents is demanded.

In this chapter we propose a method based on RBPF [85] to track the dynamic changes of the amplitude, latency, and shape of P300 subcomponents across trials. The proposed method considers the temporal correlation between P300 subcomponents recorded from different sites of the brain and enables separation and identification of the subcomponents. The latency, amplitude, and width of each subcomponent, as the main varying parameters, are modelled using state space systems. In this model the observation is modelled as a linear function of amplitude and a non-linear function of latency and width. Because of uncertainty in the estimation and tracking, two RBPFs are coupled and employed for recursive estimation of the system state across trials. By including some physiological based constraints, the proposed technique prevents generation of invalid particles during estimation of the state.

The main advantage of the algorithm compared with other single trial based methods is its robustness to low signal-to-noise ratios and temporal correlation between the P300 subcomponents. The method is applied to both simulated data and real mental fatigue data to track subtle changes of the P300 subcomponents before and during fatigue state. The results demonstrate potential use of the method in ERP based applications.

Some preliminary results of the method have been presented in [96]. The method presented in this chapter can be considered as an extension of our previous work in [97], in which a constrained PF was employed for separation and tracking the P300 subcomponents from only a single channel.

The designed coupled RBPF (CRBPF) has shown to be helpful and effective in single trial estimation of P300 subcomponents and it can be employed for single trial estimation of any other ERP subcomponents using the corresponding physiological based constraints. The concept of the designed CRBPF is novel and it is expected to be used in some applications where synchronous tracking of states of two dependent systems is required.

The remainder of this chapter is structured as follows. In Section 5.2, a PF formulation is developed for estimation of ERP subcomponents from single trial EEG signals. Then, in Section 5.3, the CRBPF is proposed to track variations of P300 subcomponent across different single trials. In Section 5.4 the method is first applied to simulated data and then it is applied to real mental fatigue data. Finally, Section 5.5 concludes the chapter.

## 5.2 Problem Formulation using PF

In order to track the variations of P3a and P3b parameters within consecutive time-locked trials of stimulated EEGs, PF can be effectively used. Since the aim is to track the latency, amplitude, and width of the ERP subcomponents across trials, the state vector of the PF can be formed as:

$$\mathbf{x}_k = [a_k(1) \quad b_k(1) \quad s_k(1) \quad \ldots \quad a_k(p) \quad b_k(p) \quad s_k(p)]^T \tag{5.1}$$

where $a_k(i)$ is the amplitude, $b_k(i)$ is the latency, and $s_k(i)$ is the width of the $i^{th}$, $i = 1, ..., p$, subcomponent in the $k^{th}$ trial, and $p$ is the number of subcomponents. Based on the above definitions the state transition and observation equations are expressed as:

$$\mathbf{x}_k = \mathbf{x}_{k-1} + \mathbf{n}_{k-1} \tag{5.2}$$

$$\mathbf{z}_k = f(t; \mathbf{x}_k) + \mathbf{v}_k \tag{5.3}$$

where $\mathbf{z}_k$ is the time-locked single trial measurement and

$$f(t; \mathbf{x}_k) = f(t; \mathbf{a}_k, \mathbf{b}_k, \mathbf{s}_k) = \sum_{i=1}^{p} a_k(i) e^{-\frac{(t-b_k(i))^2}{2s_k^2(i)}} \qquad for \quad i = 1, ..., p \tag{5.4}$$

Here $t$ denotes the time index and varies from the beginning of the ERP component to the end of ERP component. The whole time samples in a vector format $[f(1; \mathbf{x}_k) \ldots f(\mathrm{T}; \mathbf{x}_k)]$ are used in the observation equation. Based on this model, each ERP component is modelled as sum of its subcomponents and each subcomponent is approximated by a Gaussian waveform.

In many studies (e.g. see [98, 99]) P300 subcomponents are modelled using parametric functions. Among them Gaussian waveform is the most commonly used type for modelling such subcomponents [82]. Although the actual ERP subcomponents are not necessarily exactly Gaussian waveforms but modelling them as Gaussians leads to a robust and fast estimation of the peak parameters (latency and amplitude). This is what neurophysiologists and cognitive scientists are primarily concerned with.

Using the concept of PF, the available measurements for tracking variability of ERP subcomponents are time-locked single trials. The aim of tracking is to recursively estimate the state of the system which contains the latency, amplitude, and width of each ERP subcomponent.

## 5.3 Coupled RBPF Formulation

The objective here is to incorporate the topographic information of P3a and P3b (locations) into the detection and tracking algorithm which can interlink two trackers corresponding to P3a and P3b to work together. In this section the problem of tracking ERP subcomponents using RBPF from a single channel is formulated first and then the required conditions and measures for coupling two RBPFs, in order to track P300 subcomponents, are described.

It can be seen from equation (5.4) that each ERP component is modelled as sum of several Gaussian waveforms representing its subcomponents. It is possible to factorize the observation model into amplitude information (as the linear part) and exponentially varied waves (as the non-linear part). In this case a linear relation between the observation and the vector of amplitudes has been made while there is generally a non-linear relation with respect to other state variables.

Regarding equations (5.1)–(5.4) and using the concept of RBPF, the state-space and observation can be formulated respectively as:

$$\mathbf{x}_k^1 = [b_k(1) \quad s_k(1) \quad \dots \quad b_k(p) \quad s_k(p)]^T \tag{5.5}$$

$$\mathbf{x}_k^2 = [a_k(1) \quad \dots \quad a_k(p)]^T \tag{5.6}$$

$$\mathbf{z}_k = [f_1(t;\mathbf{x}_k^1) \quad \dots \quad f_p(t;\mathbf{x}_k^1)][a_k(1) \quad \dots \quad a_k(p)]^T + \mathbf{v}_k \tag{5.7}$$

where as in (5.4)

$$f_i(t;\mathbf{x}_k^1) = f_i(t;b_k(i),s_k(i)) = e^{-\frac{(t-b_k(i))^2}{2s_k^2(i)}} \qquad for \quad i = 1, ..., p \tag{5.8}$$

According to the concept of RBPF, the state vector is partitioned into the vectors of linear and non-linear variables. Based on equations (5.5) and (5.6), $\mathbf{x}_k^1$ is the non-linear state vector which contains non-linear variables and $\mathbf{x}_k^2$ is the linear state vector which contains the linear variables. Comparing the above equations with equations (3.20), (3.21) and (3.22), it is evident that $\mathbf{C}_k(\mathbf{x}_k^1)$ (in equation (3.22)) is modelled as the matrix of exponentials $f_i(t;b_k(i),s_k(i))$ which contains the non-linear state variables (latency and width). Also for simplicity $\mathbf{B}_{k-1}(\mathbf{x}_{k-1}^1)$ (in equation (3.21)) is selected as the unitary matrix. In this case the state transition for the linear state variables is independent from the non-linear state variables.

It is possible to apply the RBPF to the single channel of the time-locked measured ERPs in order to track the dynamic changes in latency, amplitude, and width of ERP subcomponents. In the initialization stage, instead of generating random particles, we can use the averaged ERP of several consecutive trials and generate some particles which contribute more to the posterior density. In the subsequent trials, due to the existence of noise and artefact in the data, the correct track of ERP subcomponent parameters may be lost. The use of some physiological constraints on the state variables can be helpful in order to remove the particles which are invalid while they have contribution to the estimation of posterior density. The constraints can be set using the prior knowledge about the ERP subcomponent specifications. In addition, it is possible to apply the tracking procedure to more channels and impose more meaningful constraints. Here, we have designed the CRBPF for tracking the variability of P300 subcomponents from two channels. The subcomponents (P3a and P3b) can be considered spatially disjoint, however they usually overlap temporally on the scalp [22].

As we mentioned in Chapter 2, Section 2.2.1, P3a is located more towards the frontal site while P3b is located more towards the parietal part of the brain. Hence, P3a has larger amplitude over the frontal electrodes and P3b has larger amplitude over the parietal electrodes. In addition, the electrodes on midline are found to be more effective in detection of P300 [22]. We then select Fz electrode in the frontal and Pz electrode in the parietal site. Two RBPFs are formulated. The first one (RBPF1) is applied to the Fz channel while the second one (RBPF2) is applied to the Pz channel. Since the aim is to track the two P300 subcomponents from two channels, for simplicity of notation we rewrite the equations for the state variables of RBPF1 and RBPF2 as follows:

$$\mathbf{x}_k^1 = \boldsymbol{\rho}_k^i = [b_k^i \quad s_k^i \quad \widetilde{b}_k^i \quad \widetilde{s}_k^i]^T \tag{5.9}$$

and

$$\mathbf{x}_k^2 = \mathbf{a}_k^i = [a_k^i \quad \widetilde{a}_k^i]^T \tag{5.10}$$

Therefore, the state equations become:

$$\begin{aligned} \boldsymbol{\rho}_k^i &= \boldsymbol{\rho}_{k-1}^i + \mathbf{w}_{k-1}^{\rho i} \\ \mathbf{a}_k^i &= \mathbf{a}_{k-1}^i + \mathbf{w}_{k-1}^{ai} \end{aligned} \tag{5.11}$$

where $i = 1, 2$ refers to RBPF1 and RBPF2 respectively and $\mathbf{w}_{k-1}^{\rho i}$ and $\mathbf{w}_{k-1}^{ai}$ are zero mean WGN noises with known covariance matrices $\mathbf{Q}_{k-1}^{w(\rho i)}$ and $\mathbf{Q}_{k-1}^{w(ai)}$ respectively. In equation (5.9) $b_k^i$ and $s_k^i$ are respectively the latency and width of P3a in the $k^{th}$ trial of $i^{th}$ RBPF and $\widetilde{b}_k^i$ and $\widetilde{s}_k^i$ are respectively the latency and width of P3b in the $k^{th}$ trial of $i^{th}$ RBPF. In equation (5.10) $a_k^i$ and $\widetilde{a}_k^i$ are the amplitudes of P3a and P3b in the $k^{th}$ trial of $i^{th}$ RBPF.

Tracking two temporally correlated P300 subcomponents from a single channel is not always accurate. Since in the formulation using only one RBPF, sum of two Gaussians and noise is considered, the RBPF tracks the changes of Gaussian parameters across trials. The correct tracking trajectory can be lost because of a sudden change in any one of the parameters of the Gaussians. Therefore, tracking using two channels is expected to be more accurate. By considering the relation between the two RBPFs, it is possible to prevent deviation of the estimation from the actual values. In order to make a connection between the two RBPFs, we assume that the original shapes of P3a and P3b sources are the same at Fz and Pz channels and only the amplitudes can be different. This assumption may not be exactly true in real applications, but it helps to couple the two RBPFs in order to simultaneously track the changes in a system where there is an uncertainty in the signal specifications as a result of very low amplitude of the signal. Therefore, the benefit of simultaneous tracking is to reduce the uncertainty in the system by considering some meaningful constraints.

In addition, we incorporate a small difference in the latencies of P3a and P3b at Fz and Pz channels in our estimation. In the initialization stage, considering the averaged ERP, we generate a rather large number of particles according to the uniform distribution with relatively large variances for the latency, amplitude, and width. These initial particles are the same for RBPF1 and RBPF2. In the subsequent trials, the particles with small weights are replaced by the particles with large weights.

In each trial, the required relation between the two RBPFs should be taken into account for drawing samples from the prior density. As long as we assume that the shapes of P3a or P3b are the same for Fz and Pz channels, we can couple the pairs of particles with the same width for P3a and P3b. The basis of the designed CRBPF is in coupling particle pairs. In Fig. 5.1 one pair of particles has been shown.

Initialization of the particles for RBPF1 and RBPF2 is the same mainly because we want to have particle pairs. In particle pairs the width is the same for P3a in RBPF1 and RBPF2, and also the same for P3b in RBPF1 and RBPF2. Therefore, in each trial it is sufficient to assign the same width for each subcomponent in both RBPFs. However the amplitudes of the subcomponents are different and the latencies differ in small delay. The width and latency values of the subcomponents can be drawn from the prior density. Then, KF can be applied for estimation of amplitudes of the subcomponents.

In this stage, some invalid particles may be generated. It is effective to detect these particles and remove them by setting their weights to zero. Therefore, invalid particles do not have any contribution in the estimation of the system

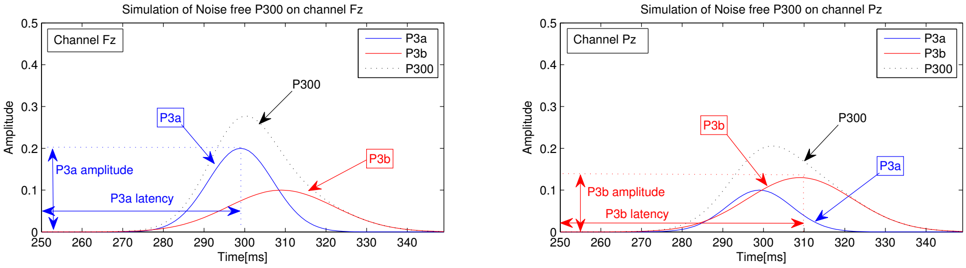

(a) (b)

Figure 5.1: The latency, amplitude, and width of the simulated P3a and P3b at Fz are used as the states of RBPF1 and at Pz as the states of RBPF2. Each particle pair has the same width value for P3a at Fz and Pz channels, and has the same width value for P3b at Fz and Pz channels.

state. One type of invalid particles is the one for which the estimated amplitude of P3a at Pz channel is larger than the amplitude of P3a at Fz channel. Also, the particles for which the estimated amplitude of P3b at Fz channel is larger than the amplitude of P3b at Pz channel are considered invalid.

Usually P3a and P3b overlap over the scalp but P3a has a relatively shorter latency than P3b, therefore, it is possible to have P3a and P3b latencies close to each other. This can cause displacement of generated latencies for P3a and P3b in a particle. The particles in which the latency of P3b is shorter than the latency of P3a are marked invalid. The weight of all the invalid particles are set to zero. The particle weights are then normalized separately. If the weight of one particle is high and the weight of its pair is low or vice versa, we need to decrease the weight of both particle pairs. Because the two RBPFs are working together, an effective particle pair is the one in which both particles have high weights. So, if one of the pairs has a low weight we decrease the weight of both particle pairs.

Therefore, it is possible to update the weights of both particle pairs by incorporating a variable in order to have a better estimation for the width value. Then, for the resampling, we can use a weight that is the scaled weight of both particle pairs. The pseudo-code of the CRBPF is shown in Algorithm 5.1. In this algorithm the optimal values for $\lambda'$ and $\lambda$ can be obtained using some optimization methods. However, we set $\lambda'$ to 1 and $\lambda$ to 0.5 empirically and found them satisfactory in our application based on the simulated data. The important issue is the impact of these variables for better estimation of the weights of particle pairs. $\tau$ is the difference between the latencies of P3a for RBPF1 and RBPF2. In the same way, $\widetilde{\tau}$ is the difference between the latencies of P3b for RBPF1 and

RBPF2. Next, we apply the proposed coupled RBPF to both simulated and real EEG data.

Algorithm 5.1 Pseudo-code for CRBPF

```
set $k = 0$ and generate random numbers $\boldsymbol{\rho}_0^{(n)_1}$,$\boldsymbol{\rho}_0^{(n)_2}$ according to random
uniform distribution considering the averaged ERP.
$n = 1, ..., N_s$, $N_s$ is the number of particles.
$i = 1, 2$ denotes RBPF1 and RBPF2 respectively.
set $\boldsymbol{\mu}_k^{\mathbf{a}(n)_1} = 0$, $\mathbf{P}_k^{\mathbf{a}(n)_1} = \mathbf{I}$, $\boldsymbol{\mu}_k^{\mathbf{a}(n)_2} = 0$ and $\mathbf{P}_k^{\mathbf{a}(n)_2} = \mathbf{I}$
for $\{k = 1$ to $k_{max}\}$ $\{k_{max}$ is the number of trials$\}$
  - generate random numbers $\mathbf{w}_{k-1}^{\rho(n)_1}$ and $\mathbf{w}_{k-1}^{\rho(n)_2}$
  - set $\boldsymbol{\rho}_k^{(n)_1} = \boldsymbol{\rho}_{k-1}^{(n)_1} + \mathbf{w}_{k-1}^{\rho(n)_1}$ and $\boldsymbol{\rho}_k^{(n)_2} = \boldsymbol{\rho}_{k-1}^{(n)_2} + \mathbf{w}_{k-1}^{\rho(n)_2}$ which satisfy the
    following constraints:
    - $s_k^{(n)_1} = s_k^{(n)_2}$ , $\widetilde{s}_k^{(n)_1} = \widetilde{s}_k^{(n)_2}$ , $|b_k^{(n)_1} - b_k^{(n)_2}| \leq \tau$ , $|\widetilde{b}_k^{(n)_1} - \widetilde{b}_k^{(n)_2}| \leq \widetilde{\tau}$
  - update $\boldsymbol{\mu}_k^{\mathbf{a}(n)_1}$, $\boldsymbol{\mu}_k^{\mathbf{a}(n)_2}$, $\mathbf{P}_k^{\mathbf{a}(n)_1}$ and $\mathbf{P}_k^{\mathbf{a}(n)_2}$ for each particle using
    equations (3.24)-(3.28)
  - calculate the weight of each particle using equation (3.18)
  - if $\mu_k^{a(n)_1} < \mu_k^{a(n)_2}$ or $\mu_k^{\widetilde{a}(n)_1} > \mu_k^{\widetilde{a}(n)_2}$ or $b_k^{(n)_1} > \widetilde{b}_k^{(n)_1}$ or $b_k^{(n)_2} > \widetilde{b}_k^{(n)_2}$
    - set $w_k^{(n)_1} = 0$ and $w_k^{(n)_2} = 0$
  - end if
  - normalize the weights $w_k^{(n)_1} = w_k^{(n)_1} / \sum_{n=1}^{N} w_k^{(n)_1}$ and $w_k^{(n)_2} = w_k^{(n)_2} / \sum_{n=1}^{N} w_k^{(n)_2}$
  - set $\alpha^{(n)} = 1 - |w_k^{(n)_1} - w_k^{(n)_2}|$
  - update both weights of RBPF1 and RBPF2
    - set $w_k^{(n)_1} = w_k^{(n)_1} \times \alpha^{(n)} \times \lambda'$
    - set $w_k^{(n)_2} = w_k^{(n)_2} \times \alpha^{(n)} \times \lambda'$
  - Resample particles of RBPF1 and RBPF2 using the scaled weight
    - set $w_k^{(n)} = \lambda \times w_k^{(n)_1} + (1 - \lambda) \times w_k^{(n)_2}$
end for
```

## 5.4 Experimental Results

In this section, first, two sets of simulated signals are generated and the CRBPF is applied to show the capability of the method for tracking the parameters of ERP subcomponents. Then, the method is applied to real mental fatigue data and the corresponding results are provided.

### 5.4.1 Simulated Data

In order to evaluate the method and quantify the detection error the method is applied to some simulated data. In the first set of simulated signals two Gaussian-shape waves representing P3a and P3b are generated. The state variables are latencies, amplitudes, and widths of the Gaussian waves. The uniform distribution is used in order to generate the new state variables from the previous trials. The observations are generated using the corresponding state variables. These state variables share the same width value for the first and second subcomponents. The generated observations satisfy the required constraints for the latency and amplitude of the P300 subcomponents as explained in Section 5.3. This provides a realistic situation for application of the system.

As for real EEG, for the simulated signals the latency of P3a is smaller than the latency of P3b, the amplitude of P3a in the first signal is larger than that of the second signal, and the amplitude of P3b in the second signal is larger than that of the first signal. The noise variance for the latency is 3, for the amplitude is 0.1, and for the width is 1. In each trial the clean observations, which are sum of two Gaussians, are added with a random noise of 0.3 variance. The simulated signals contain 30 trials.

After generating these signals, CRBPF is applied to estimate and track the simulated P300 subcomponents. In Fig. 5.2 the results of tracking of latencies (Fig. 5.2(a,c)), amplitudes (Fig. 5.2(b,d)), and widths (Fig. 5.2(e,f,g,h)) of the generated Gaussians for the first and second RBPF are shown.

Here, the number of particles is set to 10000. If we used PF instead of RBPF, it would be necessary to increase the number of particles. Increasing the number of particles does not necessarily increase the performance of the estimator since there maybe a sudden change in one or more than one of the state variables. By reducing the dimension of the state space and applying RBPF, the same or better performance will be obtained in comparison with PF. In addition, the proposed method involves several constraints which should be checked for each particle. Therefore, the computation time is reduced when RBPF is used.

The rate of invalid particles varied in different trials. In average, 10% of the

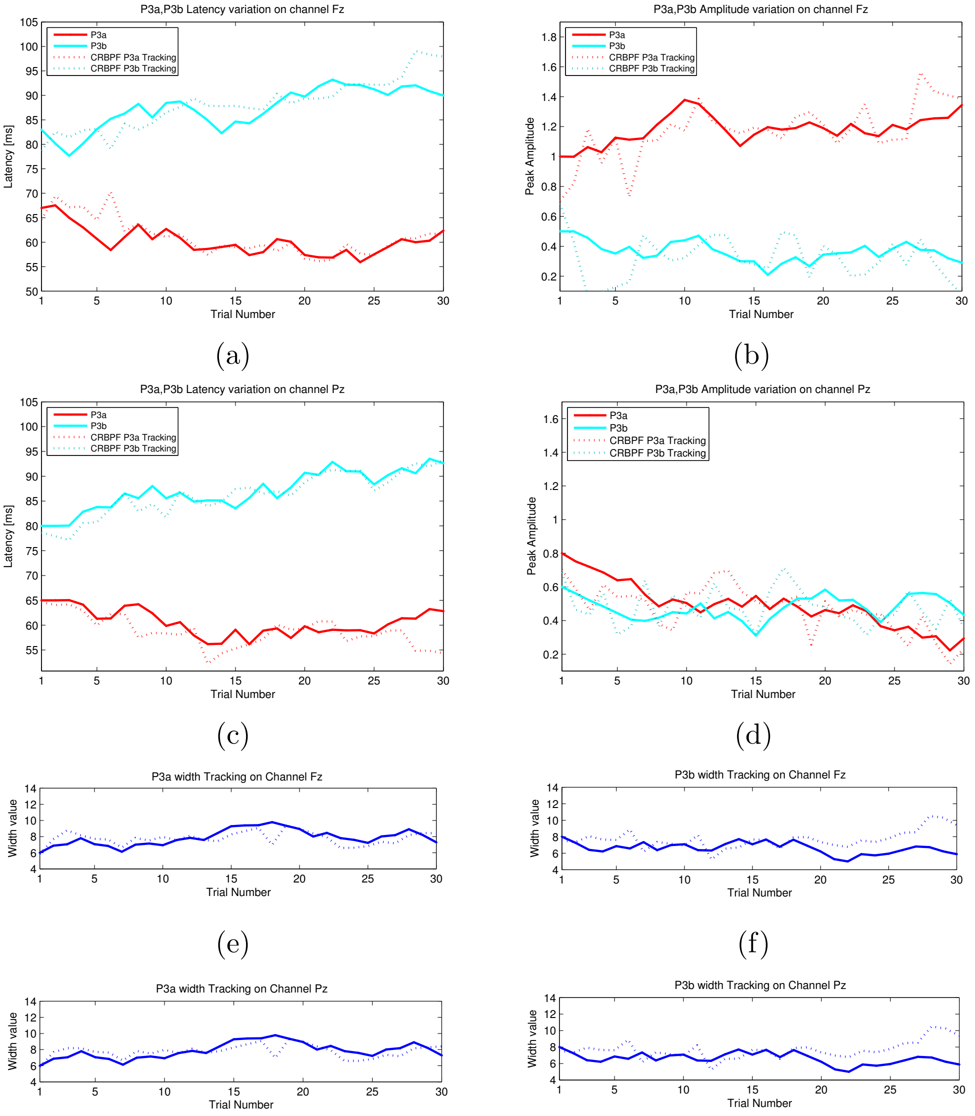

(a) (b)

(c) (d)

(e) (f)

(g) (h)

Figure 5.2: Tracking the latency, amplitude, and width of simulated P3a and P3b on channels Fz (a,b,e,f) and Pz (c,d,g,h) using CRBPF; the thick line connects the actual values while the dotted line is the result of estimation and tracking using CRBPF.

particles marked invalid in each trial. The average computational time for execution of CRBPF in each trial was about 0.7533 of a second (using Pentium(R) 4 CPU 3.00GHz, 3.00 GB of RAM).
The available SNR is measured in dB unit and defined as:

$$\text{SNR} = 10log_{10}(\frac{P_{signal}}{P_{noise}}) \tag{5.12}$$

The MSE is defined as:

$$\text{MSE} = \frac{1}{N}\sum_{i=1}^{N}(z_{act}(i) - z_{est}(i))^2 \tag{5.13}$$

where $z_{act}$ is the original clean observation, $z_{est}$ is the estimated observation, and $N$ is the number of time samples. It can be seen from Fig. 5.2(e,g) that the same width is estimated for P3a at Fz and Pz channels. The same width is also estimated for P3b at Fz and Pz channels (see Fig. 5.2(f,h)). In the first 10 trials, since the filter has not converged, the latency and amplitude estimations, as in Fig. 5.2(a,c,b,d) are not accurate enough. In the subsequent trials the CRBPF converges and has clearly better estimation.

In the last few trials, however, some deviations in the estimation of ERP subcomponent parameters can be seen. This is due to the fact that in each trial, the amplitudes, latencies, and widths, as the states, are generated randomly, and the SNR values are also small. In Fig. 5.3 the calculated MSE and SNR of each trial are shown for Fz and Pz channels in the top and bottom rows. It can be seen from Fig. 5.3(d) that SNR value for the signal in channel Pz is close to 1 and decreases slightly in the later trials. Therefore, in some trials the exact track is lost because of low SNR. Similar to the first trials, however, as the iterations continue, the estimated values are expected to converge to the actual values again.

It can be seen from Fig. 5.3 that the SNR values are moderate in most of realistic situations. On the other hand, the calculated MSE is very low and the tracking is towards the actual values. Although the exact track may be lost in some trials due to the low SNR or sudden change in one of the variables, we still have a very good estimation for the parameters. The important issue is the trend for variations of the parameters which is mostly preserved even after deviation from the actual values. The trend of variations is especially useful when the SNR is negative in which almost all methods fail. However the advantage of tracking across trials is that instead of direct estimation of the parameters, the information from previous trials are taken into account. Therefore, using

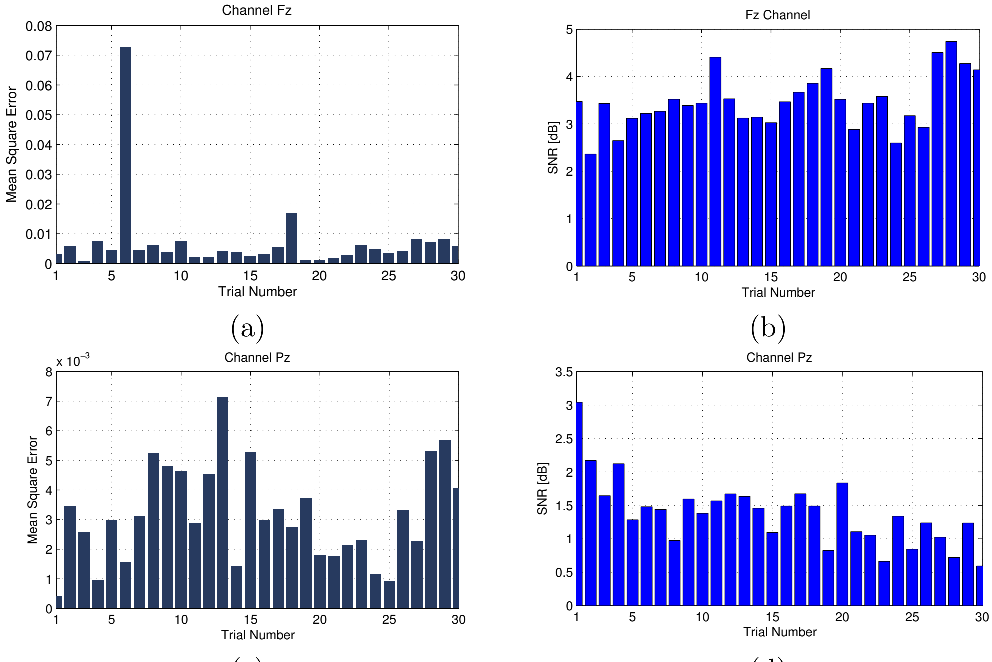

(a) (b)

(c) (d)

Figure 5.3: The corresponding MSE, (a) and (c), and SNR, (b) and (d), calculated in different trials for the simulated data for Fz (top) and Pz (bottom) channels.

a tracking based system such as CRBPF, the trends for variations of the parameters will reveal important information such as increase or decrease of the parameter values across trials. In order to see how the CRBPF works in very low SNRs, in the second simulated signals negative SNRs are also considered.

### Effect of Mismatch

In the first set of simulated signals the generated P3a and P3b were exact Gaussian waveforms. However in the real case P3a and P3b may not be exactly Gaussians. Therefore, in the second set of simulated signals we modelled the P3a and P3b as another waveform to better generalize application of the method. Gamma waveform defined as:

$$r(t) = ct^{k-1}exp(-\frac{t}{\theta}) \tag{5.14}$$

where $k > 0$ is a shape parameter, $\theta > 0$ is a scale parameter, and $c$ is a normalizing constant, is used as an appropriate alternative. The Gamma waves for P3a and P3b are shown in Fig. 5.4. In this figure $k = 3$ and $\theta = 17$ are used for generating both Gamma waves. In this experiment 30 trials are generated. The noise variance for the latency is 3 and for the amplitude is 0.1.

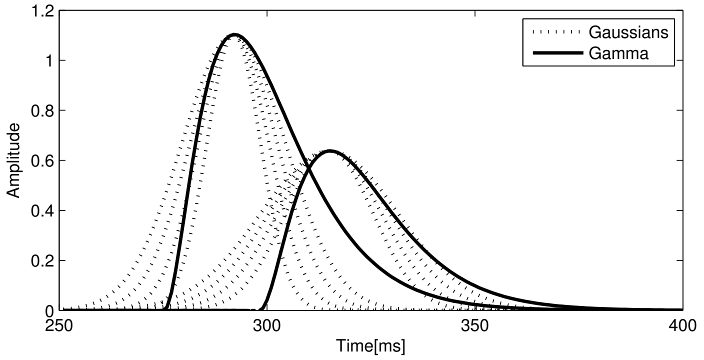

Figure 5.4: Two Gamma waves are used for modelling P3a and P3b. Different Gaussians approximating Gamma waves are also shown.

In each trial, the clean observations which are sum of two Gamma waves as shown in Fig. 5.4 are added with a random noise of variance 0.3. The shape of Gamma waveforms remains the same across all the trials. The aim of this experiment is to verify whether the CRBPF is able to work in the case of having other shapes rather than Gaussians for the original P3a and P3b signals. The experiment is repeated two times and the results of tracking the latency and amplitude variations of P3a and P3b at Fz and Pz channels are shown in Fig. 5.5 and Fig. 5.6. Also, in these figures the MSE and SNR are shown in each trial for each channel.

In Fig. 5.5(a) and Fig. 5.5(e) latency variations of P300 subcomponents (P3a and P3b) at Fz and Pz channels are shown respectively. In the last trials a bias in latency estimation for P3b can be seen. However, from Fig. 5.5(d) and Fig. 5.5(h), it can be seen that the SNR values in the last trials are very low. In Fig. 5.5(b) and Fig. 5.5(f) the amplitude variations for the P300 subcomponents (P3a and P3b) at Fz and Pz channels are shown respectively. From these figures the total variability of the amplitudes are preserved while there are some error in estimation.

In addition, since the estimated P300 signal is based on the Gaussian assumption of the P3a and P3b while the actual P3a and P3b are Gamma waves, it can be seen that the calculated MSE in each trial for Fz and Pz channels shown in Fig. 5.5(c) and Fig. 5.5(g) are high. The estimated width for P3a and P3b had some fluctuations at the initial trials but they remained constant over time. The estimated width corresponds to the width of Gaussian waveform. This however, may not refer to the width of a Gamma wave. The important point is that we kept the width of Gamma waves the same across different trials and the estimated width remained constant after the first few trials. The estimated

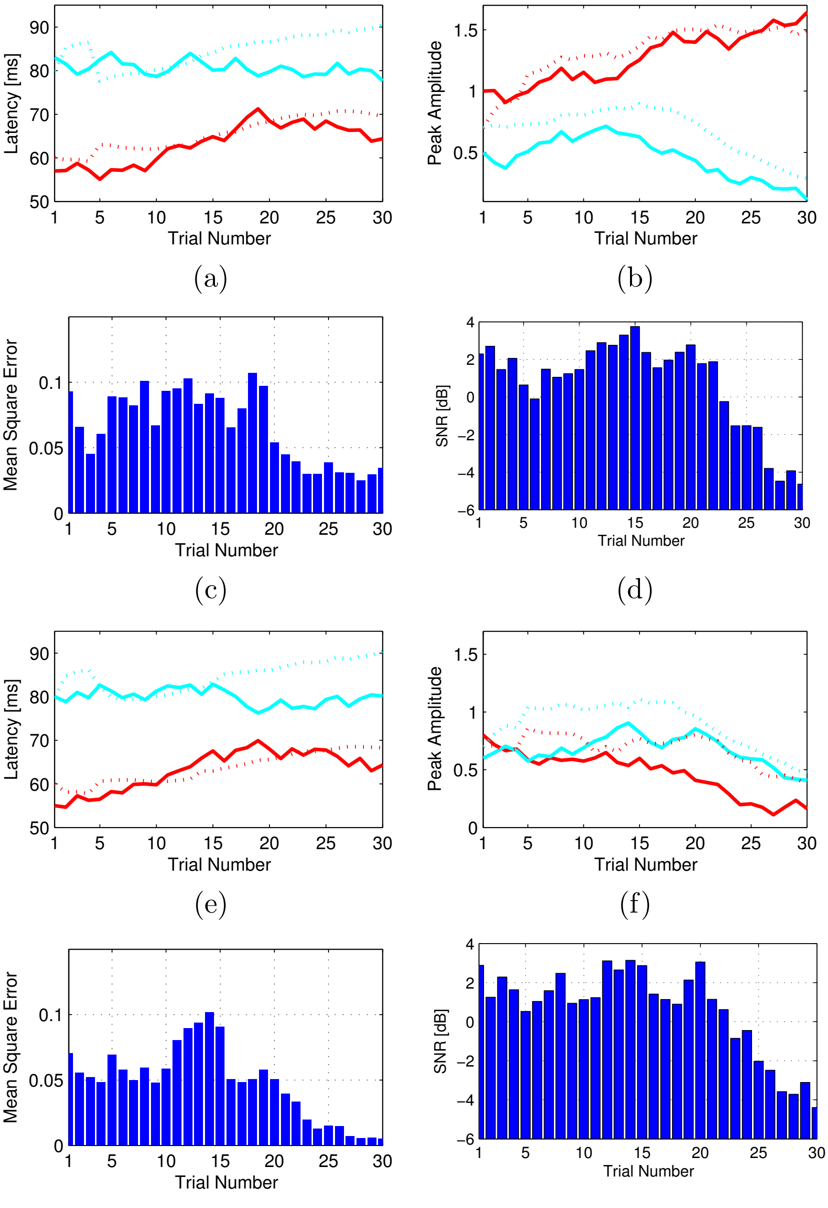

(a) (b)

(c) (d)

(e) (f)

(g) (h)

Figure 5.5: The dotted lines are the results of tracking using CRBPF, (a) latency variations of P3a (red line) and P3b (Blue line) on channel Fz, (b) amplitude variations of P3a (red line) and P3b (Blue line) on channel Fz, (c) MSE obtained at each trial for channel Fz, (d) calculated SNR at each trial for channel Fz, (e) latency variations of P3a (red line) and P3b (Blue line) on channel Pz, (f) amplitude variations of P3a (red line) and P3b (Blue line) on channel Pz, (g) MSE obtained at each trial for channel Pz, and (h) calculated SNR at each trial for channel Pz.

width for each of Gamma-based P3a and P3b relates to the width of a Gaussian that can best approximate them.

Therefore, based on the results of this experiment, in the case of Gamma waveforms for P3a and P3b and despite very low SNRs, the CRPBF can still track inter-trial variabilities of the P3a and P3b parameters with very good approximations. This conclusion has been verified by repetition of the experiment as shown in Fig. 5.6. In this figure the results of tracking P3a and P3b amplitudes and latencies at Fz and Pz channels are shown (Fig. 5.6(a,b,e,f)). The SNR and MSE in each trial for Fz and Pz channels are also shown (Fig. 5.6(c,d,g,h)). In this figure, the SNR value is very low in most of the trials and the actual generated signals for P3a and P3b are Gamma waveforms. The CRBPF nevertheless, is still able to track the inter-trial variabilities of the P3a and P3b.

### 5.4.2 Real Data

The description of the real data is explained in Section 4.5.2. EEG data of one of the subjects was selected. Using interpolation the sampling frequency was increased to 1000Hz in order to increase the temporal resolution. So, for example, a shift of less than 0.01 second in latency can be tracked. Previously, this data set was being used for P300 detection by the averaging method [92].

The CRBPF was applied to Fz and Pz channels considering 50 trials from the first and fourth half an hour. In the first half an hour the subject was not under fatigue while in the fourth half an hour the subject was under fatigue. In both cases, before and during fatigue, the averaged ERP of 20 trials was used to initialize the particles of the CRBPF.

The results of tracking P3a and P3b variability are shown in Fig. 5.7. This figure illustrates the variability of P3a and P3a amplitudes (Fig. 5.7(c,d,g,h)), latencies (Fig. 5.7(a,b,e,f)), and widths (Fig. 5.7(i,j,k,l)) before and during fatigue state. Based on the results it is possible to draw some conclusions about the effect of mental fatigue on P300. Generally in the previous researches on mental fatigue [70, 71, 72, 73, 74], the decrease in the overall P300 amplitude and increase in its latency have been reported. But, using our method we could separate P300 into its constituent subcomponents and evaluate the effect on each subcomponent separately. Based on the results it is concluded that the latencies of both P3a and P3b increase with time on task interval. During the fatigue state the increase of the latency of P3a is slightly more than that for the P3b. Indeed, the amplitude of P3a decreases with fatigue more than that of the P3b. The width of P3b remains approximately constant in the fatigue state while the width of P3a decreases.

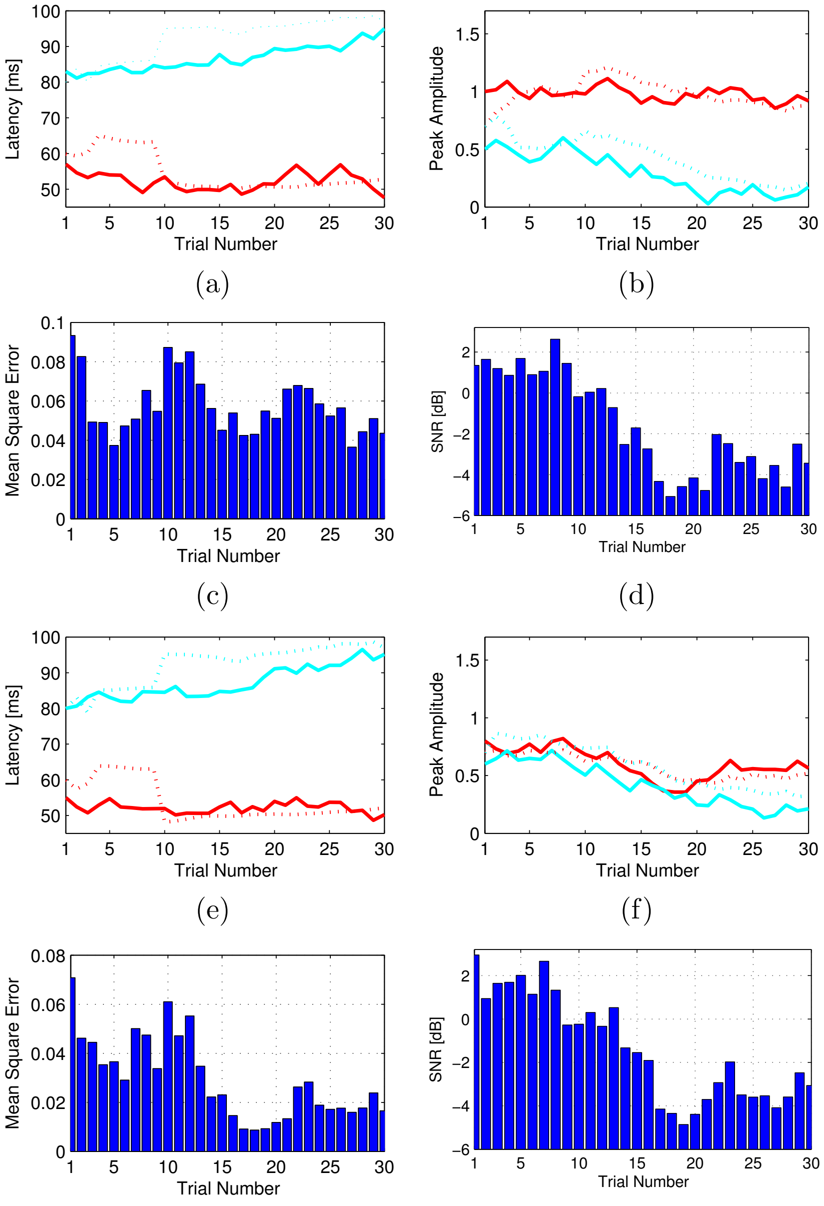

(a) (b)

(c) (d)

(e) (f)

(g) (h)

Figure 5.6: The dotted lines are the results of tracking using CRBPF, (a) latency variations of P3a (red line) and P3b (Blue line) on channel Fz, (b) amplitude variations of P3a (red line) and P3b (Blue line) on channel Fz, (c) MSE obtained at each trial for channel Fz, (d) calculated SNR at each trial for channel Fz, (e) latency variations of P3a (red line) and P3b (Blue line) on channel Pz, (f) amplitude variations of P3a (red line) and P3b (Blue line) on channel Pz, (g) MSE obtained at each trial for channel Pz, and (h) calculated SNR at each trial for channel Pz.

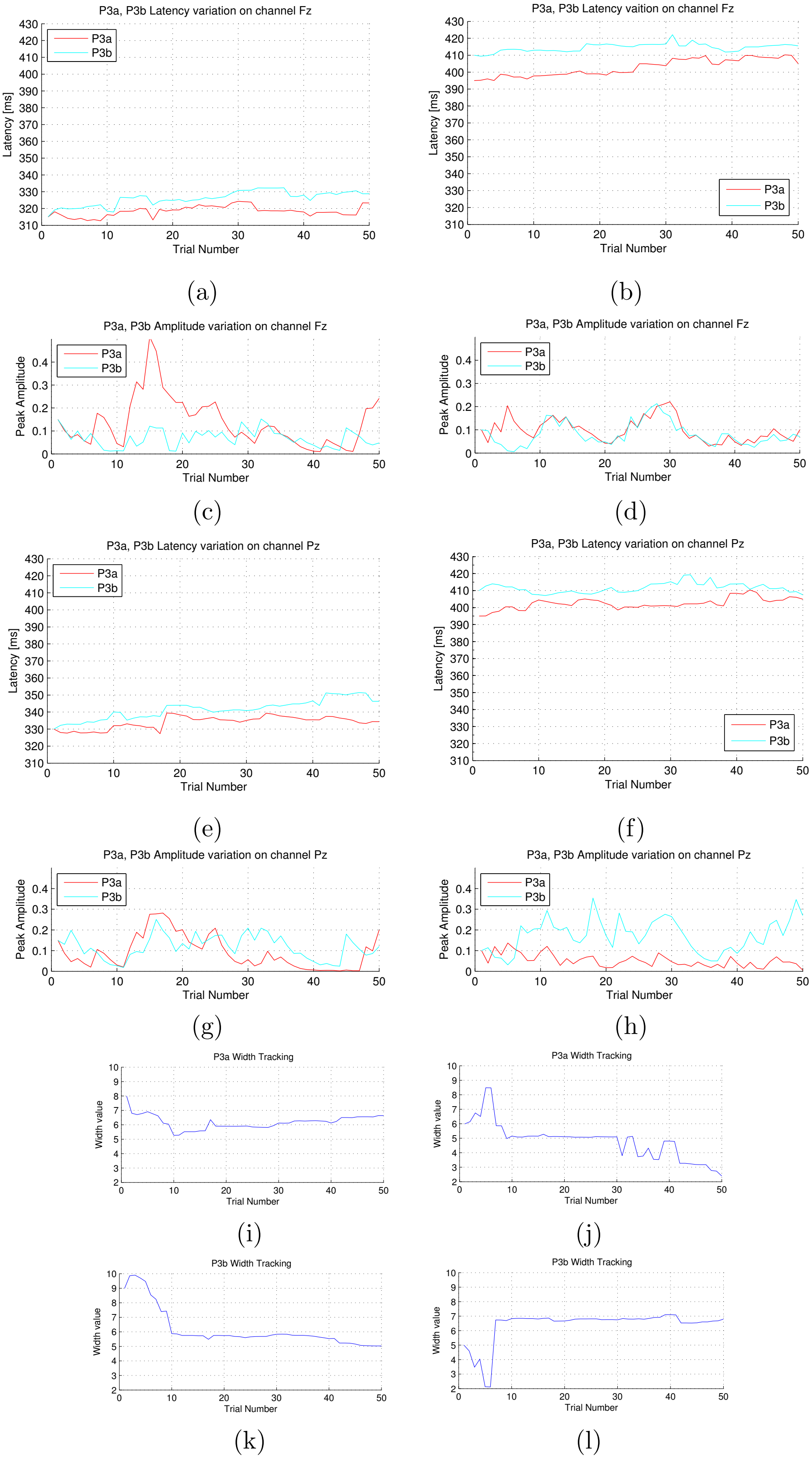

(a) (b) (c) (d) (e) (f) (g) (h) (i) (j) (k) (l)

Figure 5.7: Tracking variability of P3a and P3b before and during fatigue; the left column corresponds to the before fatigue state (a,c,e,g,i,k) while the right column to the during fatigue state (b,d,f,h,j,l).
]

The P3a amplitude seems to become smaller with time on the task, while that of the P3b seems to increase somewhat. During the first half an hour a clear difference between the P3a and P3b locations over scalp is observed. P3a is more prominent at Fz as expected. During the last half an hour the P3a became very small at Pz while the P3b was prominent at this position. P3a is related to novelty. It is possible however that the decrease in the P3a amplitude with time on the task is related to practice on or habituation to the task.

Therefore, mental fatigue can be related to increase in the P3a and P3b latencies, and decrease in the P3a amplitude and width. Using the results of this research the amplitude and width of P3a and latencies of P3a and P3b, obtained by applying CRBPF, can be considered as useful features for detection of fatigue state. However, these features are not enough for distinguishing between the different mental states and alarming the fatigue state. In future studies a comprehensive analysis of mental fatigue can be performed by combination of these extracted features along with other useful features, from different ERP components and subcomponents and the background EEG, and then giving them as an input to a classifier in order to classify different mental states. In addition, it is possible to use all the features obtained by applying the proposed CRBPF in this chapter including latency, amplitude, and width of both P3a and P3b. Then, an appropriate feature selection method can be used to mark and remove the useless features.

## 5.5 Conclusions

In this chapter a new method is proposed to separate and track variability of P300 subcomponents in different single trials. The method has been applied to investigate mental fatigue. The coupled PF proposed in this chapter uses the concept of RBPF, combines two RBPFs, and imposes some constraints on the state variables to have a more reliable estimation and to use the required number of particles effectively. The particle initialization with the help of averaged ERP is useful to move the particles towards the right part of the posterior density. Therefore, the algorithm is capable of estimating P300 component and its subcomponents P3a and P3b in single trials. Here, for the first time, all variations of the P300 subcomponents (P3a and P3b) including latency, amplitude, and width, have been considered from single trials and applied to the mental fatigue. It is known that P3a is an attention related subcomponent and P3b is a memory related subcomponent [22]. Therefore, during the fatigue state the attention to the stimuli decreases more than the memory engagement with the stimuli.

This single trial estimation can reveal important information about the variability of P300 subcomponents which cannot be achieved by detection of averaged P300 as in previous researches whereby the variability of the subcomponents is ignored. Therefore, this new single trial estimation of ERP subcomponents has shown to be favourably effective in mental fatigue analysis. In addition, the designed coupled RBPF is able to synchronously and simultaneously characterize two dependent systems and therefore can be applicable for monitoring many natural systems.

Although the proposed method is based on fitting Gaussians to ERP signals and using application specific constraints, the risk of generating responses that do not exist in the data is avoided by particle initialization using the averaged ERP and especially by coupling the two measurement channels. The coupling is possible since the P3a and P3b are expected to be statistically dependent (e.g. temporal order, correlated amplitudes, etc). Using prior knowledge about other ERP subcomponents, it is possible to use the method with appropriate constraints. In addition, the method can be combined with beamforming algorithms to introduce a spatio-temporal approach for analysis of ERP subcomponents. The results achieved in this work are inline with clinical expectations. They also verify previous reported outcomes by [70, 71, 72, 73, 74]. However, the method has the ability to give more insight about the relative changes of P300 subcomponents. The method presented in this chapter is useful for temporal estimation of ERP subcomponents. In the next chapter, a new single trial estimation method is proposed for spatio-temporal estimation of ERP subcomponents.

# Chapter 6

# Spatio-temporal Filtering Method for Single Trial Estimation of Correlated ERP Subcomponents

## 6.1 Introduction

In the previous chapter a method based on PF was proposed for tracking variability of ERP subcomponents from two channels. The method only considers the temporal variations of the ERP subcomponents across different trials whereas the spatial relationships are ignored. Therefore, a new method for spatio-temporal estimation of ERP subcomponents is demanded.

In this chapter a novel spatio-temporal filtering method is proposed for single trial estimation of ERP subcomponents which can be mutually correlated. The method can be specifically used for spatio-temporal estimation of P300 subcomponents (e.g. P3a and P3b). These subcomponents can be generated in an oddball paradigm considering the target stimuli. It is hypothesized that the discrimination between target and standard stimuli initiates the frontal lobe activity that engages the attention focus demanded by the task performance [100]. P3a is supposed to be related to the neural changes in the anterior cingulate when the incoming stimuli replace the contents of working memory [101]. P3b is then generated from memory storage operations that are initiated in the hippocampal formation in which the update output is transmitted to the parietal cortex [102]. Therefore, the P3a is generated when a demanding stimuli commands frontal lobe attention and subsequently P3b is generated when the required attention resources are allocated for memory updating in association cortex. Based on this model, the P300 component generation is due to the interaction between frontal lobe and hippocampal/temporal-parietal function. Although the exact neural origins of P3a and P3b are distinct, the generation of these subcomponents involve interactions between them and as the result engages overlapping neural activations [100]. Based on this, these subcomponents are correlated. Throughout this study, the correlation of ERPs in temporal or spatial domain is considered as the overlap in time or space domain which can be seen from statistical point of view of the scalp projections and time domain series of the ERPs. However, in general the overlap is the sign of neural generation/interactions of the ERP components/subcomponents.

Recently a method for spatio-temporal estimation of ERP components has been developed [103]. The advantage of this method is that instead of modelling the whole ERP component, it models its descriptors (amplitude and latency) based on the spatial diversity of multi-channel recordings and a user defined template. This method has shown to be effective in ERP component estimation even in negative SNRs. However, although this method can be used for single trial estimation of ERP components, it is not suitable for estimation of the ERP subcomponents particularly when they overlap in time.

Hence, in the case of having correlated components or subcomponents the method cannot achieve correct results. Therefore, in this chapter we have significantly improved the method presented in [103] by developing a spatio-temporal filtering method for single trial estimation of correlated ERP subcomponents. In [82] a spatial notch filter is used to localize the ERP subcomponents in the brain. In this approach the correlation between the desired component and the background EEG has been considered. In our proposed method for spatio-temporal estimation of the ERP subcomponent descriptors two cost functions are defined first. Following that, the latencies, amplitudes, and scalp projections of both subcomponents are estimated. Each cost function can deflate one of the correlated subcomponents and estimate the other one. In general, the subcomponents are considered to be temporally/spatially correlated.

It is possible to generalize the method to be considered for the cases where there are more than two subcomponents. In this chapter in Section 6.2, it is shown mathematically that the method presented in [103] for estimation of the ERP components is not suitable for ERP subcomponent estimation because of temporal correlation between the subcomponents. The new method proposed here however, can result in a very good estimation of ERP subcomponent descriptors.

Therefore, unlike the previous works in ERP estimation [82, 103], the proposed method is able to estimate the subcomponents such as P3a and P3b. The method is applied to both simulated and real data and has shown to perform very well even in low SNRs. The method has been compared with the spatial PCA and its superiority confirmed by using simulated signals. In addition, the two methods were compared in different spatial correlations. Finally it has been compared with temporal PCA for different temporal correlations. The approach can be useful in mental fatigue analysis where the relative variability of P300 subcomponents is the key factor in detecting the level of fatigue.

The remainder of this chapter is structured as follows. In Section 6.2 linear generative EEG model is described. Then, in Section 6.3, the new spatio-temporal filtering method is proposed. In Section 6.4 the results of applying the spatio-temporal filtering to simulated data following by a comparison study are provided. The results of applying the method to the real data are provided in Section 6.5. Finally, Section 6.6 concludes the chapter.

## 6.2 Linear Generative EEG Model

In this section a composite EEG model including two (generally correlated) subcomponents is provided. For this we start with writing the linear generative EEG model in matrix form as:

$$\mathbf{X} = \mathbf{a}\,\mathbf{s} + \sum_{i=1}^{N} \mathbf{b}_i \mathbf{n}_i \tag{6.1}$$

where $\mathbf{X}$ is a $D \times T$ matrix which represents the single trial EEG data of $D$ channels and $T$ samples, $\mathbf{s}$ is a $1 \times T$ vector that can represent the time course of ERP component, $\mathbf{n}_i$ denotes the $1 \times T$ noise in general, and $N$ is the number of noise components. The vectors $\mathbf{a}^T$ and $\mathbf{b}_i^T$ are of dimension $1 \times D$ and can be considered as the projections of the corresponding source and background EEG plus noise to the electrodes respectively, $\mathbf{X}$ can also be modelled in terms of its constituent normalized components as:

$$\mathbf{X} = \sigma_{s0}\mathbf{a}_0\mathbf{s}_0 + \sum_{i=1}^{N} \sigma_i \mathbf{b}_{0i}\mathbf{n}_{0i} \tag{6.2}$$

where $\mathbf{a}_0$, $\mathbf{s}_0$, and $\mathbf{n}_{0i}$ are the normalized versions of their counterparts in (6.1). The scalars $\sigma_{s0}$ and $\sigma_i$ are the overall contributions of the sources to the multi-channel EEG data. It is expected that for a stable normalized scalp projection,

$\mathbf{a}_0$ is fixed for all the trials and the amplitude $\sigma_{s0}$ changes across trials. Now, consider a new equivalent formulation with respect to ERP subcomponents which are potentially correlated (at this stage it is assumed that there are two overlapped subcomponents as the case for P3a and P3b):

$$\mathbf{X} = \sigma_1 \mathbf{a}_1 \mathbf{s}_1 + \sigma_2 \mathbf{a}_2 \mathbf{s}_2 + \sum_{i=1}^{N} \sigma_i \mathbf{b}_{0i} \mathbf{n}_{0i} \tag{6.3}$$

where $\sigma_1$, $\mathbf{a}_1$, and $\mathbf{s}_1$ are the amplitude, scalp projection, and time course of the first ERP subcomponent, and $\sigma_2$, $\mathbf{a}_2$, and $\mathbf{s}_2$ are those of the second ERP subcomponent of the combined component described by $\sigma_{s0}$, $\mathbf{a}_0$, $\mathbf{s}_0$ in equation (6.2). Suppose that we have an estimation of the first subcomponent that is normalized as $\mathbf{y}_1$. If we post-multiply its transpose to both sides of equation (6.3), the following relation will be obtained (the cross term $\mathbf{n}_{0i}.\mathbf{y}_1^T$ nearly vanishes because it is assumed that the noise including the background EEG is uncorrelated with the ERP subcomponents):

$$\mathbf{X}.\mathbf{y}_1^T = \sigma_1 \mathbf{a}_1 \mathbf{s}_1 \mathbf{y}_1^T + \sigma_2 \mathbf{a}_2 \mathbf{s}_2 \mathbf{y}_1^T \tag{6.4}$$

If we assume that the normalized estimated subcomponent $\mathbf{y}_1$ is exactly the same as the first subcomponent, the first term will be equal to $\sigma_1 \mathbf{a}_1$ due to the normalization operation, i.e. $\mathbf{s}_1.\mathbf{y}_1^T$ is equal to 1. The main concern is with the second term in which $\mathbf{s}_2.\mathbf{y}_1^T$ becomes a scaling factor due to the existence of temporal correlation between the subcomponents. If $\mathbf{s}_2.\mathbf{y}_1^T$ were zero (having no temporal correlation), $\mathbf{X}.\mathbf{y}_1^T$ could result in an estimation of $\mathbf{a}_1$. Therefore, multiplication of one of the estimated subcomponents by $\mathbf{X}$ is not useful for estimation of its corresponding scalp projection due to the nonzero nature of the second term in equation (6.4) in the case that the subcomponents are temporally correlated.

The above approach has been proposed and used in [103] in order to have an initial estimation of the scalp projection $\mathbf{a}$ of the ERP component which is uncorrelated with the noise. But we showed that in the case of having temporally correlated ERP subcomponents the method is not able to estimate the scalp projections of the subcomponents. Hence, it is necessary to extend the method to work for estimation of the correlated ERP subcomponents. In the next section, the proposed spatio-temporal filtering method for solving this problem is explained.

## 6.3 Spatio-temporal Filtering Method

The proposed spatio-temporal filtering method for estimation of correlated ERP subcomponents suppresses one subcomponent in spatial domain while detecting the other one in temporal domain. Now, consider the following constrained problem:

$$min \quad ||\mathbf{w}^T\mathbf{X} - \mathbf{r}_1||_2^2 \quad subject\ to \quad \mathbf{w}^T\mathbf{a}_2 = 0 \tag{6.5}$$

where both $\mathbf{w}^T$ and $\mathbf{a}_2^T$ are $1 \times D$ vectors, $\mathbf{r}_1$ is a $1 \times T$ vector, $D$ is the number of channels, and $T$ is the number of time samples. The constrained problem can be converted to an unconstrained problem using Lagrange multipliers leading to the following cost function:

$$\mathbf{F} = ||\mathbf{w}^T\mathbf{X} - \mathbf{r}_1||_2^2 + \mathbf{w}^T\mathbf{a}_2 q \tag{6.6}$$

where $q$ is the Lagrange multiplier. The gradient of $\mathbf{F}$ with respect to $\mathbf{w}^T$ is:

$$\begin{aligned}\frac{\partial F}{\partial \mathbf{w}^T} &= \frac{\partial}{\partial \mathbf{w}^T}\{\mathbf{r}_1\mathbf{r}_1^T - 2\mathbf{r}_1\mathbf{X}^T\mathbf{w} + \mathbf{w}^T\mathbf{X}\mathbf{X}^T\mathbf{w} + \mathbf{w}^T\mathbf{a}_2 q\} \\ &= -2\mathbf{r}_1\mathbf{X}^T + 2\mathbf{w}^T\mathbf{X}\mathbf{X}^T + q\mathbf{a}_2^T\end{aligned} \tag{6.7}$$

By setting the above equation to zero and solving it for $\mathbf{w}^T$:

$$\mathbf{w}^T = 0.5(2\mathbf{r}_1\mathbf{X}^T - q\mathbf{a}_2^T)\mathbf{C}_x^{-1} \tag{6.8}$$

where $\mathbf{C}_x = \mathbf{X}\mathbf{X}^T$. Since we are not sure if $\mathbf{C}_x$ is full rank, we used pseudo-inverse for $\mathbf{C}_x^{-1}$. If (6.8) is substituted into the constraint in (6.5), we obtain:

$$\mathbf{w}^T\mathbf{a}_2 = 0.5(2\mathbf{r}_1\mathbf{X}^T - q\mathbf{a}_2^T)\mathbf{C}_x^{-1}\mathbf{a}_2 = 0; \tag{6.9}$$

This is solved for $q$ which results in:

$$q = \frac{2\mathbf{r}_1\mathbf{X}^T\mathbf{C}_x^{-1}\mathbf{a}_2}{\mathbf{a}_2^T\mathbf{C}_x^{-1}\mathbf{a}_2} \tag{6.10}$$

Now, consider the main cost function in equation (6.5):

$$\mathbf{G} = ||\mathbf{w}^T\mathbf{X} - \mathbf{r}_1||_2^2 \tag{6.11}$$

By setting $\mathbf{G}$ to zero and solving it for $\mathbf{w}$, the optimum solution given by $\mathbf{w}_{opt}^T$ to extract $\mathbf{r}_1$ is given by:

$$\mathbf{w}_{opt}^T = \mathbf{r}_1\mathbf{X}^T\mathbf{C}_x^{-1} \tag{6.12}$$

By pre-multiplying $\mathbf{w}_{opt}^T$ to both sides of equation (6.3), it can be seen that in order to have an estimation of $\mathbf{s}_1$, in the case of having an appropriate reference signal for $\mathbf{s}_1$ i.e. $\mathbf{r}_1$, $\mathbf{w}_{opt}^T\mathbf{a}_1$ will be $1/\sigma_1$ and $\mathbf{w}_{opt}^T\mathbf{a}_2$ will be zero. Therefore, $\mathbf{w}_{opt}^T$ should be orthogonal to $\mathbf{a}_2$. If $\mathbf{a}_1$ and $\mathbf{a}_2$ are orthogonal, then, $\mathbf{w}_{opt}^T$ can be in the direction of $\mathbf{a}_1$ vector. But this does not necessarily mean that $\mathbf{a}_1$ and $\mathbf{a}_2$ should be orthogonal. Some simulations showed that even when $\mathbf{a}_1$ and $\mathbf{a}_2$ are not orthogonal, $\mathbf{w}_{opt}^T$ is found in which $\mathbf{w}_{opt}^T\mathbf{a}_1$ is $1/\sigma_1$ and $\mathbf{w}_{opt}^T\mathbf{a}_2$ is very close to zero.

The only constraint is that $\mathbf{a}_1$ and $\mathbf{a}_2$ should not be exactly in the same direction. This is true for the case of having different ERP subcomponents. This is because the subcomponents originate from distinct regions of the brain and therefore, they are spatially disjoint. The scalp projections can also be described using a forward matrix. This matrix models the mixing process of the sources at the electrodes. When two sources are from different parts of the brain, their forward projection vectors and as the result, their scalp projections are not the same.

Therefore, it is concluded that in the case of having an exact reference for $\mathbf{s}_1$, $\mathbf{w}_{opt}^T\mathbf{a}_1 = 1/\sigma_1$ and $\mathbf{w}_{opt}^T\mathbf{a}_2 = 0$. Substituting $\mathbf{w}_{opt}^T$ from equation (6.12) into $\mathbf{w}_{opt}^T\mathbf{a}_2 = 0$, the following equation will be obtained:

$$\mathbf{r}_1\mathbf{X}^T\mathbf{C}_x^{-1}\mathbf{a}_2 = 0 \tag{6.13}$$

Equation (6.13) is equal to the numerator of equation (6.10) and therefore, the Lagrange multiplier will be zero. This is obvious because this makes the cost functions $\mathbf{F}$ and $\mathbf{G}$ equal. In other words, when it is reasonable to have $\mathbf{w}_{opt}^T\mathbf{a}_2 = 0$ there is no need to add the constraint $\mathbf{w}^T\mathbf{a}_2 = 0$ because as explained, this holds implicitly.

Since it is shown that having $\mathbf{w}^T\mathbf{a}_2 = 0$ as the constraint in (6.5) is not helpful, we define a new constrained problem which is similar to (6.5) but with an alternative constraint. To do that, first $\mathbf{a}_2$ in the constraint term in (6.5) is replaced with $\widetilde{\mathbf{a}}_2$. Later a suitable choice for $\widetilde{\mathbf{a}}_2$ is made and it is shown that solving the new constrained problem leads to the estimation of scalp projection for one of the correlated subcomponents. Therefore, in a similar manner, the new constrained problem is defined as:

$$min \quad ||\mathbf{w}^T\mathbf{X} - \mathbf{r}_1||_2^2 \quad subject\ to \quad \mathbf{w}^T\widetilde{\mathbf{a}}_2 = 0 \tag{6.14}$$

After converting the constrained problem into an unconstrained problem using Lagrange multiplier, the new cost function is obtained as:

$$\widetilde{\mathbf{F}} = ||\mathbf{w}^T\mathbf{X} - \mathbf{r}_1||_2^2 + \mathbf{w}^T\widetilde{\mathbf{a}}_2\widetilde{q} \tag{6.15}$$

Following equations (6.9) and (6.10) the following solution for the Lagrange multiplier is achieved:

$$\widetilde{q} = \frac{2\mathbf{r}_1\mathbf{X}^T\mathbf{C}_x^{-1}\widetilde{\mathbf{a}}_2}{\widetilde{\mathbf{a}}_2^T\mathbf{C}_x^{-1}\widetilde{\mathbf{a}}_2} \tag{6.16}$$

With the help of equations (6.8) and (6.16) $\mathbf{w}^T$ is calculated as follows:

$$\mathbf{w}^T = \mathbf{r}_1\mathbf{X}^T\mathbf{C}_x^{-1} - \frac{\mathbf{r}_1\mathbf{X}^T\mathbf{C}_x^{-1}\widetilde{\mathbf{a}}_2}{\widetilde{\mathbf{a}}_2^T\mathbf{C}_x^{-1}\widetilde{\mathbf{a}}_2}\widetilde{\mathbf{a}}_2^T\mathbf{C}_x^{-1} \tag{6.17}$$

or

$$\mathbf{w} = \mathbf{C}_x^{-1}\mathbf{X}\mathbf{r}_1^T - \frac{\mathbf{r}_1\mathbf{X}^T\mathbf{C}_x^{-1}\widetilde{\mathbf{a}}_2}{\widetilde{\mathbf{a}}_2^T\mathbf{C}_x^{-1}\widetilde{\mathbf{a}}_2}\mathbf{C}_x^{-1}\widetilde{\mathbf{a}}_2 \tag{6.18}$$

We pre-multiply both sides of the above equation by $\mathbf{X}^T$ to obtain the following equation:

$$\mathbf{X}^T\mathbf{w} = \mathbf{X}^T\mathbf{C}_x^{-1}\mathbf{X}\mathbf{r}_1^T - \frac{\mathbf{r}_1\mathbf{X}^T\mathbf{C}_x^{-1}\widetilde{\mathbf{a}}_2}{\widetilde{\mathbf{a}}_2^T\mathbf{C}_x^{-1}\widetilde{\mathbf{a}}_2}\mathbf{X}^T\mathbf{C}_x^{-1}\widetilde{\mathbf{a}}_2 \tag{6.19}$$

A suitable choice is made for $\widetilde{\mathbf{a}}_1$ and $\widetilde{\mathbf{a}}_2$ as:

$$\begin{aligned} \widetilde{\mathbf{a}}_1 &= \mathbf{X}\mathbf{r}_1^T \\ \widetilde{\mathbf{a}}_2 &= \mathbf{X}\mathbf{r}_2^T \end{aligned} \tag{6.20}$$

Therefore, it is simple to derive the following equations using equations (6.3) and (6.20):

$$\begin{aligned} \widetilde{\mathbf{a}}_1 &= \sigma_1\mathbf{a}_1\mathbf{s}_1\mathbf{r}_1^T + \sigma_2\mathbf{a}_2\mathbf{s}_2\mathbf{r}_1^T \\ \widetilde{\mathbf{a}}_2 &= \sigma_1\mathbf{a}_1\mathbf{s}_1\mathbf{r}_2^T + \sigma_2\mathbf{a}_2\mathbf{s}_2\mathbf{r}_2^T \\ \widetilde{\mathbf{a}}_1 &= \sigma_1\mathbf{a}_1\mathbf{s}_1\mathbf{r}_1^T + \frac{(\widetilde{\mathbf{a}}_2 - \sigma_1\mathbf{a}_1\mathbf{s}_1\mathbf{r}_2^T)}{\mathbf{s}_2\mathbf{r}_2^T}\mathbf{s}_2\mathbf{r}_1^T \\ \widetilde{\mathbf{a}}_1 &= \sigma_1\mathbf{a}_1\mathbf{s}_1\mathbf{r}_1^T + \widetilde{\mathbf{a}}_2\frac{\mathbf{s}_2\mathbf{r}_1^T}{\mathbf{s}_2\mathbf{r}_2^T} - \sigma_1\mathbf{a}_1\frac{\mathbf{s}_1\mathbf{r}_2^T(\mathbf{s}_2\mathbf{r}_1^T)}{\mathbf{s}_2\mathbf{r}_2^T} \end{aligned} \tag{6.21}$$

From the above equations, it can be seen that $\widetilde{\mathbf{a}}_1$ and $\widetilde{\mathbf{a}}_2$ are linear combinations of the scaled $\mathbf{a}_1$ and $\mathbf{a}_2$. Having appropriate reference signals, when the correlation between the subcomponents decreases, $\widetilde{\mathbf{a}}_1$ tends towards $\sigma_1\mathbf{a}_1$ and $\widetilde{\mathbf{a}}_2$ tends towards $\sigma_2\mathbf{a}_2$.

In fact, even if by solving equation (6.5) we are able to estimate the scalp projection for one subcomponent, having only the mixture matrix $\mathbf{X}$, we do not have access to $\mathbf{a}_1$ or $\mathbf{a}_2$ (unless there is no correlation between the subcomponents) in order to solve the constrained problem in (6.5). However, by using the reference signals $\mathbf{r}_1$ and $\mathbf{r}_2$, as it is shown in (6.20) and (6.21), we can have access to the linear combinations of the scaled scalp projections of both subcomponents ($\mathbf{a}_1$,$\mathbf{a}_2$). Then, we can use any of the linear combinations and solve the constrained problem in (6.14). In the following equations, we show that having $\widetilde{\mathbf{a}}_2$ as defined in (6.20) by solving the constrained problem in (6.14) the scalp projection for the first subcomponent ($\mathbf{a}_1$) is estimated. The same procedure can be implemented in order to find the scalp projection for the second subcomponent ($\mathbf{a}_2$). By replacing $\widetilde{\mathbf{a}}_1$ from equation (6.21) in equation (6.19), the following equations can be derived:

$$\begin{aligned}
\mathbf{X}^T\mathbf{w} &= \mathbf{X}^T\mathbf{C}_x^{-1}\mathbf{X}\mathbf{r}_1^T - \frac{\widetilde{\mathbf{a}}_1^T\mathbf{C}_x^{-1}\widetilde{\mathbf{a}}_2}{\widetilde{\mathbf{a}}_2^T\mathbf{C}_x^{-1}\widetilde{\mathbf{a}}_2}\mathbf{X}^T\mathbf{C}_x^{-1}\widetilde{\mathbf{a}}_2 \\
&= \mathbf{X}^T\mathbf{C}_x^{-1}\mathbf{X}\mathbf{r}_1^T \\
&- \frac{[\sigma_1\mathbf{s}_1\mathbf{r}_1^T\mathbf{a}_1^T + \frac{\mathbf{s}_2\mathbf{r}_1^T}{\mathbf{s}_2\mathbf{r}_2^T}\widetilde{\mathbf{a}}_2^T - \sigma_1\frac{\mathbf{s}_1\mathbf{r}_2^T(\mathbf{s}_2\mathbf{r}_1^T)}{\mathbf{s}_2\mathbf{r}_2^T}\mathbf{a}_1^T]\mathbf{C}_x^{-1}\widetilde{\mathbf{a}}_2}{\widetilde{\mathbf{a}}_2^T\mathbf{C}_x^{-1}\widetilde{\mathbf{a}}_2}\mathbf{X}^T\mathbf{C}_x^{-1}\widetilde{\mathbf{a}}_2
\end{aligned} \tag{6.22}$$

At this stage it is desired to show that $\mathbf{a}_1^T\mathbf{C}_x^{-1}\widetilde{\mathbf{a}}_2 = 0$. Consider equation (6.13) and use it with swapped indices as:

$$\begin{aligned}
\mathbf{r}_2\mathbf{X}^T\mathbf{C}_x^{-1}\mathbf{a}_1 &= 0 \\
\widetilde{\mathbf{a}}_2^T\mathbf{C}_x^{-1}\mathbf{a}_1 &= 0 \\
\mathbf{a}_1^T\mathbf{C}_x^{-1}\widetilde{\mathbf{a}}_2 &= 0
\end{aligned} \tag{6.23}$$

These can be used to simplify equation (6.22) to:

$$\begin{aligned}
\mathbf{X}^T\mathbf{w} &= \mathbf{X}^T\mathbf{C}_x^{-1}\mathbf{X}\mathbf{r}_1^T - \frac{[\frac{\mathbf{s}_2\mathbf{r}_1^T}{\mathbf{s}_2\mathbf{r}_2^T}\widetilde{\mathbf{a}}_2^T]\mathbf{C}_x^{-1}\widetilde{\mathbf{a}}_2}{\widetilde{\mathbf{a}}_2^T\mathbf{C}_x^{-1}\widetilde{\mathbf{a}}_2}\mathbf{X}^T\mathbf{C}_x^{-1}\widetilde{\mathbf{a}}_2 \\
&= \mathbf{X}^T\mathbf{C}_x^{-1}\mathbf{X}\mathbf{r}_1^T - [\frac{\mathbf{s}_2\mathbf{r}_1^T}{\mathbf{s}_2\mathbf{r}_2^T}]\mathbf{X}^T\mathbf{C}_x^{-1}\widetilde{\mathbf{a}}_2 \\
&= \mathbf{X}^T\mathbf{C}_x^{-1}[\sigma_1\mathbf{a}_1\mathbf{s}_1\mathbf{r}_1^T + \sigma_2\mathbf{a}_2\mathbf{s}_2\mathbf{r}_1^T] \\
&\qquad - \mathbf{X}^T\mathbf{C}_x^{-1}[\frac{\mathbf{s}_2\mathbf{r}_1^T}{\mathbf{s}_2\mathbf{r}_2^T}][\sigma_1\mathbf{a}_1\mathbf{s}_1\mathbf{r}_2^T + \sigma_2\mathbf{a}_2\mathbf{s}_2\mathbf{r}_2^T] \\
&= \mathbf{X}^T\mathbf{C}_x^{-1}[\sigma_1\mathbf{a}_1\mathbf{s}_1\mathbf{r}_1^T + \sigma_2\mathbf{a}_2\mathbf{s}_2\mathbf{r}_1^T] \\
&\qquad - \mathbf{X}^T\mathbf{C}_x^{-1}[\frac{\mathbf{s}_2\mathbf{r}_1^T}{\mathbf{s}_2\mathbf{r}_2^T}\sigma_1\mathbf{a}_1\mathbf{s}_1\mathbf{r}_2^T + \sigma_2\mathbf{a}_2\mathbf{s}_2\mathbf{r}_1^T]
\end{aligned} \tag{6.24}$$

Then, $\mathbf{X}^T\mathbf{w}$ can be simplified more into:

$$\begin{aligned}\mathbf{X}^T\mathbf{w} &= \mathbf{X}^T\mathbf{C}_x^{-1}[\sigma_1\mathbf{a}_1\mathbf{s}_1\mathbf{r}_1^T] - \mathbf{X}^T\mathbf{C}_x^{-1}[\frac{\mathbf{s}_2\mathbf{r}_1^T}{\mathbf{s}_2\mathbf{r}_2^T}\sigma_1\mathbf{a}_1\mathbf{s}_1\mathbf{r}_2^T] \\ &= \mathbf{X}^T\mathbf{C}_x^{-1}\sigma_1\mathbf{a}_1[\mathbf{s}_1\mathbf{r}_1^T - \frac{\mathbf{s}_2\mathbf{r}_1^T}{\mathbf{s}_2\mathbf{r}_2^T}(\mathbf{s}_1\mathbf{r}_2^T)]\end{aligned} \tag{6.25}$$

By pre-multiplying equation (6.25) by $\mathbf{X}$,

$$\mathbf{X}\mathbf{X}^T\mathbf{w} = \mathbf{X}\mathbf{X}^T\mathbf{C}_x^{-1}\sigma_1\mathbf{a}_1[\mathbf{s}_1\mathbf{r}_1^T - \frac{\mathbf{s}_2\mathbf{r}_1^T}{\mathbf{s}_2\mathbf{r}_2^T}(\mathbf{s}_1\mathbf{r}_2^T)] \tag{6.26}$$

Since $\mathbf{C}_x = \mathbf{X}\mathbf{X}^T$ and $\mathbf{X}\mathbf{X}^T\mathbf{C}_x^{-1} = I$, the following equation is derived:

$$\mathbf{X}\mathbf{X}^T\mathbf{w} = \sigma_1\mathbf{a}_1[\mathbf{s}_1\mathbf{r}_1^T - \frac{\mathbf{s}_2\mathbf{r}_1^T}{\mathbf{s}_2\mathbf{r}_2^T}(\mathbf{s}_1\mathbf{r}_2^T)] \tag{6.27}$$

If $\mathbf{X}\mathbf{X}^T\mathbf{w}$ is normalized to unit variance, $\mathbf{a}_1$ will be obtained. Therefore, following (6.20) by using $\widetilde{\mathbf{a}}_2 = \mathbf{X}\mathbf{r}_2^T$, minimizing equation (6.15), solving it for $\mathbf{w}$, and pre-multiplying the resulted $\mathbf{w}$, first by $\mathbf{X}^T$ and then by $\mathbf{X}$, we can have an estimate of $\mathbf{a}_1$. This is the scalp projection of the first subcomponent whose corresponding temporal reference signal is given by $\mathbf{r}_1$.

Therefore, equation (6.15) is shown to be useful in estimation of the scalp projection of one of the correlated subcomponents. Considering equation (6.15) and the results given by equation (6.27), the procedure for estimating the scalp projection of the first subcomponent is illustrated in Algorithm 6.1.

Algorithm 6.1: ESP1 Estimation of the scalp projection for the first subcomponent

```
$\mathbf{a}_1$ = ESP1 (X,$\mathbf{r}_1$,$\mathbf{r}_2$)
-Set $\mathbf{C}_x^{-1} = (\mathbf{X}\mathbf{X}^T)^{-1}$
-Set $\widetilde{\mathbf{a}}_2 = \mathbf{X}\mathbf{r}_2^T$ (see eq. 6.20)
-Find $\widetilde{q} = 2(\mathbf{r}_1\mathbf{X}^T\mathbf{C}_x^{-1}\widetilde{\mathbf{a}}_2)/(\widetilde{\mathbf{a}}_2^T\mathbf{C}_x^{-1}\widetilde{\mathbf{a}}_2)$ (see eq. 6.16)
-Find $\mathbf{w} = \mathbf{C}_x^{-1}\mathbf{X}\mathbf{r}_1^T - 0.5\widetilde{q}\mathbf{C}_x^{-1}\widetilde{\mathbf{a}}_2$ (see eq. 6.18)
-Estimate $\mathbf{a}_1 = (\mathbf{X}\mathbf{X}^T\mathbf{w})/norm(\mathbf{X}\mathbf{X}^T\mathbf{w})$ see (eq. 6.27)
Return $\mathbf{a}_1$
```

Similarly, to enable estimation of the scalp projection for the second subcomponent, equation (6.15) can be replaced by the following equation:

$$\widetilde{\mathbf{F}} = ||\mathbf{w}^T\mathbf{X} - \mathbf{r}_2||_2^2 + \mathbf{w}^T\widetilde{\mathbf{a}}_1\widetilde{q} \tag{6.28}$$

Using the above equation, the same procedure can be followed in order to find the scalp projection of the second subcomponent. The Pseudo-code for estimating the scalp projection of the second subcomponent is illustrated in Algorithm 6.2.

Algorithm 6.2: ESP2 Estimation of the scalp projection for the second subcomponent

```
$\mathbf{a}_2 = \mathrm{ESP2}\ (\mathrm{X}, \mathbf{r}_1, \mathbf{r}_2)$
-Set $\mathbf{C}_x^{-1} = (\mathbf{X}\mathbf{X}^T)^{-1}$
-Set $\widetilde{\mathbf{a}}_1 = \mathbf{X}\mathbf{r}_1^T$
-Find $\widetilde{q} = 2(\mathbf{r}_2\mathbf{X}^T\mathbf{C}_x^{-1}\widetilde{\mathbf{a}}_1)/(\widetilde{\mathbf{a}}_1^T\mathbf{C}_x^{-1}\widetilde{\mathbf{a}}_1)$
-Find $\mathbf{w} = \mathbf{C}_x^{-1}\mathbf{X}\mathbf{r}_2^T - 0.5\widetilde{q}\mathbf{C}_x^{-1}\widetilde{\mathbf{a}}_1$
-Estimate $\mathbf{a}_2 = (\mathbf{X}\mathbf{X}^T\mathbf{w})/norm(\mathbf{X}\mathbf{X}^T\mathbf{w})$
Return $\mathbf{a}_2$
```

Incorporating and estimating the spatial projecting vectors $\widetilde{\mathbf{a}}_1$ and $\widetilde{\mathbf{a}}_2$ into the temporal least square (6.15) and estimation of $\mathbf{w}^T$ significantly improve the results and enable separation of temporally or spatially correlated signals such as P3a and P3b. One achievement which has also been confirmed by simulation is that in the case of a mismatch between the reference signal and the actual source the normalized vector of $\mathbf{X}\mathbf{X}^T\mathbf{w}$ does not change (or because of different noise level it changes very slightly). In other words, the estimation of scalp projection of one of the ERP subcomponents is not exactly dependent on the shape of the reference signals. These references, although reasonably similar to the source signals, are not their exact replications. When there is a mismatch between the actual source and the reference signal, we can still have a very good approximation of scalp projections of the subcomponents. This is due to the fact that the mismatch results in the change of the scale $([\mathbf{s}_1\mathbf{r}_1^T - \frac{\mathbf{s}_2\mathbf{r}_1^T}{\mathbf{s}_2\mathbf{r}_2^T}(\mathbf{s}_1\mathbf{r}_2^T)])$ in equation (6.27) in the estimation. After normalization however, this has no effect in estimation of the scalp projection.

In other words, the scale contains the dot product of the actual sources and the reference signals. If the reference is not exactly the same as the source signal, we have a different scale; however after normalization, the scale will not influence estimation of the scalp projections. If both reference signals are uncorrelated (or slightly correlated) with the source the vector $\mathbf{X}\mathbf{X}^T\mathbf{w}$ tends to zero vector. Therefore, we are able to check whether we are dealing with correct references (or dealing with meaningful ranges of latencies for given references).

Nevertheless, in order to have a temporal estimation for each subcomponent, we need to solve equation (6.11) to find $\mathbf{w}_{opt}^T$ given in (6.12) and then pre-multiply it by $\mathbf{X}$. Therefore, given a reference signal for each subcomponent, $\mathbf{w}_{opt}^T\mathbf{X}$ will be the temporal estimation of that subcomponent.

As stated in Chapter 5, Section 5.2, ERP subcomponents are modelled using parametric functions in many studies (e.g. see [98, 99]). The macroscopic EEG electrical field is created from spike trains by a non-linear generator with a second-order linear component with real poles as noted by Freeman [104]. According to this model, the impulse response of the system is a monophasic waveform with a single mode, where the rising time depends on the relative magnitude of the two real poles and can therefore vary compared to the falling time. This means Gamma functions can best represent the brain activations.

Therefore, like the method in [103] we used Gamma wave as an approximation to ERP subcomponents. Based on the defined algorithm, first, we generate two references $(\mathbf{r}_1, \mathbf{r}_2)$ which represent the first and second subcomponents using Gamma functions expressed as:

$$r(t) = ct^{k-1} exp(-\frac{t}{\theta}) \tag{6.29}$$

where $k > 0$ is a shape parameter, $\theta > 0$ is a scale parameter, and $c$ is a normalizing constant. The Gamma function can be considered as a monophasic waveform with its mode at $t = (k-1)\theta, (k > 1)$. The Gamma wave has a short rise time and a longer tail for small $k$, and for the large $k$ it is a symmetric waveform. The Pseudo-code for the new spatio-temporal filtering method is shown in Algorithm 6.3. This algorithm uses the procedures in EPS1 and EPS2 algorithms. Gamma waves are used for generating the reference signals. Also in this algorithm several cost functions are defined in order to have reliable estimations for the subcomponent parameters.

After generating Gamma wave as a reference signal for each ERP subcomponent, we slide each reference in a range of valid latencies to generate more reference signals for both subcomponents. We represent the peak latency of the reference as $\tau$. Having generated references, the value of $\widetilde{\mathbf{a}}_1$ and $\widetilde{\mathbf{a}}_2$ can be obtained using equation (6.20). Then, it is possible to solve the unconstrained problems given in (6.15) and (6.28) considering each reference and $\widetilde{\mathbf{a}}_i$ ($i$=1,2) that is obtained by using the reference for another subcomponent. Next, we estimate $\mathbf{w}_1(\tau_1)$ and $\mathbf{w}_2(\tau_2)$ using equation (6.18) as shown in EPS1 and EPS2 Algorithms.

Then, considering three cost functions ($J_1(\tau_1)$, $J_2(\tau_2)$, and $\widetilde{J}(\tau_1, \tau_2)$), we choose the reference signals for which the sum of the three cost functions is minimum. Finally, we are able to estimate $\mathbf{a}_1$, $\mathbf{a}_2$, $\sigma_1$, and $\sigma_2$. Practically, better results are achieved in estimation of peak latency if we use $\widetilde{J}(\tau_1, \tau_2)$ cost function. This cost function is obtained from equations (6.11) and (6.12) by considering sum of the reference signals and also each reference signal separately. This is not surprising since for temporal estimation of the subcomponents it is preferred to use $\mathbf{w}_{opt}$ given in equation (6.12) and for the estimation of scalp projection and the amplitude it is better to use the constrained problem given in (6.14). Therefore, for estimation of the peak latency we use $\mathbf{w}_{opt}$ resulted when using the reference signals for each subcomponent and considering $\widetilde{J}(\tau_1, \tau_2)$ cost function.

Algorithm 6.3 New spatio-temporal filtering method

```
-Generate $\mathbf{r}_1(\tau_1)$,$\mathbf{r}_2(\tau_2)$ considering reasonable ranges of peak
latencies $[\tau_1 \in \mathbf{T}_{s1}, \tau_2 \in \mathbf{T}_{s2}]$ for the first and second
subcomponents using Gamma waves
-Set $\widetilde{\mathbf{a}}_1(\tau_1) = \mathbf{X}\mathbf{r}_1(\tau_1)^T$ and $\widetilde{\mathbf{a}}_2(\tau_2) = \mathbf{X}\mathbf{r}_2(\tau_2)^T$
-Find $\mathbf{w}_1(\tau_1) = \mathbf{C}_x^{-1}\mathbf{X}\mathbf{r}_1(\tau_1)^T - \frac{\mathbf{r}_1(\tau_1)\mathbf{X}^T\mathbf{C}_x^{-1}\widetilde{\mathbf{a}}_2(\tau_2)}{\widetilde{\mathbf{a}}_2^T(\tau_2)\mathbf{C}_x^{-1}\widetilde{\mathbf{a}}_2(\tau_2)}\mathbf{C}_x^{-1}\widetilde{\mathbf{a}}_2(\tau_2)$
      $\mathbf{w}_2(\tau_2) = \mathbf{C}_x^{-1}\mathbf{X}\mathbf{r}_2(\tau_2)^T - \frac{\mathbf{r}_2(\tau_2)\mathbf{X}^T\mathbf{C}_x^{-1}\widetilde{\mathbf{a}}_1(\tau_1)}{\widetilde{\mathbf{a}}_1^T(\tau_1)\mathbf{C}_x^{-1}\widetilde{\mathbf{a}}_1(\tau_1)}\mathbf{C}_x^{-1}\widetilde{\mathbf{a}}_1(\tau_1)$
-Set $J_1(\tau_1) = ||\mathbf{w}_1^T(\tau_1)\mathbf{X} - \mathbf{r}_\mathbf{1}(\tau_1)||_2^2 + \mathbf{w}_1(\tau_1)^T\widetilde{\mathbf{a}}_2(\tau_2)\widetilde{q}$
      $J_\mathbf{2}(\tau_\mathbf{2}) = ||\mathbf{w}_2^T(\tau_2)\mathbf{X} - \mathbf{r}_2(\tau_2)||_2^2 + \mathbf{w}_2(\tau_2)^T\widetilde{\mathbf{a}}_1(\tau_1)\widehat{q}$
      $\widetilde{J}(\tau_1, \tau_2) = ||(\mathbf{r}(\tau_1) + \mathbf{r}(\tau_2))[\mathbf{X}^T\mathbf{C}_x^{-1}\mathbf{X} - I]||_2^2 +$
      $||\mathbf{r}(\tau_1)[\mathbf{X}^T\mathbf{C}_x^{-1}\mathbf{X} - I]||_2^2 + ||\mathbf{r}(\tau_2)[\mathbf{X}^T\mathbf{C}_x^{-1}\mathbf{X} - I]||_2^2$
      $[\mathbf{l}_1, \mathbf{l}_2] = \underset{\tau_1,\tau_2}{argmin}\ (J_1(\tau_1) + J_2(\tau_2) + \widetilde{J}(\tau_1, \tau_2))$
-Estimate $\mathbf{a}_1 = \frac{\mathbf{X}\mathbf{X}^T\mathbf{w}_1(\mathbf{l}_1)}{norm(\mathbf{X}\mathbf{X}^T\mathbf{w}_1(\mathbf{l}_1))}$
      $\mathbf{a}_2 = \frac{\mathbf{X}\mathbf{X}^T\mathbf{w}_2(\mathbf{l}_2)}{norm(\mathbf{X}\mathbf{X}^T\mathbf{w}_2(\mathbf{l}_2))}$
      $\sigma_1 = 1/[(\mathbf{r}_1(\mathbf{l}_1)\mathbf{X}^T\mathbf{C}_x^{-1})(\mathbf{a}_1)]$
      $\sigma_2 = 1/[(\mathbf{r}_2(\mathbf{l}_2)\mathbf{X}^T\mathbf{C}_x^{-1})(\mathbf{a}_2)]$
-Find the peak latencies as $[\widetilde{\tau}_1, \widetilde{\tau}_2] = \underset{\tau_1,\tau_2}{argmin}\ \widetilde{J}(\tau_1, \tau_2)$
```

## 6.4 Simulation Results

In this section, the method is applied to simulated data and the corresponding results are demonstrated. The goal of the simulation study is to evaluate the ability of the method in estimation of peak latency, amplitude, and scalp projection of the ERP subcomponents in single trials in different SNR levels. In addition, the performance of the proposed method and the PCA method have been compared. In the following, the PCA, spatial PCA, and temporal PCA methods are briefly described. Then, a comparison study including the simulation results is provided.

### 6.4.1 PCA, Temporal PCA, Spatial PCA, and Spatio-temporal PCA

Statistical decomposition of ERPs has been of great interest among ERP researchers over the past several decades. A variety of methods have been proposed in which PCA [105, 106, 107] has been the simplest and most widely used method. PCA uses eigenvalue decomposition to extract linear combinations of variables from a data covariance matrix. Therefore, PCA can be performed by eigenvalue decomposition of a data covariance matrix or by singular value decomposition (SVD) of a data matrix. In SVD decomposition the data matrix is usually mean centered for each variable.

The target outputs of a PCA algorithm are the component scores and loadings. The component scores are the transformed variable values corresponding to a particular case in the data while the component loadings are the variance each original variable would have if the data were projected onto a given PCA axis. Mathematically, PCA can be considered as an orthogonal linear transformation that transforms the data to a new coordinate system. In the new coordinate system, the greatest variance by any projection of the data comes to lie on the first coordinate in which is called the first principal component. Then, the second greatest variance lie on the second coordinate as the second principal component, and so on [106]. Suppose the data matrix $\mathbf{X}^T$ is available; this data matrix contains $n$ rows, which represent $n$ observations, and $m$ columns which represent $m$ features. The SVD of $\mathbf{X}$ is given by:

$$\mathbf{X} = \mathbf{B}\boldsymbol{\Sigma}\mathbf{V}^T \tag{6.30}$$

where $\mathbf{B}$ is the $m \times m$ matrix of the eigenvectors of $\mathbf{X}\mathbf{X}^T$, $\boldsymbol{\Sigma}$ is the $m \times n$ rectangular diagonal matrix with nonnegative real numbers on the diagonal, and matrix $\mathbf{V}$ is $n \times n$. When the same number of principal components as original variables are obtained, then PCA has preserved the dimensionality as:

$$\begin{aligned} \mathbf{Y}^T &= \mathbf{X}^T\mathbf{B} \\ &= \mathbf{V}\boldsymbol{\Sigma}^T \end{aligned} \tag{6.31}$$

In the cases where $m < n - 1$, $\mathbf{V}$ is not uniquely defined whereas $\mathbf{Y}$ is uniquely defined. Each row of $\mathbf{Y}^T$ is a rotation of the corresponding row of $\mathbf{X}^T$. This is due to the fact that by definition of the SVD of a real matrix, $\mathbf{B}$ is an orthogonal matrix. The first column of $\mathbf{Y}^T$ consists of the scores with respect to the first principal component, while the second column has the scores with respect to the second principal component, and so on.

In a reduced-dimensionality representation, the data matrix $\mathbf{X}$ is projected down into the reduced space defined by only the first $L$ singular vector:

$$\begin{aligned}\mathbf{Y} &= \mathbf{B}_L^T\mathbf{X} \\ &= \boldsymbol{\Sigma}_L\mathbf{V}_L^T\end{aligned} \tag{6.32}$$

Matrix $\mathbf{B}$ of eigenvectors of the observation covariances $\mathbf{C} = \mathbf{X}\mathbf{X}^T$ matrix is equivalent to matrix $\mathbf{B}$ of singular vectors of $\mathbf{X}$:

$$\mathbf{X}\mathbf{X}^T = \mathbf{B}\boldsymbol{\Sigma}\boldsymbol{\Sigma}^T\mathbf{B}^T \tag{6.33}$$

If we consider a set of points in Euclidean space, the first extracted principal component corresponds to a line that minimizes the square sum of the distances of the points from the line. This line should pass through the multidimensional mean. In a similar manner, the second extracted principal component corresponds to a line that has the minimum square sum of the distances of the points from that line. Before extracting the second principal component, all the correlation with the first principal component should be subtracted out from the points. The singular values in $\boldsymbol{\Sigma}$ are the square roots of the eigenvalues of matrix $\mathbf{X}\mathbf{X}^T$.

Each eigenvalue is proportional to the portion of the variance (square sum of distances of the points from their multidimensional mean) that corresponds to each eigenvector. Therefore, the sum of all the eigenvalues is equal to the square sum of the distances of the points from their multidimensional mean. PCA algorithm rotates the set of points around their mean in order to find the principal components. Using an orthogonal transformation, the most variance is moved into the first few dimensions. The other components which have small variances can be removed without loss of information. The mean centering (mean subtraction) of the data before applying PCA is necessary to ensure that the first principal component represents the direction of maximum variance. If mean subtraction is not performed, it is possible that the first principal component is similar to the mean of the data. The first principal component is obtained as:

$$\mathbf{b}_1 = \underset{\|\mathbf{b}\|=1}{argmax} \text{ Var } \mathbf{b}^T\mathbf{X} = \underset{\|\mathbf{b}\|=1}{argmax} \ \mathbf{E}\{(\mathbf{b}^T\mathbf{X})^2\} \tag{6.34}$$

Having the first $k-1$ extracted principal components, the $k^{th}$ principal component can be obtained by subtracting the first $k-1$ principal components from the data matrix $\mathbf{X}$:

$$\hat{\mathbf{X}}_{k-1} = \mathbf{X} - \sum_{i=1}^{k-1} \mathbf{b}_i \mathbf{b}_i^T \mathbf{X} \tag{6.35}$$

By considering $\hat{\mathbf{X}}_{k-1}$ as the new data matrix, the next principal component will be obtained as:

$$\mathbf{b}_k = \underset{\|\mathbf{b}\|=1}{argmax} \ \mathbf{E}\{(\mathbf{b}^T\hat{\mathbf{X}}_{k-1})^2\} \tag{6.36}$$

In ERP analysis, PCA has been used mainly for separation of the ERP components/subcomponents from the background EEG [108, 109]. However, other applications of PCA can be in data reduction or filtering. This is because PCA can be used to simplify the analysis of complex data by compressing the important information into small number of components.

### Factor rotation

PCA is applied to the ERP data in two steps. The first step is principal component extraction as explained above. From now on, for simplicity the principal components are referred to as the factors. This initial extraction results in an un-rotated solution [108]. The output of the first step is a factor loading matrix and a factor score matrix. The factor loading matrix relates to the correlations between the variables and the factor scores while the factor score matrix represents the magnitude of the factors for each of the observations. Therefore, the factor score matrix represents the relationship between the factors and the observations. Multiplication of factor loading and factor score matrices, will reproduce the data matrix.

In ERP analysis, by applying PCA it is expected to extract ERP subcomponents or components. However, there is not a one-by-one map between the extracted principal components (factors) and ERP subcomponents/components. The PCA generates those factors that account for maximum variance. These factors may be influenced by more than one ERP component/subcomponent after the initial extraction in the first step [108]. For example a factor can be a hybrid of two ERP components (e.g 90% of the one ERP component and 10% of another ERP component). Since the final goal in applying PCA is to have factors, each representing one ERP component/subcomponent, a post-processing technique should be performed on the extracted factors. The used technique is factor rotation. Factor rotation is used to restructure the allocation of variables to those factors which are more likely to present the latent variables (ERP components/subcomponents). The most common factor rotation is Varimax [110].

In Varimax, the factors are rotated pairwise iteratively, until the change in the solution is trivial. The Varimax procedure rotates the two factors such that the sum of the factor loadings is maximized. Therefore, new factors are generated that are as close to zero for some variables as possible, while others are as large as possible. It is expected that these generated factors closely correspond to a single ERP component/subcomponent. This rotation process can be illustrated as a scatterplot in which the axes are the factors and each point represents a single variable. The rotation process rotates the axes of the coordinate system such that the axes pass through the most concentrated groupings of the points. In other words, the rotation arranges the factor loadings of each variable to be as large for one factor and as small for the other factors as possible.

The Varimax rotation is sensitive to the correlations and overlap between the ERP components/subcomponents. Therefore, it affects the accuracy of the system [108]. In both steps i.e. the initial extraction and Varimax rotation, the strict orthogonality is maintained between the factors (so the factors are assumed to be uncorrelated). Therefore, the correlation between ERP components/subcomponents violates the statistical uncorrelatedness assumptions. The more the ERP components/subcomponents are correlated, the more the solution will be inaccurate and produce misallocation of variance among the factors. However, component correlation is effectively addressed using oblique rotations such as Promax [111]. In Promax rotation, the correlation between the factors are allowed. Promax performs an initial Varimax rotation, then it relaxes the orthogonality restrictions which allows the factors to become correlated. Considering the scatter plot, this is equivalent to the Varimax rotation. However each axis is rotated separately and therefore, there is no need for the axes to be perpendicular. Therefore, if ERP components/subcomponents are correlated, using Promax rotation a more accurate solution will be obtained.

### Temporal PCA

In temporal PCA, the data matrix is organized in a way that the variables are the recorded potential at each time point, and the observations correspond to different waveforms recorded at each channel [108, 109]. Therefore, the number of variables is equal to the number of time points, and the number of observations is equal to the number of channels. After arrangement of the data matrix, PCA is applied to the data matrix for initial component extraction. Then, a factor rotation algorithm should be applied to the extracted factors. Previous results suggest that when using the temporal PCA, it is preferred to use the Promax rotation as the rotation algorithm [108]. The factor loadings which are the output of the temporal PCA algorithm correspond to the time course of each factor while the factor score corresponds to the magnitude of each factor for different channels.

Since the variables in temporal PCA algorithm are the recorded potentials at each time point, the output consists of the factors that are temporally uncorrelated. Therefore, if in an ERP dataset, the ERP components/subcomponents are highly correlated in temporal domain, it is very difficult for the temporal PCA to extract the factors which are uncorrelated in time domain. In this case it is very likely to obtain only one factor which is a mixture of two correlated factors. However, temporal PCA is very effective for the case that the ERP components/subcomponents are correlated in spatial domain while much less correlated in temporal domain. Thus, temporal PCA makes use of temporal domain information in order to separate spatially correlated ERP components/subcomponents. If the ERP components/subcomponents are more correlated in temporal domain rather than spatial domain, another approach should be applied. The previously suggested approach for decomposition of temporally correlated ERP components/subcomponents is spatial PCA which is explained in the following sub-section.

### Spatial PCA

In spatial PCA, the data matrix is organized in a way that the variables consist of potentials recorded at each channel and the observation corresponds to the recorded potentials at each time point [108, 109]. Therefore, the number of variables is equal to the number of channels and the number of observations is equal to the number of time points. After arrangement of the data matrix, the PCA is applied to the data matrix for initial component extraction. Then, as for temporal PCA, a factor rotation algorithm should be applied to the extracted factors. Previous results suggest that when using the spatial PCA, it is preferred to use the Infomax rotation [112] as the rotation algorithm [108]. The factor loadings, which are the output of the spatial PCA algorithm, correspond to the recorded voltage at each channel for each factor while the factor scores correspond to the magnitude of each factor at different time points.

Since the variables in spatial PCA algorithm are the measured voltage at each channel, the output consists of the factors that are spatially uncorrelated. Therefore, if in an ERP dataset, the ERP components/subcomponents are highly correlated in spatial domain, it is very difficult for the spatial PCA to extract factors which are uncorrelated in spatial domain. In this case it might have only one factor mixture of two correlated factors, since it is very difficult to distinguish between the factors in spatial domain. However, spatial PCA is very effective for the cases where the ERP components/subcomponents are correlated in temporal domain while much less correlated in spatial domain. Thus, spatial PCA makes use of spatial domain in order to separate temporally correlated ERP components/subcomponents. Therefore, the choice of applying spatial PCA or temporal PCA depends on the specification of the ERP dataset. If the ERP components/subcomponents are more correlated in temporal domain, the spatial PCA should be applied. If the ERP components/subcomponents are more correlated in spatial domain, temporal PCA should be applied.

### Spatio-temporal PCA

To address limitations of temporal PCA and spatial PCA, a two step procedure has been recently proposed [113]. In the two step procedure the spatial PCA is applied in the first step while temporal PCA is applied in the second step. The method is called spatio-temporal PCA. However, if in the first step temporal PCA and in the second step spatial PCA is applied, then, the method is called temporospatial PCA. In spatio-temporal PCA, after applying spatial PCA (considering channels as variables) the resulted factor score should be rearranged. Since in the second step temporal PCA is applied to each resulted factor scores, the factor scores should be rearranged in a way that the new variables are the time points. In fact this two step method must be applied to a dataset which consists of the multi-channel data matrix of several trials and/or from several subjects. In this way in the second step, when rearranging the factor score in to the new variables, the new observation corresponds to different trials from different subjects. It is obvious that the two-step PCA (spatio-temporal/temporospatial PCA) is not suitable for single trial analysis of ERP data from one subject, since in this case the number of observation in the second step will be equal to one and the second PCA can not be performed.

It is also suggested to use the two-step PCA for general cases where the specification of ERP dataset is not known [113]. For example, if a dataset consists of

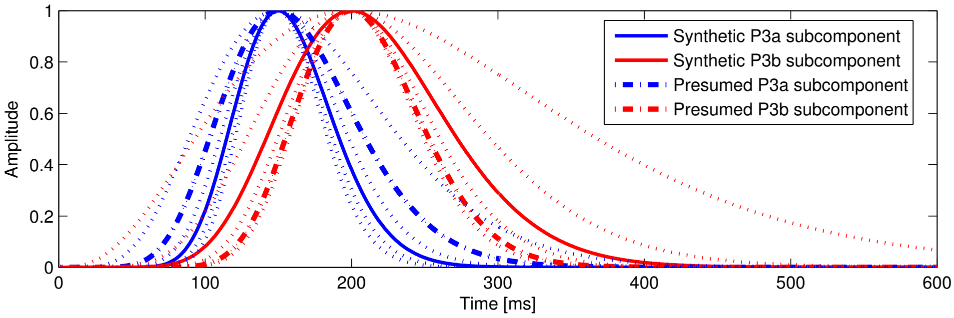

Figure 6.1: Synthetic and presumed reference signals for P3a and P3b used in the simulation study. The waveforms with dotted lines represent different approximations for actual signals and two of them are selected as the presumed reference signals for simulating the Mismatch case.

mixtures of ERP components/subcomponents, which some of them can be separated temporally and some of them spatially, the two-step PCA provides a generally applicable procedure. However, if the ERP components/subcomponents can be clearly separated in spatial domain or in temporal domain, the corresponding one-step approach is preferred to take advantage of the stronger statistical power. Therefore, the two-step PCA algorithm is a general approach for a dataset having mixtures of different ERP components/subcomponents also when the ERPs are recorded from multiple trials or multiple subjects.

### 6.4.2 Comparison Study

In this section, a set of simulated data were generated to compare the results of the proposed method with the existing methods. Two Gamma waves were generated as the representations of ERP subcomponents and the method is applied in order to quantify the estimation error of their descriptors (latency, amplitude, and scalp projections). For simplicity, we called the first subcomponent P3a and the second subcomponent P3b. The Gamma waves were used as approximations of the P300 subcomponents. The simulated subcomponents are shown in Fig. 6.1 as the synthetic P3a and P3b subcomponents. These subcomponents have temporal correlation of 0.69 (0 refers to no temporal correlation and 1 to perfect temporal correlation). So, they are highly correlated in the temporal domain. We used a three layer spherical head model with conductivities of 0.33, 0.0042, 0.33 $\mu S/cm$, for scalp, skull, and brain, respectively [114].

Then, we placed P3a and P3b in frontal and posterior parts of the brain respectively. The locations for simulated P3a and P3b are shown in Fig. 6.2.

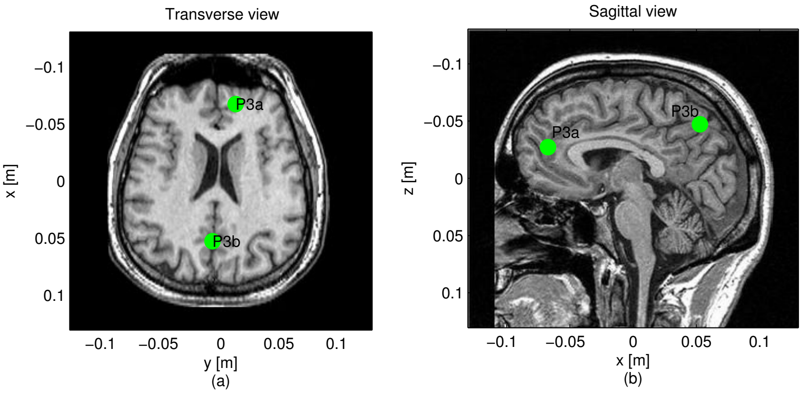

Figure 6.2: Locations of the simulated P3a and P3b inside the brain; (a) transverse view, (b) sagittal view.

Using the forward model obtained by the BrainStorm software [115] and setting the moments for P3a and P3b in three different axes, scalp projections of P3a and P3b are generated. These scalp projections are the results of multiplication of the forward matrix and moments of each subcomponent. The spatial correlations are considered as the correlation between the scalp projections. The spatial correlation for the simulated P3a and P3b was set to 0.26 (0 refers to no spatial correlation and 1 to perfect spatial correlation). Then, using equation (6.3), a 20 channel dataset was generated. Each channel included 40 trials. In all of the trials the latency of P3a was fixed at 150 ms and the latency of P3b was fixed at 200 ms as in Fig. 6.1. The amplitudes of P3a and P3b change in different trials. The variance of the noise was fixed at all the trials.

First, we applied the method to the generated simulated data considering the reference signal as the actual synthetic source. We called this method Exact match. Then, we used other reference signals for P3a and P3b which were not exactly the same as the actual synthetic sources. These waves for P3a and P3b are shown in Fig. 6.1 as the presumed P3a and P3b subcomponents. The method considering these references is called Mismatch.

As explained in the previous section, the spatial PCA is expected to be more effective when the aim is separation of the components with similar time courses while temporal PCA is expected to be more effective at separating components with similar scalp topographies [108, 109]. Since in our simulation the temporal correlation is high, it is reasonable to compare the results with spatial PCA rather than temporal PCA. Then, we used spatial PCA from ERP PCA Toolkit [116] in which the ICA Infomax [117] is used as the rotation algorithm. We considered 40 trials in 9 different SNR levels. The SNR in dB is defined as:

$$\text{SNR} = 10log_{10}(\frac{P_{signal}}{P_{noise}}) \tag{6.37}$$

The results of estimation of scalp projections, amplitudes, and latencies of P3a and P3b by applying the above three methods (spatial PCA, Exact match and Mismatch) are shown in Table 6.1, Table 6.2, and Table 6.3 respectively. The mean correlation coefficient between the estimated and actual scalp projections for P3a and P3b in 40 trials using three methods are shown in Table 6.1.

One drawback of using spatial PCA is that there are situations in which it fails to reconstruct both subcomponents. In this case, however, one subcomponent has been estimated with a good accuracy; the estimation for another subcomponent is far away from the actual subcomponent. For example, in some trials when the spatial PCA fails to estimate one subcomponent, the correlation coefficient between the estimated and actual scalp projection for that subcomponent is close to zero. We discarded those trials in which spatial PCA fails to estimate one subcomponent and only considered the case that spatial PCA is able to estimate both subcomponents. From Table 6.1 it can be seen that generally when SNR decreases the number of discarded trials increases.

In the estimation of scalp projections of P3a and P3b in negative SNR, Exact match and Mismatch methods provide very good approximations. Therefore, with respect to scalp projection estimation our method outperforms spatial PCA. For P3b we have consistent results for SNRs of -8 to 8. So, when the SNR increases, the correlation coefficient between the estimated and actual scalp projections tends to 1. Also, there is a slight difference between the Exact match and Mismatch methods. This is what we expect from the designed filter. Because the designed filter in the left hand side of equation (6.27) is able to estimate the

Table 6.1: Scalp projection estimation for P300 subcomponents in different SNRs for different methods. The values are mean correlation coefficients between the estimated and actual scalp projections in 40 trials

| | P3a Scalp projection | | | P3b Scalp projection | | | |
|---|---|---|---|---|---|---|---|
| SNR(dB) | PCA | Exact Match | Mismatch | PCA | Exact Match | Mismatch | Discarded Trials |
| −8 | 0.6444 | 0.9371 | 0.9357 | 0.6501 | 0.9156 | 0.9019 | 64% |
| −6 | 0.7432 | 0.9677 | 0.9632 | 0.7580 | 0.9470 | 0.9343 | 48% |
| −4 | 0.8171 | 0.9800 | 0.9703 | 0.8820 | 0.9652 | 0.9523 | 23% |
| −2 | 0.8784 | 0.9840 | 0.9685 | 0.9292 | 0.9819 | 0.9704 | 18% |
| 0 | 0.9057 | 0.9810 | 0.9580 | 0.9454 | 0.9910 | 0.9832 | 16% |
| 2 | 0.9225 | 0.9735 | 0.9428 | 0.9291 | 0.9961 | 0.9913 | 9% |
| 4 | 0.9307 | 0.9688 | 0.9354 | 0.9296 | 0.9974 | 0.9957 | 6% |
| 6 | 0.9199 | 0.9625 | 0.9256 | 0.9051 | 0.9975 | 0.9975 | 14% |
| 8 | 0.9037 | 0.9598 | 0.9215 | 0.8847 | 0.9984 | 0.9976 | 16% |

scaled scalp projection of one subcomponent, when we use the reference signals, there is a change in that scale. In a low noise situation this has very little effect (because of normalization of the left hand side of equation (6.27)).

However for P3a we have inconsistency in all methods. These inconsistencies can be explained in terms of having 0.26 spatial correlation between the subcomponents. In Table 6.1 the increase in the correlation coefficient of the actual and estimated P3a scalp projection with the increase in the noise level is mainly because more noise can decrease the correlation between the subcomponents. In Table 6.1, the noise effect in decreasing the correlation, and as a result, better estimation can be seen in some ranges of SNRs for all the methods.

For confirmation of robustness we performed another experiment considering two scalp projections which had a small spatial correlation of 0.1 and the results were consistent for nearly all other methods. In Table 6.2 the mean and variance of the ratio between the actual and estimated amplitudes in 40 trials are shown considering all the methods. When SNR increases this ratio tends toward 1 for all methods. In the amplitude estimation a bias can be seen for the Exact match and Mismatch methods.

Regarding amplitude estimation, spatial PCA results in a better estimation. In Table 6.3, the mean and variance of estimated latency in 40 trials is shown considering the three methods. From this table, it can be seen that considering Exact match method, the mean of estimated latency for P3a tends to 150 and for P3b towards 200 with the increase in SNR. Also the variance of estimation continuously decreases when the SNR increases. In the case of Mismatch, a bias in latency estimation can be seen, however, the variance of estimation decreases when the SNR increases.

Regarding latency estimation, the Exact match method outperforms the spatial PCA and Mismatch methods. Since, with decrease in the SNR level, the variance of estimation for spatial PCA increases, Mismatch method seems to

Table 6.2: Amplitude estimation for P300 subcomponents in different SNRs for different methods. The values are means and variances of the ratios between the actual and estimated amplitudes in 40 trials.

| | P3a Amplitude | | | P3b Amplitude | | |
|---|---|---|---|---|---|---|
| SNR(dB) | PCA | Exact Match | Mismatch | PCA | Exact Match | Mismatch |
| $-8$ | $0.9872 \pm 0.1130$ | $1.9841 \pm 0.1030$ | $1.9882 \pm 0.1785$ | $1.3364 \pm 0.1787$ | $1.7276 \pm 0.1506$ | $1.8001 \pm 0.1356$ |
| $-6$ | $1.0130 \pm 0.1000$ | $1.6423 \pm 0.1072$ | $1.6691 \pm 0.1030$ | $1.3335 \pm 0.0837$ | $1.4022 \pm 0.1436$ | $1.4634 \pm 0.1410$ |
| $-4$ | $1.0857 \pm 0.0873$ | $1.5054 \pm 0.0929$ | $1.5434 \pm 0.0909$ | $1.4230 \pm 0.1435$ | $1.2766 \pm 0.0922$ | $1.3387 \pm 0.0917$ |
| $-2$ | $1.1309 \pm 0.0708$ | $1.3971 \pm 0.0592$ | $1.4509 \pm 0.0508$ | $1.4224 \pm 0.1317$ | $1.2119 \pm 0.0796$ | $1.2703 \pm 0.0721$ |
| 0 | $1.1349 \pm 0.0540$ | $1.3160 \pm 0.0549$ | $1.3857 \pm 0.0648$ | $1.3561 \pm 0.1092$ | $1.0941 \pm 0.0688$ | $1.1616 \pm 0.0675$ |
| 2 | $1.1179 \pm 0.1110$ | $1.2767 \pm 0.0625$ | $1.3534 \pm 0.0630$ | $1.2941 \pm 0.0716$ | $1.0239 \pm 0.0416$ | $1.0982 \pm 0.0475$ |
| 4 | $1.1302 \pm 0.0301$ | $1.2192 \pm 0.0412$ | $1.2956 \pm 0.0437$ | $1.2747 \pm 0.0636$ | $1.0012 \pm 0.0459$ | $1.0782 \pm 0.0489$ |
| 6 | $1.1085 \pm 0.0703$ | $1.2042 \pm 0.0367$ | $1.2858 \pm 0.0406$ | $1.2436 \pm 0.0500$ | $0.9668 \pm 0.0296$ | $1.0428 \pm 0.0261$ |
| 8 | $1.0927 \pm 0.0538$ | $1.1807 \pm 0.0326$ | $1.2678 \pm 0.0381$ | $1.2077 \pm 0.0478$ | $0.9464 \pm 0.0282$ | $1.0256 \pm 0.0263$ |

be more robust. If we evaluate and compare only Exact match and Mismatch methods, we can see that the best approximation is for the scalp projections. Therefore, in the case of Mismatch a bias in latency and amplitude estimation can be seen. This is because we directly designed a filter for estimation of scalp projections of one subcomponent considering two reference signals. Then, we showed that in the case of having reference signals, which are not necessarily the exact source signals, there is a scale change with no effect after normalization. Therefore, the estimated scalp projection in the case of Mismatch in low noise conditions is almost independent of the shape of reference signal. However, we do not directly estimate the latencies and amplitudes of the subcomponents; instead, we use the estimated scalp projections and some other cost functions as shown in Algorithm 6.3. Therefore, in the case of Mismatch, the more the reference signal is similar to the exact signal, the better estimation for latency and amplitude is achieved.

### Effect of real noise

In an experiment, we used 600ms pre-stimulus data as the background EEG and used it as noise. Therefore, in SNR calculation the power of background EEG is considered as the power of noise. For SNR close to 0, the results of averaging over 40 trials are shown in Table 6.4.

The aim of this experiment was to compare the performance of three methods in the case of having a non-Gaussian and non-linear noise which is more realistic. It can be seen that the Exact Match outperforms the Mismatch method and both of them outperform PCA method. Also it seems that PCA method is less robust in the case of having only background EEG as the noise.

### Effect of reference mismatch

Table 6.3: Latency estimation for P300 subcomponents in different SNRs for different methods. The values are means and variances of the estimated latencies in 40 trials.

| | P3a Latency | | | P3b Latency | | |
|---|---|---|---|---|---|---|
| SNR(dB) | PCA | Exact Match | Mismatch | PCA | Exact Match | Mismatch |
| $-8$ | $204.0667 \pm 109.1588$ | $153.3000 \pm 2.6929$ | $158.6333 \pm 4.7885$ | $187.2667 \pm 42.0344$ | $208.0333 \pm 6.8857$ | $193.5333 \pm 10.9505$ |
| $-6$ | $160.4333 \pm 58.1903$ | $154.6667 \pm 2.0567$ | $164.7000 \pm 4.4346$ | $199.5667 \pm 31.1389$ | $202.4333 \pm 5.7816$ | $184.6000 \pm 8.4225$ |
| $-4$ | $147.6000 \pm 17.4111$ | $154.6333 \pm 1.9737$ | $165.4667 \pm 3.2667$ | $217.7667 \pm 24.8231$ | $200.7333 \pm 4.0166$ | $182.2667 \pm 6.3078$ |
| $-2$ | $152.7000 \pm 8.2927$ | $153.6667 \pm 1.5610$ | $163.9000 \pm 2.8569$ | $213.2667 \pm 19.6362$ | $198.7667 \pm 3.5495$ | $184 \pm 9.1576$ |
| 0 | $148.2333 \pm 6.7194$ | $153.0667 \pm 0.9072$ | $163.6333 \pm 2.1088$ | $216.8667 \pm 15.0143$ | $197.3000 \pm 4.0099$ | $181.0333 \pm 5.6598$ |
| 2 | $150 \pm 8.2838$ | $151.9000 \pm 0.8847$ | $162.6000 \pm 1.6316$ | $213.8333 \pm 19.8791$ | $198.7333 \pm 3.5227$ | $189.5667 \pm 14.8804$ |
| 4 | $149.4000 \pm 4.4458$ | $151.2667 \pm 0.6915$ | $162.4333 \pm 1.1651$ | $220.2333 \pm 13.9350$ | $198.4000 \pm 2.9431$ | $208.4000 \pm 14.4857$ |
| 6 | $148.2667 \pm 6.2474$ | $150.7667 \pm 0.5040$ | $164.2667 \pm 0.8277$ | $217.8667 \pm 13.7984$ | $198.5667 \pm 2.3146$ | $218.0333 \pm 1.1885$ |
| 8 | $146.7667 \pm 5.4815$ | $150.4000 \pm 0.4983$ | $165.2333 \pm 0.6261$ | $216.8000 \pm 10.7748$ | $198.8667 \pm 1.7564$ | $219.2000 \pm 0.6644$ |

In Table 6.5 we tried to show the effects of different choices for reference signals. We changed the shape of P3a and P3b by changing their $k$ and $\theta$ values in equation (6.29) and generated different reference signals which are shown in Fig. 6.1 as dotted lines. From Table 6.5 it can be seen that with different degrees of Mismatch we have different bias in estimation. When the Mismatch is very high as it can be seen from the $15^{th}$ row of Table 6.5, there is a high bias in latency estimation. The estimations in Table 6.5 are the average estimation considering 15 trials at SNR 0. The bold row corresponds to our special reference choice for P3a and P3b (presumed P3a and P3b in Fig. 6.1).

### Effect of spatial correlation

In another experiment we kept the temporal correlation at 0.69 for P3a and P3b as in Fig. 6.1. We then changed the locations and moments of P3a and P3b in the brain in order to generate different levels of spatial correlations. In each level, we generated 15 trials. By considering all the methods (and two different SNR levels of -5 and 0), we calculated the average of correlation coefficients between the estimated and actual scalp projections which are shown in Fig. 6.3 for both SNRs. The Exact match and Mismatch methods outperform the spatial PCA in less than 0.9 spatial correlations. In both SNR levels the performances of Exact match and Mismatch methods drop as the spatial correlation approaches 1. For spatial correlation less than 0.9, Exact match and Mismatch methods outperform the spatial PCA.

### Effect of temporal correlation

Our method is compared with temporal PCA from ERP PCA Toolkit [116] in different temporal correlations considering two SNR levels of -5 and 0. In temporal PCA algorithm, Promax is used as the rotation algorithm with the rotation parameter 3, the relationship matrix type is covariance based, and the loading normalization is Kaiser. The results are illustrated in Fig. 6.4. The spatial correlation between the subcomponents is 0.26 and the result is the average of the results for 15 trials. It is clear that the performance of the temporal PCA

Table 6.4: P300 subcomponents parameter estimation at SNR = 0 dB considering background EEG as noise.

| | P3a | | | P3b | | |
|---|---|---|---|---|---|---|
| *Parameter* | PCA | Exact Match | Mismatch | PCA | Exact Match | Mismatch |
| *Scalp Projection* | 0.7044 | 0.8944 | 0.8614 | 0.8890 | 0.9620 | 0.9584 |
| *Amplitude* | $0.7087 \pm 0.0667$ | $1.1759 \pm 0.2063$ | $1.1843 \pm 0.2067$ | $0.7968 \pm 0.0306$ | $0.9833 \pm 0.1166$ | $0.9600 \pm 0.1263$ |
| *Latency* | $136.0667 \pm 19.8302$ | $150.7000 \pm 0.8367$ | $165.6667 \pm 2.2335$ | $230.3667 \pm 35.9976$ | $200.6333 \pm 3.6054$ | $219.2333 \pm 1.1943$ |

degrades with the increase in the temporal correlation. In addition, low noise situation has an adverse effect in temporal PCA. Clearly, our method, which exploits both temporal and spatial domain and has no assumption on the uncorrelatedness or orthogonality of the subcomponents either in time or spatial domain, outperforms the PCA/ICA based methods.

Finally, we tried to show a single trial estimation of scalp projection, amplitude, and latency of P3a and P3b considering all three methods (spatial PCA, Exact match and Mismatch). For these single trials, the latencies and amplitudes of P3a and P3b change in different trials; therefore we have different temporal correlations between P3a and P3b. In Fig. 6.5 the correlation coefficients of estimated and actual scalp projections and latency estimation in the 30 single trials are provided. In Fig. 6.6 the amplitude estimation is shown, in addition, in this figure, the temporal correlation between P3a and P3b and SNR values in each trial are shown. In the next section the method is applied to the real data and the results are provided.

## 6.5 Real Data Results

The EEG data were recorded using a Nihon Kohden model EEG-F/G amplifier and Neuroscan Acquire 4.0 software. The international $10-20$ electrode setting system was used to record EEG activity from 15 electrodes. The impedance for all the electrodes was below $5k\Omega$. The sampling frequency ($F_s$) was 2kHz and the data were bandpass filtered (0.1 – 70 Hz). This frequency range was chosen to be consistent with [118]. In order to avoid any interference, the subjects were required to sit alert with their eyes closed.

In addition, in order to avoid any muscle artefact, the neck was firmly supported by the back of the chair, feet were rested on a footstep, and stimuli

Table 6.5: Effects of Mismatch in P300 subcomponents descriptor's estimation.

| | K - P3a | K - P3b | K | P3a latency | P3a amplitude | P3a scalp | K | P3b Latency | P3b amplitude | P3b scalp |
|---|---|---|---|---|---|---|---|---|---|---|
| 1 | Fix | decrease | 22 | 156.3333 ± 1.0465 | 1.1814 ± 0.0532 | 0.9889 | 9 | 192.0667 ± 2.5204 | 1.2033 ± 0.0712 | 0.9922 |
| 2 | Fix | decrease | 22 | 161.4667 ± 1.5055 | 1.1055 ± 0.0491 | 0.9892 | 4 | 190.5333 ± 2.0656 | 1.2641 ± 0.0695 | 0.9911 |
| 3 | Fix | increase | 22 | 150.2667 ± 1.1629 | 1.2953 ± 0.0649 | 0.9619 | 19 | 208.1333 ± 4.1381 | 1.1752 ± 0.0846 | 0.9939 |
| 4 | Fix | increase | 22 | 150.3333 ± 1.1751 | 1.3289 ± 0.0697 | 0.9496 | 24 | 213.6000 ± 2.9228 | 1.1705 ± 0.0865 | 0.9942 |
| 5 | decrease | Fix | 17 | 155.2667 ± 0.9612 | 1.2618 ± 0.0619 | 0.9766 | 14 | 196.8000 ± 5.2807 | 1.1567 ± 0.0797 | 0.9914 |
| 6 | decrease | Fix | 12 | 163.5333 ± 1.3020 | 1.3024 ± 0.0609 | 0.9753 | 14 | 189.6667 ± 5.2327 | 1.1015 ± 0.0757 | 0.9917 |
| 7 | increase | Fix | 27 | 150.4000 ± 0.9103 | 1.2760 ± 0.0601 | 0.9766 | 14 | 198.3333 ± 4.5930 | 1.1522 ± 0.0786 | 0.9953 |
| 8 | increase | Fix | 32 | 149.3333 ± 0.8997 | 1.2678 ± 0.0573 | 0.9765 | 14 | 197.7333 ± 4.6517 | 1.1688 ± 0.0806 | 0.9946 |
| 9 | increase | increase | 27 | 148.3333 ± 1.1629 | 1.2909 ± 0.0621 | 0.9620 | 19 | 207.7333 ± 3.7315 | 1.1954 ± 0.0863 | 0.9920 |
| 10 | increase | increase | 32 | 148.2000 ± 1.1464 | 1.3409 ± 0.0680 | 0.9498 | 24 | 211.9333 ± 2.8402 | 1.1616 ± 0.0856 | 0.9946 |
| 11 | decrease | decrease | 17 | 160.2667 ± 1.3345 | 1.2794 ± 0.0543 | 0.9896 | 9 | 191.8000 ± 2.3361 | 1.1275 ± 0.0662 | 0.9912 |
| 12 | decrease | decrease | 12 | 170.0000 ± 0 | 1.2229 ± 0.0510 | 0.9881 | 4 | 191.4000 ± 2.4437 | 1.2248 ± 0.0712 | 0.9901 |
| 13 | decrease | increase | 17 | 153.0000 ± 1.0690 | 1.3481 ± 0.0635 | 0.9626 | 19 | 204.2000 ± 10.2901 | 1.0838 ± 0.0772 | 0.9911 |
| 14 | **decrease** | **increase** | **12** | **159.0000 ± 1.4639** | **1.3561 ± 0.0696** | **0.9492** | **24** | **195.3333 ± 17.1159** | **1.0832 ± 0.0797** | **0.9916** |
| 15 | decrease | increase | 7 | 170.0000 ± 0 | 1.4178 ± 0.0700 | 0.9419 | 27 | 180 ± 0 | 0.9834 ± 0.0750 | 0.9580 |
| 16 | increase | decrease | 27 | 154.2000 ± 1.0823 | 1.1725 ± 0.0493 | 0.9891 | 9 | 191.4667 ± 2.5317 | 1.2178 ± 0.0715 | 0.9897 |
| 17 | increase | decrease | 32 | 156.9333 ± 1.2799 | 1.0754 ± 0.0433 | 0.9895 | 4 | 188.8667 ± 2.1996 | 1.2820 ± 0.0688 | 0.9853 |

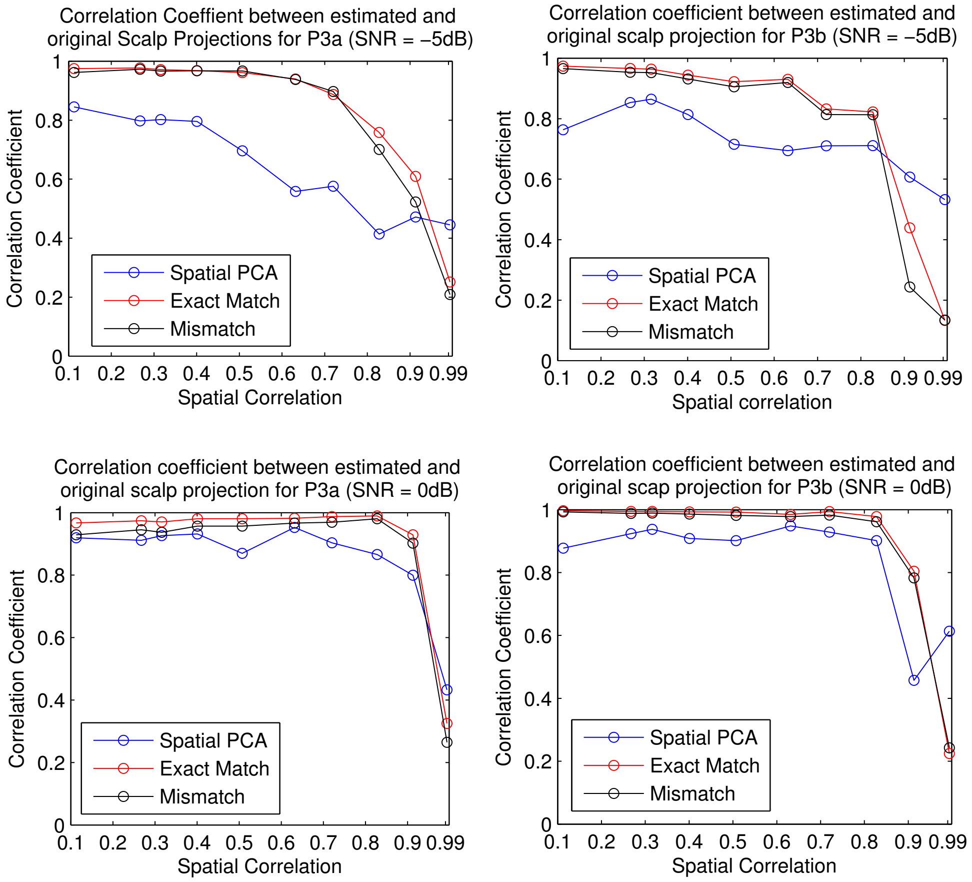

Figure 6.3: Comparison between three methods (spatial PCA, Exact Match and Mismatch) with respect to the correlation coefficient between the original and estimated scalp projections of P3a (left column) and P3b (right column) in different spatial correlations and two SNR levels of -5 dB (top row) and 0 dB (bottom row).

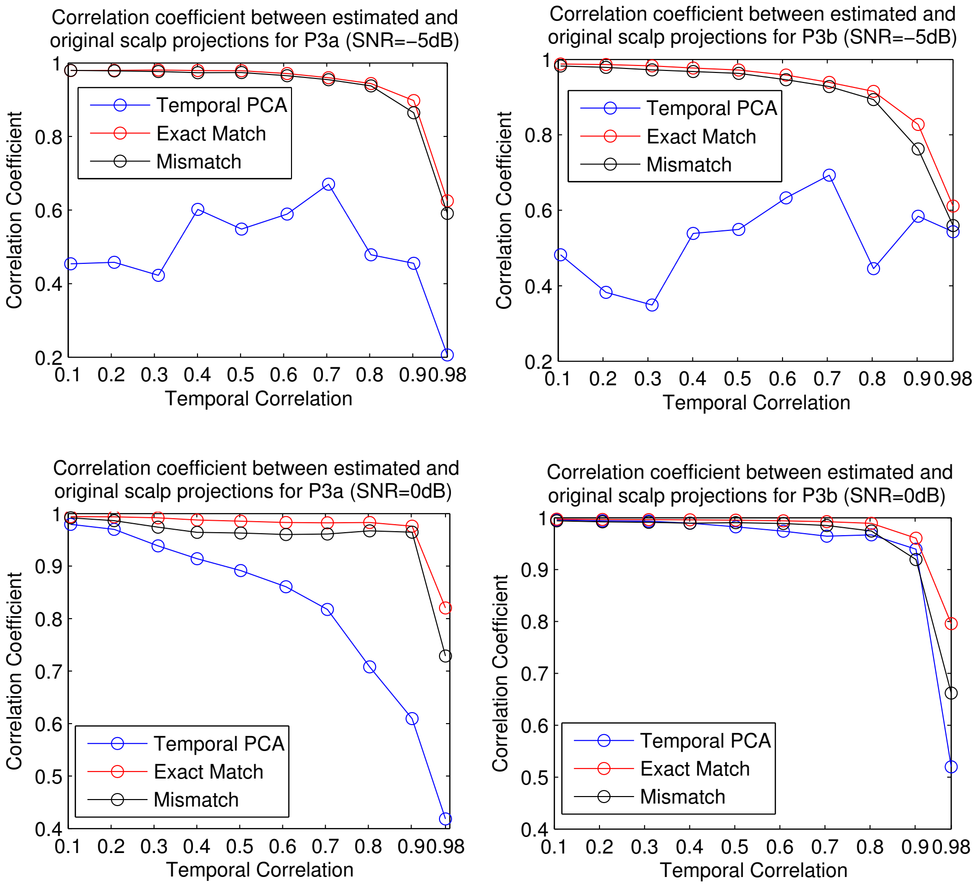

Figure 6.4: Comparison between three methods (temporal PCA, Exact Match and Mismatch) with respect to the correlation coefficient between the original and estimated scalp projections of P3a (left column) and P3b (right column) in different temporal correlations and two SNR levels of -5 dB (top row) and 0 dB (bottom row).

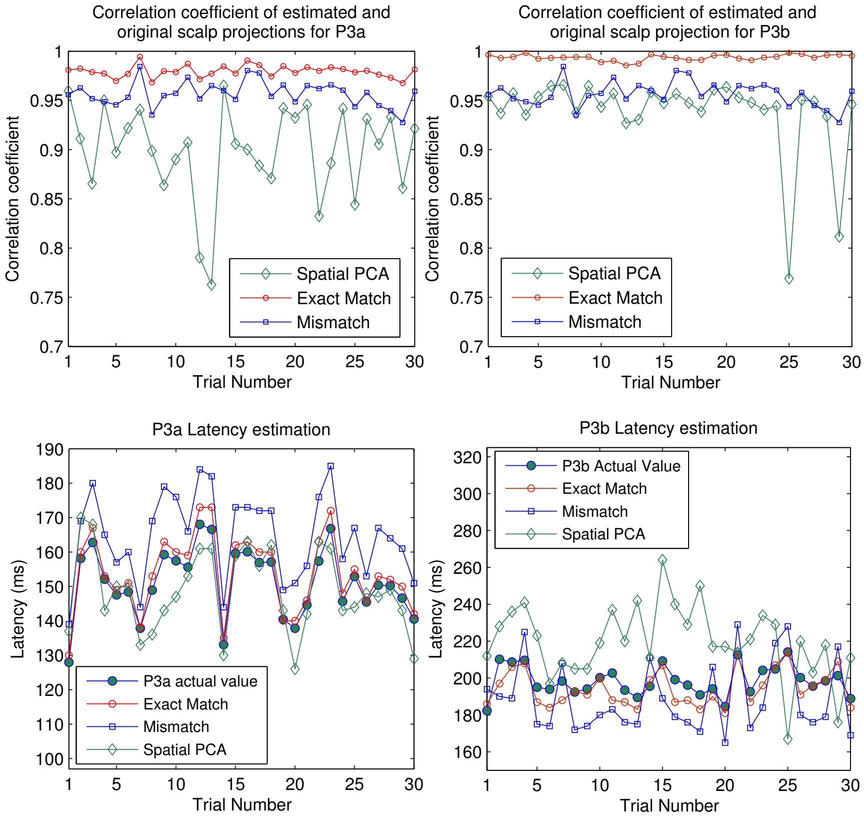

Figure 6.5: In the top row, the correlation coefficient between the original and estimated scalp projections of P3a and P3b obtained by the three methods (spatial PCA, Exact Match and Mismatch) in each trial are shown. In the bottom row, single trial estimation of latencies of P3a and P3b obtained by the three methods (spatial PCA, Exact Match and Mismatch) in each trial are shown.

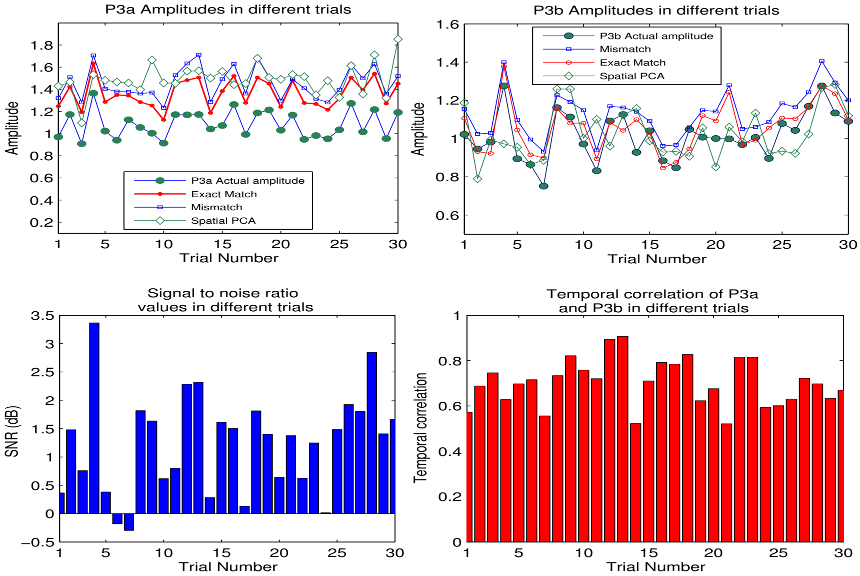

Figure 6.6: In the top row, single trial estimation of amplitudes of P3a and P3b obtained by the three methods (spatial PCA, Exact Match and Mismatch) in each trial are shown. In the bottom row, SNR and temporal correlations between P3a and P3b in each trial are shown.

were presented through ear plugs inserted in the ear. Forty rare tones (1 kHz) were randomly distributed amongst 160 frequent tones (2 kHz). Their intensity was 65 dB with 10- and 50-milliseconds duration for rare and frequent tones, respectively.

The subjects were asked to press a button as soon as they heard a low tone (1 kHz). Before the start of the experiment, the ability of the subject to distinguish between low and high tones was confirmed. The basis of the designed task is to assess basic memory processes. ERP components measured in this task included N100, P200, N200, P3a and P3b. Forty trials from one subject related to the infrequent (rare) tones were selected and the proposed method for estimation of latency, amplitude and scalp projections of P3a and P3b was applied. These trials and their average from channel Fz is shown in Fig. 6.7.

For selection of reference signals, we used the averaged P300 as it is shown in Fig. 6.8. In the top row the selected reference signals have little overlap with the average P300. The normalized estimated scalp projection using left hand side of equation (6.27) is depicted for both P3a and P3b. It can be seen that the scalp projection values for P3a are negative or very close to zero. This can be explained from equation (6.27) because the term $\mathbf{s}_1\mathbf{r}_1^T$ seems to be zero or very close to zero. We slide the references (with slight changes in their shapes)

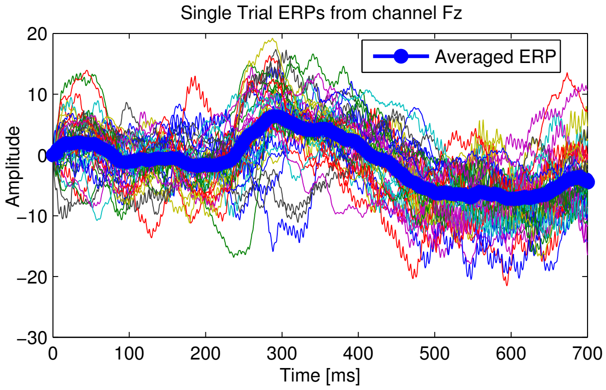

Figure 6.7: Single Trial ERPs (40 trials related to the infrequent tones) and their average from channel Fz.

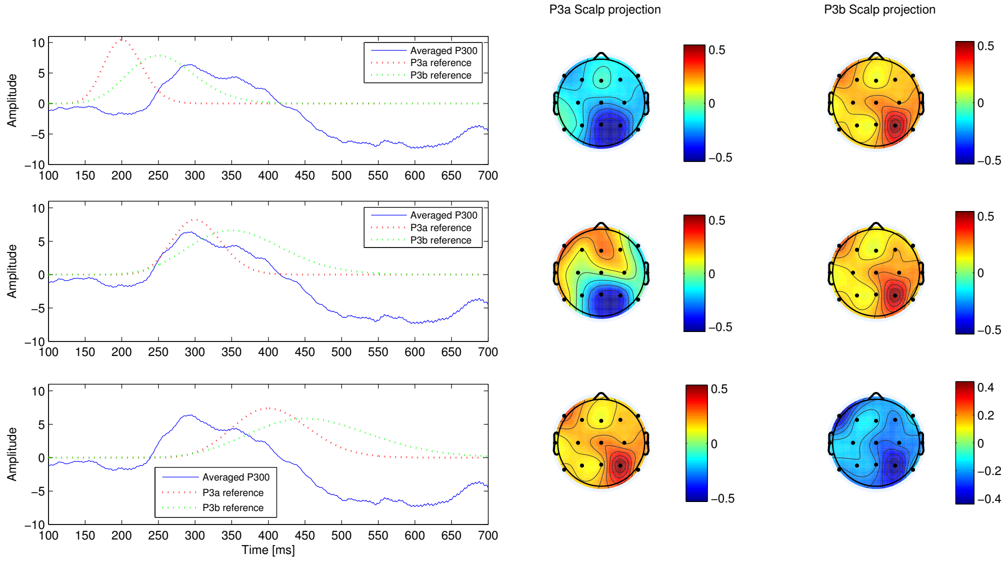

Figure 6.8: Selection of reference signals for P3a and P3b. In each row, the reference signals for P3a and P3b with their estimated scalp projections are shown. By sliding the reference signals towards and away from the averaged P300 and varying their shapes, the observed changes in their estimated scalp projections are helpful for reference selection. The reference signals shown in the middle row which have high correlation with the averaged P300 are used as good candidates for approximating the actual P3a and P3b.

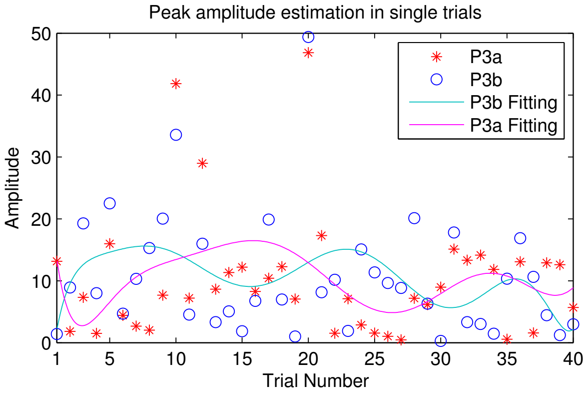

Figure 6.9: estimated amplitudes for P3a and P3b in different trials.

towards having more correlation with the average P300 as it is shown in the middle row.

The estimated scalp projections seem to be more reasonable since they do not contain only negative or very close to zero values. We can further slide the references as it is shown in the bottom row and we can see that this time the scalp projection for the second subcomponent has negative values in all the entries. In the top row, the reference signal for P3a seems to have no correlation (or very little correlation) with actual P3a so its estimated scalp projection has negative or very close to zero values in all entries, however it seems that there are some correlations between the reference signal and the actual signal for P3b. In the bottom row, the reference signal for P3a seems to have overlap with the actual P3b, therefore, in the first estimated subcomponent, P3b scalp projections appeared. The reference signal for P3b seems to have no correlation with actual P3b and the estimated scalp projection has negative values in all entries. It is also possible to use arbitrary shapes for P3a and P3b to see which shapes are more reasonable using the estimated scalp projections.

For our dataset, by testing different shapes for P3a and P3b, P3b shape was more likely to be wider than P3a. We have used the selected reference signals in middle row of Fig. 6.8 for P3a and P3b. After selecting the reference signals we estimated the amplitude, latency, and scalp projections of P3a and P3b in 40 trials.

The amplitude variations of the P3a and P3b are shown in Fig. 6.9. We fitted a polynomial with degree of 9 to P3a and P3b amplitudes in order to see the total variability across trials. The mean latency of P3a was obtained as 283.3ms and the mean latency of P3b was obtained as 367.6ms. The estimated

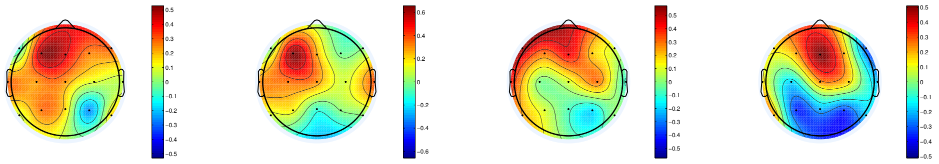

(a) (b) (c) (d)

Figure 6.10: Scalp projections of P3a in four selected progressive trials.

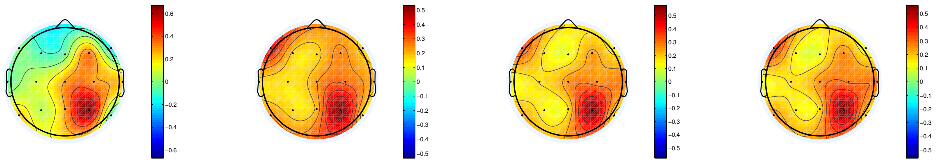

(e) (f) (g) (h)

Figure 6.11: Scalp projections of P3b in four selected progressive trials.

scalp projections of P3a and P3b in four selected trials are shown in Fig. 6.10 and Fig. 6.11. It can be seen from these figures that P3a has a more fronto-central distribution as expected and P3b has more posterior distribution. The scalp projections were plotted using EEGlab [117].

From Fig. 6.7 it can be seen that the average ERP lacks the early ERPs such as N100 and P200, however these ERPs were detected by using the average of trials related to the frequent tones. If in a dataset the early ERPs have large amplitudes and may interfere the estimation, it is useful to segment the data and extract the time-locked epochs, for example between 200ms and 500ms, and then apply the method for estimation of P300 subcomponents. The proposed method can be applied in order to investigate mental fatigue based on trial-to-trial amplitude and latency variations of the P300 subcomponents and the relative trends of P300 subcomponent variations. In addition, estimation of the scalp projections can be useful for detecting the changes in locations of P300 subcomponents for schizophrenic patients.

## 6.6 Conclusions

In this chapter a new spatio-temporal filtering method for single trial estimation of ERP subcomponents is proposed. The method defines new cost functions in which the scalp projection of each subcomponent can be obtained. The proposed method here overcomes the problem of the existence of temporal correlation between the ERP subcomponents in the previous research [103].

Based on the simulation results the method is robust in the estimation of latency, amplitude, and scalp projections. However, when there is a mismatch between a reference signal and the actual source, an offset error in estimation of the latency and amplitude occurs. This may not cause problems in some applications. However, the scalp projections of both subcomponents have been estimated with high accuracy even when there is a mismatch between the actual source and the reference signal. This is obvious, because the designed filter for estimation of the scalp projection is able to estimate the scaled scalp projection of one of the subcomponents. When there is a mismatch between the actual source and the reference signal, only the scale is changed. Therefore, the normalized version of the estimated scalp projection vector does not change; this is very important when we are dealing with localization of ERP subcomponents in the brain. Using the simulated signals, it is shown that our proposed method outperforms PCA/ICA based methods and a better approximation for scalp projections is obtained here. This leads to better localization of the subcomponents in the brain which can be exploited in another research.

The method also has been applied to real data. It has been shown that it is useful and effective for single trial estimation of P300 subcomponents. This is very demanding for some applications such as mental fatigue where the relative variability of ERP subcomponent descriptors is useful in order to determine the level of fatigue.

# Chapter 7

# Implementation of EEG-based and ERP-based Approaches to Detection of Mental Fatigue; an Auditory Based Paradigm

## 7.1 Introduction

In this chapter an auditory-based paradigm is proposed and implemented when EEG data is recorded in two states of alert and fatigue. The EEG data is recorded at the beginning of experiment while the subject is not fatigue. Then, at the end of experiment when the subject has completed a mental arithmetic task, EEG data is recorded in the fatigue state. The aim of this chapter is to apply the proposed methods in the previous chapters for spatio-temporal estimation of ERPs and EEG phase synchronization to the recorded EEG in an auditory-based paradigm which can be used for detection of fatigue state. The remainder of the chapter is structured as follows. In Section 7.2 the experimental setup is explained. Then, in Section 7.3 the results of applying the proposed method in Chapter 6 to the recorded data is provided. In Section 7.4 the EEG phase synchronization is estimated for the recorded data considering the proposed method in Chapter 4. Finally, Section 7.5 concludes the chapter.

## 7.2 Experimental Setup

The experiment was run in a quiet and normally illuminated room. The subject which was a 50 years old male was sitting comfortably in an armchair and had given informed consent before the start of experiment. The EEG data was recorded using a 32-channel QuickAmp amplifier and Ag/AgCl electrodes positioned according to the extended 10-20 system and re-referenced to linked ears. In addition, vertical (VEOG) and horizontal (HEOG) electrooculographic signals were recorded bipolarly using electrodes above and below the left eye and from the outer canthi. The EEG Data was recorded in DC mode at 1000 Hz with respect to an average reference. The EEG data is also notch filtered at 50 Hz.

The electrode positions are shown in Fig. 7.1. By adding gel, electrode impedances were reduced to less than $5k\Omega$. The EEG signal was recorded at the start of the experiment during the auditory oddball task. The subject heard 180 tones, 40 of them were infrequent tones while 140 of them were frequent tones. The subject was asked to respond to the infrequent tones by pressing a button. Each trial duration was set to 4 seconds.

After completing the initial recoding of the EEG, the subject was asked to perform a mental arithmetic task continuously for two hours. The subject had also the option of stopping the mental arithmetic task if he felt that he is very tired and is not willing to continue. The Matlab software was used to provide a demo which generates two random integers between 1 and 10. The subject had to enter the sum of the generated random numbers and then press ENTER key on the keyboard or 'Submit' button in the demo. The demo is shown in Fig. 7.2. After 2 hours performing the arithmetic task, the EEG data of the subject was recorded during the same auditory oddball task in the beginning of the experiment. In the next two sections the results of applying the proposed methods in Chapters 6 and 4 to the recorded EEG signal are provided.

## 7.3 Estimation of Single Trial P300 Subcomponents

Considering the results provided in Chapter 6, it is expected the P300 to be better elicited by infrequent tones. Therefore, using the spatio-temporal filtering method proposed in Chapter 6, it is possible to estimate P300 subcomponent parameters and evaluate their changes during the fatigue state considering the infrequent tones. The spatio-temporal filtering method was applied to the 40 trials relating to the infrequent tones in order to estimate P300 subcomponent parameters. One second of EEG signal after the stimulus onset in infrequent

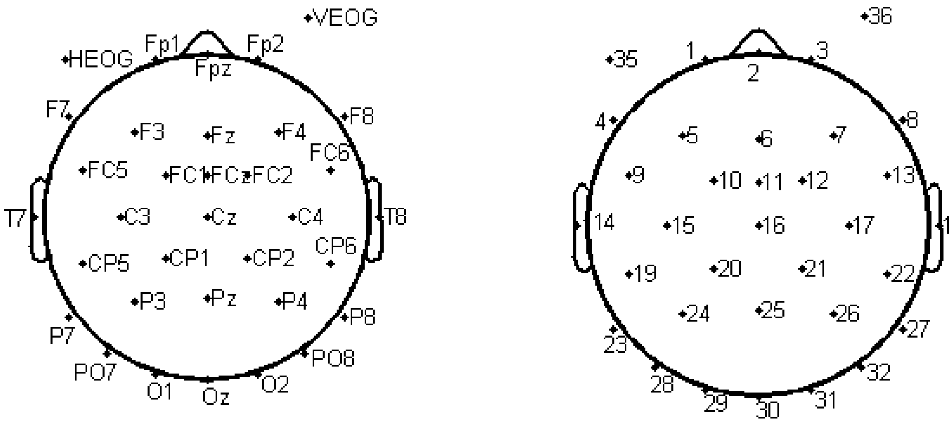

Figure 7.1: The electrode names (left) and numbers (right) which used in the experiment.

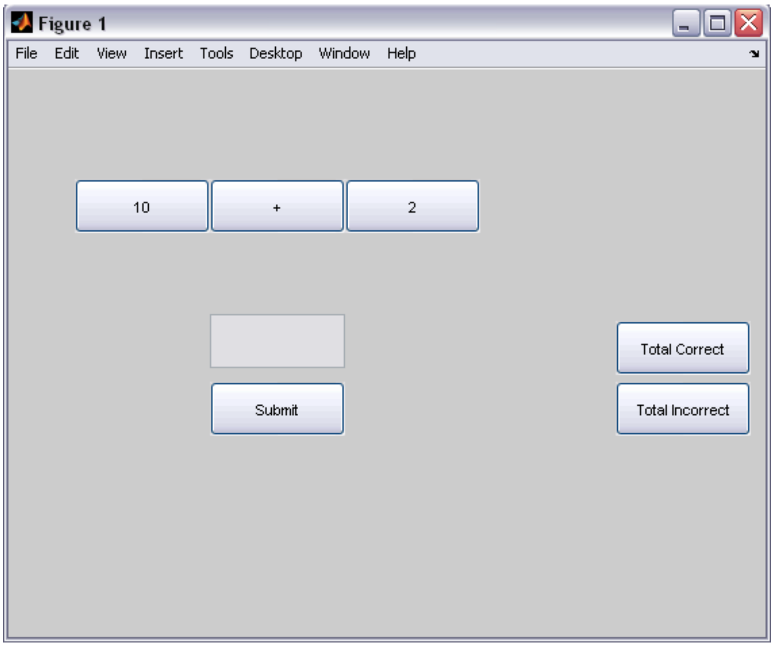

Figure 7.2: This GUI generates two random integers any time the subject presses ENTER key on the keyboard or ‘Submit’ button.

trials was segmented. The average of these trials (considering 600ms) from Cz channel was used in order to select appropriate reference signals. Forty single trial ERPs from channel Cz and their average before and during fatigue are shown in Fig. 7.3 and Fig. 7.4 respectively. The two averaged ERPs are shown separately in Fig. 7.5 for the two states of before and during fatigue. These average ERPs are used in order to select an appropriate reference signal for P3a and P3b. As it is shown in Chapter 6, the reference signals should have high correlation with the averaged ERP.

It can be seen from the averaged ERPs that as expected in the fatigue state there is a reduced amplitude and increased latency in the P300 wave. However the reduction in amplitude is very trivial and this is not always a sign of fatigue state. In addition the increased latency does not necessary correspond to the increased latency in all single trials since it is averaged over only one channel considering 40 trials. Therefore, there is a need for single trial estimation of the ERPs.

The spatio-temporal filtering method proposed in Chapter 6 is applied to the single trial ERPs before and during fatigue state to estimate P300 subcomponent descriptors (latency, amplitude, and scalp projections). The mean latency of P3a and P3b before fatigue state was obtained as 279.6 ms and 335.5 ms respectively. The mean latency of P3a and P3b during fatigue state was obtained as 325.5 ms and 372.2 ms respectively. As expected, the latency of P3a and P3b are increased in the fatigue state. The estimated amplitudes of P3a and P3b are shown in Fig. 7.6 and Fig. 7.7. By fitting a polynomial of degree 10 to the estimated P3a and P3b amplitudes before and during fatigue state, it can be seen that in the fatigue state there is a less variability in P3a and P3b amplitudes in single trials. The scalp projections of P3a and P3b for five selected trials are shown in Fig. 7.8 and Fig. 7.9 for before and during fatigue state respectively.

Although there is not a significant difference in the estimated scalp projections for P3a and P3b before and during fatigue state, the important issue is the separation of these subcomponents and estimation of other parameters. The results obtained by considering one subject confirm that the suggested paradigm can be a good option for designing a mental fatigue detection system in future studies and the estimation of P300 subcomponent parameters can be good features for discriminating the fatigue state. However, the full mental fatigue analysis should be conducted using more subjects and more features which can be obtained from both EEG and ERP. Other important features can be obtained using phase synchronization measures. In the next section, the proposed adaptive methods in Chapter 4 are used to measure the EEG phase synchronization to the recorded EEG data.

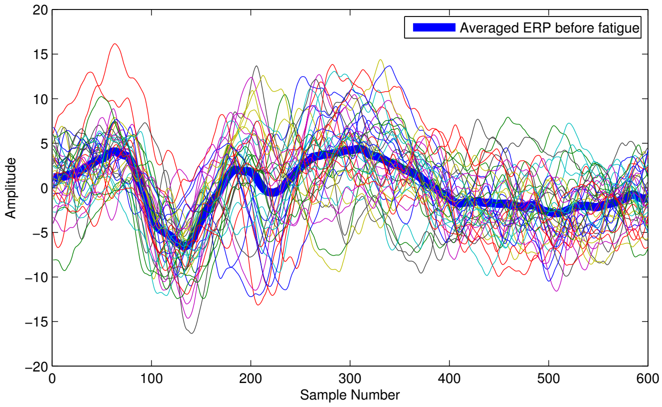

Figure 7.3: Forty single trial ERPs and their average from Cz channel before fatigue.

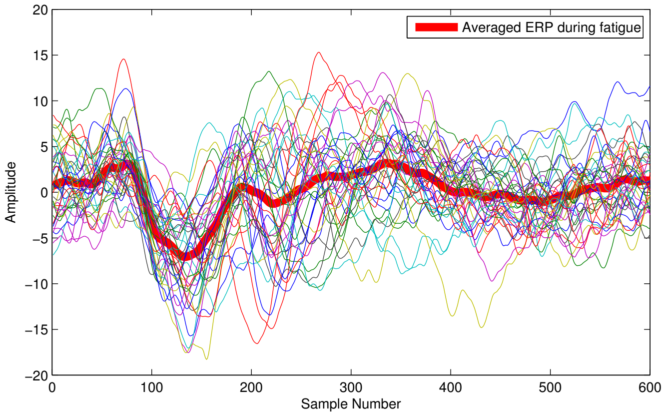

Figure 7.4: Forty single trial ERPs and their average from Cz channel during fatigue state.

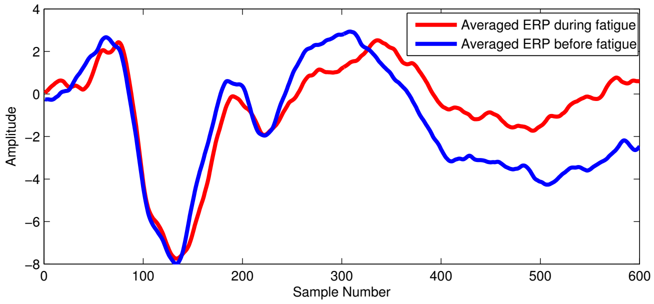

Figure 7.5: The averaged ERP of forty trials before and during fatigue state from Cz channel.

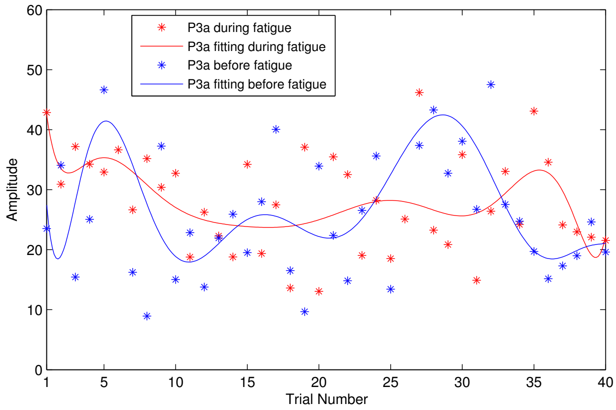

Figure 7.6: The estimated P3a amplitudes in single trials before and during fatigue state.

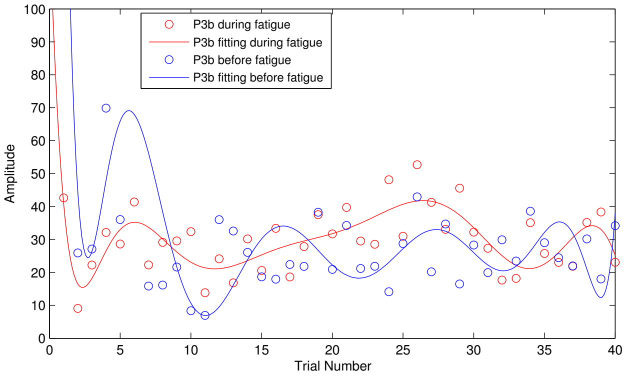

Figure 7.7: The estimated P3b amplitudes in single trials before and during fatigue state.

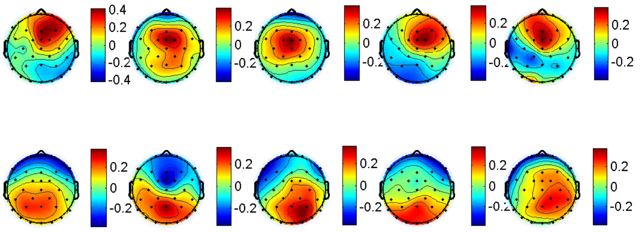

Figure 7.8: The estimated scalp projections of P3a (top row) and P3b (bottom row) before fatigue.

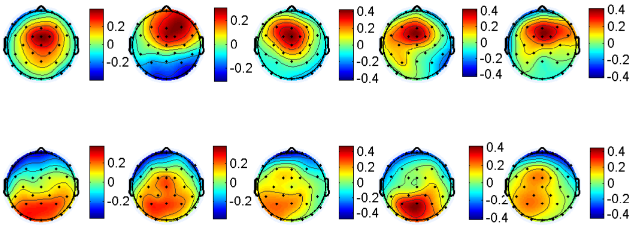

Figure 7.9: The estimated scalp projections of P3a (top row) and P3b (bottom row) during fatigue.

## 7.4 Estimation of EEG Phase Synchronization

Considering the results provided in Chapter 4, the phase synchronizations of different EEG rhythms especially alpha rhythm can be used as good features for discrimination of the fatigue state. Three seconds of the data segment is considered and EMD is applied to decompose the EEG signal into its oscillations. For beta rhythm, ALE is applied to the resulted IMF. One second of data segment (1000 samples) before stimulus onset and one second after stimulus onset are considered for measuring the phase synchronization.

Beta and theta rhythms are extracted from frontal electrodes (F3 and F4 channels) and alpha rhythm is extracted from central electrodes (C3 and C4 channels). The phase synchronization is calculated for five trials for one second before and after stimulus onset. The results of calculated phase synchronization for theta, alpha, and beta rhythms are shown in Fig. 7.10, Fig. 7.11, and Fig. 7.12 respectively.

In these figures the average phase synchronization is also depicted in thick line. From these figures the changes in phase synchronization can be clearly seen for beta, alpha, and theta rhythms before stimulus onset. Therefore, using the recorded EEG signal the EEG phase synchronization can be considered as a good feature for discrimination of the fatigue state.

## 7.5 Conclusions

In this chapter, an auditory oddball task was implemented during the EEG recording. The EEG signal was recorded in two sessions, one at the start of the experiment and the other after the subject had completed a prolonged mental task. The single trial P300 subcomponents were estimated in the infrequent trials. EEG phase synchronization was also estimated around stimulus onset.

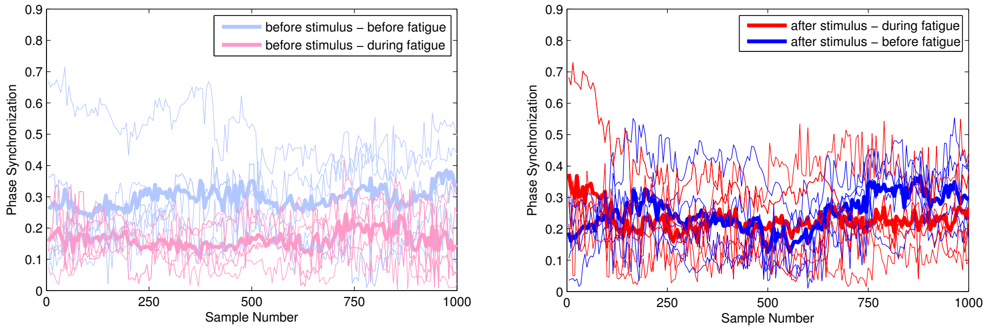

(a) (b)

Figure 7.10: Theta phase synchronization of F3-F4; (a) before stimulus and (b) after stimulus

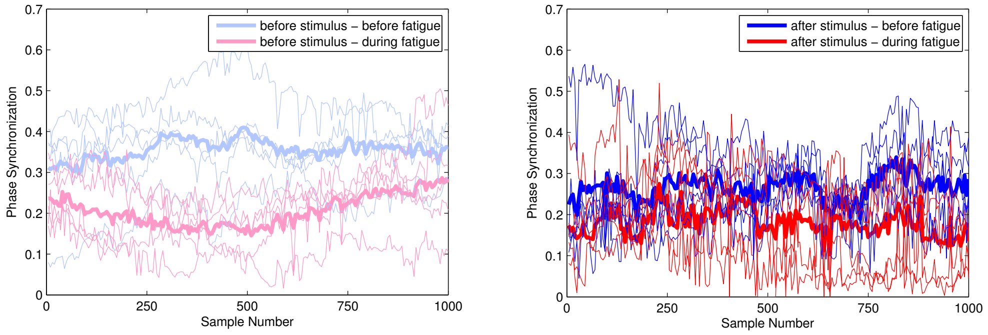

(a) (b)

Figure 7.11: Alpha phase synchronization of C3-C4; (a) before stimulus and (b) after stimulus

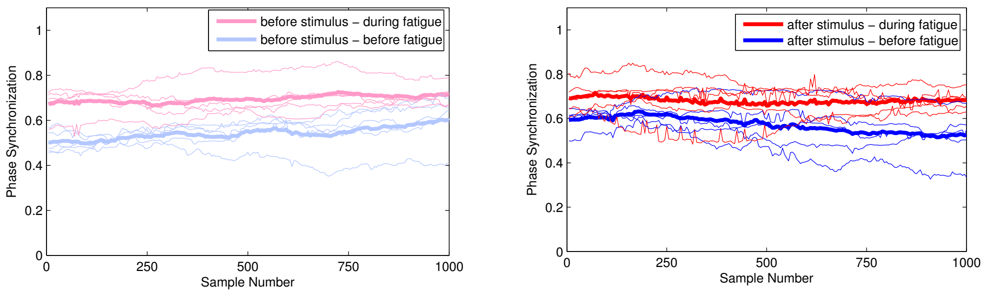

(a) (b)

Figure 7.12: Beta phase synchronization of F3-F4; (a) before stimulus and (b) after stimulus

The results demonstrate the effectiveness of applying the methods for the oddball paradigm which can be considered as a vigilance test for detection of the fatigue state. In addition by applying the proposed methods for spatio-temporal estimation of P300 subcomponents and EEG phase synchronization, the results demonstrate the use of estimated EEG phase synchronization and single trial P300 subcomponents as appropriate and effective features for the analysis and understanding of mental fatigue.

# Chapter 8

# Summary, Conclusions and Future Works

## 8.1 Summary and Conclusions

Over the past decade, there has been increasing scientific interest in detection of mental fatigue state. However the research in mental fatigue analysis using EEG signals has been limited to classical methods whereby simple features from the signals are compared or classified. In addition the analysis of mental fatigue cannot be completed using only one type of biometric. The general strategy in a mental fatigue detection system is to fuse as many features as possible. These features can be obtained from different kinds of input signals (e.g. EEG, ECG) and it is important to extract features which are most relevant. After designing the mental fatigue detection system, an alarming signal may be produced to indicate the warning of the fatigue state and prevent accidents.

In this study, analysis of mental fatigue is conducted by following two important directions. One direction is using EEG signal and extracting its effective features related to EEG phase synchronization. The other direction is using the ERP signal and estimating its parameters in single trials. New methods for each direction have been proposed in this study.

In the traditional methods, average ERP is used for evaluating the changes in the ERP signal before and during fatigue state. However the average ERP does not always correspond to the appearance of mental fatigue since the averaging results in loss of information related to the trial to trial variability of ERPs. The inter-trial variability of ERPs can change in the fatigue state. Therefore, there is an essential need to apply the single trial-based method for estimation of ERPs. In this study, two methods for single trial estimation of ERPs have been proposed. One of them is a temporal method based on RBPF and the other one a spatio-temporal filtering method based on constrained optimization. In the temporal method, tracking of the ERPs in single trials has been considered while in the spatio-temporal filtering method ERPs are estimated in both spatial and temporal domains. In addition, the designed spatio-temporal filtering method has been shown to be robust against both temporal and spatial correlations between the ERP subcomponents.

For analysis of mental fatigue based on EEG signals, classical methods calculate power spectrum of EEG in different frequency bands before and during the fatigue state. To account for non-stationarity of the EEG signals, there is a need for application of the recent adaptive methods which are suitable for analysing non-stationary and non-linear signals. These methods include EMD and ALE. In addition it is beneficial to measure synchronization of the brain activity in different brain regions. EMD and ALE have been proposed for decomposing the EEG signals into their oscillations and then denoising them. The phase synchronization of different EEG oscillations over different parts of the brain are calculated to observe the changes in the fatigue state. In addition, the RBPF was proposed for estimation of instantaneous phase of an EEG oscillation. The method has provided a new insight into the estimation of instantaneous phase which can be extended for measuring phase synchronization in future studies.

The effect of mental fatigue relates to reduced performance and decreased vigilance [119]. Through designing a vigilance test based paradigm it is possible to detect the changes in the vigilance state of the subject during the fatigue state. Auditory reaction time can be used as an objective assessment of vigilance. Therefore, in Chapter 7 an auditory based paradigm has been used. Based on the proposed paradigm, at the beginning of the experiment a vigilance test is taken from the subject using an oddball task. Then, at the end of experiment, when the subject has completed a prolonged mental task, the vigilance test is taken again. The proposed methods have been applied to estimate the single trial P300 subcomponents and the EEG phase synchronization. The results demonstrate the effectiveness of using the auditory oddball paradigm in a mental fatigue detection system.

## 8.2 Future Works

The new methods proposed in this study for estimation of single trial ERPs and EEG phase synchronization can be used for extracting reliable features in a mental fatigue detection system. As it is emphasized in this study, comprehensive analysis of mental fatigue cannot be performed by relying on only few features. In future studies, a classifier or a regression method can be used for online detection of mental fatigue state considering the features that must be obtained by applying the proposed methods in this study and also considering more subjects.

The proposed method in Chapter 4 which combines EMD and RBPF and estimates the instantaneous phase of the EEG oscillation should be further extended in order to estimate the EEG phase synchronization in real time effectively. Since this method uses RBPF with several constraints, the parameters should be selected appropriately and a reasonable number of particles should be used for the method to be applicable in real time situations.

The proposed methods in this thesis can be used for the study of driver fatigue. One of the major causes for driver fatigue based accidents is sleepiness [120]. Since sleepiness or drowsiness reduces the reaction time and as the result the vigilance state of the driver, the suggested auditory paradigm and estimation of ERPs can be used in a driver fatigue detection scenario.

In some research, especially in driver fatigue, different types of fatigue are often considered the same and the drowsiness level of the driver or his/her fatigue state is estimated. However, it is very crucial to distinguish between task-related fatigue and sleep related fatigue by designing appropriate assessment or recording paradigms. For example, in a paradigm for detection of mental fatigue, only mental task related fatigue should be included and for the paradigm in sleepiness detection both sleepiness and mental task effect should be considered. Evaluation of mental fatigue can also depend on subject, age, sex, any possible brain abnormality, recording time, environment, emotional and social engagement, and many other parameters. A robust fatigue monitoring system should indeed take all these factors into account.

# Bibliography

[1] M. A. S. Boksem, T. F. Meijman, and M. M. Lorist. Effects of mental fatigue on attention: an ERP study. *Cognitive Brain Research*, 25:107–116, 2005.

[2] E. Niedermeyer and F. L. Da Silva. *Electroencephalography: Basic principles, clinical applications, and related fields.* Lippincott Williams and Wilkins, 1999.

[3] J. M. Stern and J. Engel. *Atlas of EEG patterns.* Lippincott Williams and Wilkins, 2004.

[4] S. Makeig, A. J. Bell, T. P. Jung, and T. J. Sejnowski. Independent component analysis of electroencephalographic data. *Adv. Neural Inf. Proc. Syst.*, 8:145–151, 1996.

[5] M. M. Ter-Pogossian, M. E. Phelps, E. J. Hoffman, and N. A. Mullani. A positron-emission transaxial tomograph for nuclear imaging (PET). *Radiology*, 114(1):89–98, 1975.

[6] J. W. Belliveau, D. N. Kennedy, R. C. McKinstry, B. R. Buchbinder, R. M. Weisskoff, M. S. Cohen, J. M. Vevea, T. J. Brady, and B. R. Rosen. Functional mapping of the human visual cortex by magnetic resonance imaging. *Science*, 254:716–719, 1991.

[7] J. Clarke and A. I. Braginski. *The SQUID Handbook*, volume 1. Wiley-Vch, 2004.

[8] W. G. Walter and M. A. Camb. The location of cerebral tumours by electro-encephalography. *Lancet*, 228:305–308, 1936.

[9] W. G. Walter and V. J. Dovey. Electro-encephalography in cases of subcortical tumour. *J. Neurol. Neurosurg. Psychiat.*, 7:57–65, 1944.

[10] E. Kirmizi-Alsan, Z. Bayraktaroglu, H. Gurvit, Y. H. Keskin, M. Emre, and T. Demiralp. Comparative analysis of event-related potentials during Go/NoGo and CPT: decomposition of electrophysiological markers of response inhibition and sustained attention. *Brain Res.*, 1104(1):114–128, 2006.

[11] T. Ishihara and N. Yoshii. Multivariate analytic study of EEG and mental activity in juvenile delinquents. *Electroencephalogr. Clin. Neurophysiol.*, 33(1):71–80, 1972.

[12] Y. Mizuki, M. Tanaka, H. Isozaki, H. Nishijima, and K. Inanaga. Periodic appearance of theta rhythm in the frontal midline area during performance of a mental task. *Electroencephalogr. Clin. Neurophysiol.*, 49(3-4):345–351, 1980.

[13] Y. Mizuki. Frontal lobe: mental functions and EEG. *Am. J. EEG Technol.*, 27:91–101, 1987.

[14] G. E. Chatrian, L. Bergamini, and M. Dondey. A glossary of terms most commonly used by clinical electroencephalographers. *Electroencephalogr. Clin. Neurophysiol.*, 37(5):538–548, 1974.

[15] E. Niedermeyer, G. L. Krauss, and C. E. Peyser. The electroencephalogram and mental activation. *Clin. Electroencephalogr.*, 20(4):215–227, 1989.

[16] G. E. Chatrian, M. C. Petersen, and J. A. Lazarte. The blocking of the rolandic wicket rhythm and some central changes related to movement. *Electroencephalogr. Clin. Neurophysiol.*, 11(3):497–510, 1959.

[17] D. Klass and R. Bickford. Observations on the rolandic arceau rhythm. *Electroencephalogr. Clin. Neurophysiol.*, 9:570, 1957.

[18] S. Arroyo, R. P. Lesser, B. Gordon, S. Uematsu, D. Jackson, and R. Webber. Functional significance of the mu rhythm of human cortex: an electrophysiologic study with subdural electrodes. *Electroencephalogr. Clin. Neurophysiol.*, 87(3):76–87, 1993.

[19] G. Pfurtscheller and C. Neuper. Simultaneous EEG 10 Hz desynchronization and 40 Hz synchronization during finger movements. *Neuroreport.*, 3(12):1057–1060, 1992.

[20] G. Pfurtscheller, D. Flotzinger, and C. Neuper. Differentiation between finger, toe and tongue movement in man based on 40 Hz EEG. *Electroencephalogr Clin Neurophysiol.*, 90(6):456–460, 1994.

[21] S. J. Luck. *An Introduction to the Event-Related Potential Technique.* Cambridge, Mass.: The MIT Press, 2005.

[22] J. Polich. Updating P300: an integrative theory of P3a and P3b. *Clin. Neurophysiol.*, 118(10):2128–2148, 2007.

[23] R. Johnson. On the neural generators of the P300 component of the event-related potential. *Psychophysiology*, 30:90–97, 1993.

[24] W. R. Hensyl. *Stedman's Medical Dictionary.* Williams and Wilkins, Baltimore, MD, 25th edition, 1990.

[25] E. Grandjean. *Fitting the Task to the Man. London: Taylor and Francis.*

[26] G. Kecklund and T. Akerstedt. Sleepiness in long distance truck driving: An ambulatory EEG study of night driving. *Ergonomics*, 36:1007–1017, 1993.

[27] K. A. Brookhius and D. D. Waard. The use of psychophysiology to assess driver status. *Ergonomics*, 36(2):1099–1110, 1993.

[28] D. D. Waard and K. A. Brookhius. Assessing driver status: A demonstration experiment on the road. *Accident Analysis and Prevention*, 23:297–307, 1991.

[29] D. F. Dinges. An overview of sleepiness and accidents. *J. Sleep Res.*, 4(S2):4–14, 1995.

[30] M. M. Mitler, M. A. Carskadon, C. A. Czeisler, W. C. Dement, D. F. Dinges, and R. C. Graeber. Catastrophes, sleep and public policy an overview of sleepiness and accidents. *Consensus report. Sleep*, 11:100–109, 1988.

[31] T. A. Dingus, S. G. Klauer, V. L. Neale, A. Petersen, S. E. Lee, J. Sudweeks, M. A. Perez, J. Hankey, D. Ramsey, S. Gupta, C. Bucher, Z. R. Doerzaph, J. Jermeland, and R. R. Knipling. The 100-car naturalistic driving study, phase II results of the 100-Car field experiment (DOT HS 810 593). *Washington, DC: U.S. Department of Transportation, National Highway Traffic Safety Administration*, 2006.

[32] S. Sanei and J. Chambers. *EEG signal Processing.* John Wiley and Sons, 2007.

[33] I. A. Cook, R. O'Hara, S. H. J. Uijtdehaage, M. Mandelkern, and A. F. Leuchter. Assessing the accuracy of topographic EEG mapping for determining local brain function. *Electroencephalogr. Clin. Neurophysiol.*, 107:408–414, 1998.

[34] A. Beyerle E. Eger A. Salek-Haddadi C. Preibisch H. Laufs, A. Kleinschmidt and K. Krakow. EEG-correlated fMRI of human alpha activity. *NeuroImage*, 19:1463–1476, 2003.

[35] R. D. Ogilvie. Physiological review: the process of falling asleep. *Sleep Medicine Reviews*, 5(3):247–270, 2001.

[36] S. K. L. Lal and A. Craig. A critical review of the psychophysiology of driver fatigue. *Biological Psychology*, 55:173–194, 2001.

[37] C. Lafrance and M. Dumont. Diurnal variations in the waking EEG: comparison with sleep latencies and subjective alertness. *J. Sleep Res.*, 9:243–248, 2000.

[38] W. Klimesh. EEG alpha and theta oscillations reflect cognitive and memory performance: a review and analysis. *Brain Res. Rev.*, 29:169–195, 1999.

[39] B. S. Oken and M. Salinsky. Alertness and attention: basic science and electrophysiologic correlates. *J. Clin. Neurophysiol*, 9(4):480–494, 1992.

[40] K. Q. Shen, X. P. Li, W. L. P. M. Pullens, H. Zheng, C. J. Ong, and E. P. V. Wilder-Smith. Key feature extraction for fatigue identification using random forests. *Proceedings of the 27th Annual IEEE Conference on Engineering in Medicine and Biology*, 2005.

[41] A. Muzur, E. F. Pace-Schott, and J. A. Hobson. The prefrontal cortex in sleep. *Electroencephalogr. Clin. Neurophysiol.*, 6:475–481, 2002.

[42] L. Breiman. Random forests. *Machine Learning*, 45:5–32, 2001.

[43] I. Guyon, S. Gunn, A. B. Hur, and G. Dror. Result analysis of the NIPS 2003 feature selection challenge. *Proceedings of the Eighteenth Annual Conference on Neural Information Processing Systems, Vancouver, Canada*, 2004.

[44] K. Q. Shen, C. J. Ong, X. P. Li, Z. Hui, and E. P. V.Wilder-Smith. A feature selection method for multilevel mental fatigue EEG classification. *IEEE Trans. Biomed. Eng.*, 54(7):1231–1237, 2007.

[45] A. V. Oppenheim and R. W. Schafer. *Discrete-Time Signal Processing.* Upper Saddle River, NJ: Prentice-Hall, 1989.

[46] A. Lempel and J. Ziv. On the complexity of finite sequence. *IEEE Transactions on Information Theory*, 22:75–81, 1976.

[47] S. M. Pincus. Approximate entropy as a measure of system complexity. *Proceedings of the National Academy of Science United States of America*, 88:2297–2301, 1991.

[48] I. A. Rezek and S. J. Roberts. Stochastic complexity measures for physiological signal analysis. *IEEE Transactions on Biomedical Engineering*, 45(9):1186–1191, 1998.

[49] J. Liu, C. Zhang, and C. Zheng. EEG-based estimation of mental fatigue by using KPCA-HMM and complexity parameters. *Biomedical Signal Processing and Control, Elsevier*, 5(2):124–130, 2010.

[50] B. Scholkopf, A. J. Smola, and K. R. Muller. Nonlinear component analysis as a kernel eigenvalue problem. *Neural Computation*, 10:1299–1319, 1998.

[51] K. R. Muller, S. Mika, G. Ratsch, K. Tsuda, and B. Scholkopf. An introduction to kernel-based learning algorithms. *IEEE Transactions on Neural Networks*, 12:181–201, 2001.

[52] L. R. Rabiner. A tutorial on hidden markov models and selected applications in speech recognition. *Proceedings of the IEEE*, 77(2):257–286, 1989.

[53] F. Varela, J. P. Lachaux, E. Rodriguez, and J. Martinerie. The brainweb: phase synchronization and large-scale integration. *Nat. Rev. Neurosci.*, 2(4):229–239, 2001.

[54] N. E. Huang, Z. Shen, S. R. Long, M. C. Wu, H. H. Shih, Q. Zheng, N. C. Yen, C. C. Tung, and H. H. Liu. The empirical mode decomposition and hilbert spectrum for nonlinear and non-stationary time series analysis. *Proc Roy Soc London A*, 454:903–995, 1998.

[55] S. Haykin. *Adaptive filter theory.* Prentice-Hall, New Jersey, 2002.

[56] P. Wagner, J. Roschke, J. Fell, and C. Frank. Differential pathophysiological mechanisms of reduced P300 amplitude in schizophrenia and depression: a single trial analysis. *Schizophrenia Research*, 25(3):221–229, 1997.

[57] P. Wagner, J. Roschke, M. Grozinger, and K. Mann. A replication study on P300 single trial analysis in schizophrenia: confirmation of a reduced number of 'true positive' P300 waves. *J. Psychiatr. Res.*, 34(3):255–259, 2000.

[58] S. Cerutti, V. Bersani, A. Carrara, and D. Liberati. Analysis of visual evoked potentials through wiener filtering applied to a small number of sweeps. *J. Biomed. Eng.*, 9(1):3–12, 1987.

[59] W. Truccolo, K. H. Knuth, A. Shah, S. L. Bressler, C. E. Schroeder, and M. Ding. Estimation of single-trial multicomponent ERPs: Differentially variable component analysis (DVCA). *Biol. Cybern.*, 89(6):426–438, 2003.

[60] M. V. Spreckelsen and B. Bromm. Estimation of single-evoked cerebral potentials by means of parametric modeling and kalman filtering. *IEEE Trans. Biomed. Eng.*, 35(9):691–700, 1988.

[61] S. D. Georgiadis, P. O. Ranta-aho, M. P. Tarvainen, and P. A. Karjalainen. Single-trial dynamical estimation of event-related potentials: a kalman filter-based approach. *IEEE Trans. Biomed. Eng.*, 52(8):1397–1406, 2005.

[62] R. M. Chapman and J. W. McCrary. EP component identification and measurement by principal components analysis. *Brain Cogn.*, 27(3):288–310, 1995.

[63] A. C. Tang, B. A. Pearlmutter, N. A. Malaszenko, D. B. Phung, and B. C. Reeb. Independent components of magnetoencephalography: Localization. *Neural Comput.*, 14(8):1827–1858, 2002.

[64] M. Zibulevsky and Y. Y. Zeevi. Extraction of a single source from multichannel data using sparse decomposition. *Neurocomputing*, 49:163–173, 2002.

[65] X. Wang, Y. Chen, and M. Ding. Estimating granger causality after stimulus onset: A cautionary note. *NeuroImage*, 41(3):767–776, 2008.

[66] N. Fogelson, X. Wang, J. B. Lewis, M. M. Kishiyama, M. Ding, and R. T. Knight. Multimodal effects of local context on target detection: evidence from P3b. *J. Cogn. Neurosci.*, 21(9):1680–1692, 2009.

[67] L. Xu, P. Stoica, J. Li, S. L. Bressler, X. Shao, and M. Ding. ASEO: A method for the simultaneous estimation of single-trial event-related potentials and ongoing brain activities. *IEEE Trans. Biomed. Eng.*, 56(1):111–121, 2009.

[68] H. R. Mohseni, K. Nazarpour, E. Wilding, and S. Sanei. Application of particle filters in single-trial event related potential estimation. *Physiological Measurements*, 30(10):1101–1116, 2009.

[69] A. Murata and A. Uetake. Evaluation of mental fatigue in human-computer interaction-analysis using feature parameters extracted from event-related potential. *Proceedings of 10th IEEE International Workshop on Robot and Human Interactive Communication*, pages 630–635, 2001.

[70] A. Murata, A. Uetake, and Y. Takasawa. Evaluation of mental fatigue using feature parameter extracted from event-related potential. *International Journal of Industrial Ergonomics*, 35(8):761–770, 2005.

[71] U. Neumann, P. Ullsperger, H. G. Gille, and M. Pietschann. Effects of graduated processing difficulty on P300 component of the event-related potential. *Psychology*, 194:25–37, 1986.

[72] P. Ullsperger, A. M. Metz, X. Yu, and H. G. Gille. The P300 component of the event-related brain potential and mental effort. *Ergonomics*, 31:1127–1137, 1988.

[73] P. Ullsperger, U. Neumann, H. G. Gille, and M. Pietschann. P300 component of ERP as an index of processing difficulty. *Human Memory and Cognitive Capabilities*, pages 723–731, 1986.

[74] C. Zhang, C. Zheng, X. Yu, and Y. Ouyang. Estimating VDT mental fatigue using multichannel linear descriptors and KPCA-HMM. *EURASIP Journal on Advances in Signal Processing*, 2008:121. (11 pages).

[75] S. Debener, S. Makeig, A. Delorme, and A. K. Engel. What is novel in the novelty oddball paradigm? functional significance of the novelty P3 event-related potential as revealed by independent component analysis. *Cognitive Brain Research*, 22:309–321, 2005.

[76] J. Dien and K. M. Spencer E. Donchin. Localization of the event-related potential novelty response as defined by principal components analysis. *Cognitive Brain Research*, 17(3):637–650, 2003.

[77] A. Goldstein, K. M. Spencer, and E. Donchin. The influence of stimulus deviance and novelty on the P300 and novelty P3. *Psychophysiology*, 39:781–790, 2002.

[78] L. Spyrou, M. Jing, S. Sanei, and A. Sumich. Separation and localisation of P300 sources and their subcomponents using constrained blind source separation. *EURASIP Journal on Advances in Signal Processing*, 2007(1):89. (10 pages).

[79] A. Beauducel and S. Debener. Misallocation of variance in event-related potentials: simulation studies on the effects of test power, topography, and baseline-to-peak versus principal component quantifications. *J. Neurosci. Methods*, 124:103–112, 2003.

[80] A. Beauducel, S. Debener, B. Brocke, and J. Kayser. On the reliability of augmenting/reducing: peak amplitudes and principal components analysis of auditory evoked potentials. *J. Psychophysiol*, 14:226–240, 2000.

[81] J. Dien. Addressing misallocation of variance in principal components analysis of event-related potentials. *Brain Topogr.*, 11:43–55, 1998.

[82] L. Spyrou and S. Sanei. Source localization of event-related potentials incorporating spatial notch filters. *IEEE Trans. Biomed. Eng.*, 55(9):2232–2239, 2008.

[83] M. S. Arulampalam, S. Maskell, N. Gordon, and T. Clapp. A tutorial on particle filters for online nonlinear/non-gaussian bayesian tracking. *IEEE Trans. Signal Processing*, 50(2):174–188, 2002.

[84] A. Doucet. On sequential monte carlo methods for bayesian filtering. *Dept. Eng., Univ. Cambridge, UK, Tech. Rep.*, 1998.

[85] H. T. Su, T. P. Wu, H. W. Liu, and Z. Bao. Rao-blackwellised particle filter based track-before-detect algorithm. *IET Signal Processing*, 2:169–176, 2008.

[86] B. Widrow. Adaptive noise cancellation: Principles and applications. *Proc. IEEE*, 63:1692–1716, 1975.

[87] P. Flandrin, G. Rilling, and P. Goncalves. Empirical mode decomposition as a filter bank. *Proc Roy Soc London A*, 11:112–114, 2004.

[88] J. H. Ahlberg, E. N. Nilson, and J. L. Walsh. *The theory of splines and their applications*. Academic Press, 1967.

[89] G. Rilling, P. Flandrin, and P. Gonalves. On empirical mode decomposition and its algorithms. *Proc. of IEEE-EURASIP Workshop on Nonlinear Signal and Image Processing NSIP03 Grado I*, 3:8–11, 2003.

[90] F. Mormann, K. Lehnertz, P. David, and C. Elger. Mean phase coherence as a measure for phase synchronization and its application to the EEG of epilepsy patients. *Physica D*, 144:358–369, 2000.

[91] R. Q. Quiroga, A. Kraskov, T. Kreuz, and P. Grassberger. Performance of different synchronization measures in real data: A case study on electroencephalographic signals. *Phys. Rev. E*, 65, 2002.

[92] M. M. Lorist, M. A. S. Boksem, and K. R. Ridderinkhof. Impaired cognitive control and reduced cingulate activity during mental fatigue. *Cognitive Brain Research*, 24:199–205, 2005.

[93] M. M. Lorist, M. Klein, S. Nieuwenhuis, R. De Jong, G. Mulder, and T. M. Meijman. Mental fatigue and task control: planning and preparation. *Psychophysiology*, 37(5):614–625, 2000.

[94] Y. Kopsinis and S. McLaughlin. Development of EMD-based denoising methods inspired by wavelet thresholding. *IEEE Trans. Signal Processing*, 57(4):1351–1362, 2009.

[95] *Programs for Digital Signal Processing.* IEEE Press, New York, dsp committee ed. edition, 1979.

[96] D. Jarchi, B. Makkiabadi, and S. Sanei. Estimation of trial to trial variability of P300 subcomponents by coupled Rao-Blackwellised particle filtering. *Proceedings of 15th IEEE/SP Workshop on Statistical Signal Processing*, pages 17–20, 2009.

[97] D. Jarchi, B. Makkiabadi, and S. Sanei. Separating and tracking ERP subcomponents by constrained particle filtering. *Proceedings of 16th International Conference on Digital Signal Processing*, pages 75–80, 2009.

[98] A. Dogandzic and A. Nehorai. Estimating evoked dipole responses in unknown spatially correlated noise with EEG/MEG arrays. *IEEE Trans. Signal Processing*, 48(1):13–25, 2000.

[99] M. Scherg and D. V. Cramon. Two bilateral sources of the late AEP as identified by a spatio-temporal dipole model. *Electroencephalogr. Clin. Neurophysiol.*, 62(1):32–44, 1985.

[100] J. Polich and J. R. Criado. Neuropsychology and neuropharmacology of P3a and P3b. *International Journal of Psychophysiology*, 60:172–185, 2006.

[101] R. Desimone, E. Miller, L. Chelazzi, and A. Lueschow. Multiple memory systems in the visual cortex. *In: The Cognitive Neurosciences, M. Gazzaniga (Ed.)*, pages 475–486, 1995.

[102] R. Knight. Contribution of human hippocampal region to novelty detection. *Nature*, 383:256–259, 1996.

[103] R. Li, J. C. Principe, M. Bradley, and V. Ferrari. A spatiotemporal filtering methodology for single-trial ERP component estimation. *IEEE Trans. on Biomed. Eng.*, 56(1):83–92, 2009.

[104] W. Freeman. *Mass Action in the Nervous System.* New York: Academic, 1975.

[105] K. Fukunaga. *Introduction to Statistical Pattern Recognition.* second ed. Academic Press, 1990.

[106] I. T. Jolliffe. *Principal component analysis.* Springer-Verlag, 1986.

[107] R. Kramer. Chemometric techniques for quantitative analysis. *CRC Press*, 1998.

[108] J. Dien, W. Khoe, and G. R. Mangun. Evaluation of PCA and ICA of simulated ERPs: Promax vs. infomax rotations. *Hum. Brain Mapp.*, 28(8):742–763, 2007.

[109] J. Dien. Addressing misallocation of variance in principal components analysis of event-related potentials. *Brain Topogr.*, 11(1):43–55, 1998.

[110] H. F. Kaiser. The varimax criterion for analytic rotation in factor analysis. *Psychometrika*, 23:187–200, 1958.

[111] A. E. Hendrickson and P. O. White. Promax: a quick method for rotation to orthogonal oblique structure. *British Journal of Statistical Psychology*, 17:65–70, 1964.

[112] A. J. Bell and T. J. Sejnowski. An information-maximisation approach to blind separation and blind deconvolution. *Neural Computation*, 7:1129–1159, 1995.

[113] J. Dien. Evaluating two-step PCA of ERP data with geomin, infomax, oblimin, promax, and varimax rotations. *Psychophysiology*, 47(1):170–183, 2010.

[114] J. C. Mosher, R. M. Leahy, and P. S. Lewis. EEG and MEG: forward solutions for inverse methods. *IEEE Trans. Biomed. Eng.*, 46(3):245–259, 1999.

[115] *BrainStorm, Matlab Toolbox [Online]. Available: http://neuroimage.usc.edu/brainstorm/.*

[116] J. Dien. The ERP PCA toolkit: An open source program for advanced statistical analysis of event-related potential data. *J. Neurosci. Methods*, 187(1):138–145, 2010.

[117] A. Delorme and S. Makeig. EEGLAB: An open source toolbox for analysis of single-trial EEG dynamics including independent component analysis. *J. Neurosci. Methods*, 134(1):9–21, 2004.

[118] B. Karoumi, A. Laurent, F. Rosenfeld, T. Rochet, A. M. Brunon, J. Dalery, T. d'Amato, and M. Saoud. Alteration of event related potentials in siblings discordant for schizophrenia. *Schizophr. Res.*, 41(2):325–334, 2000.

[119] E. A. Schmidt, M. Schrauf, M. Simon, M. Fritzsche, A. Buchner, and W. E. Kincses. Drivers' misjudgement of vigilance state during prolonged monotonous daytime driving. *Accid. Anal. Prev.*, 41(5):1087–1093, 2009.

[120] M. Simon, E. A. Schmidt, W. E.Kincses, M. Fritzsche, A. Bruns, C. Aufmuth, M. Bogdan, W. Rosenstiel, and M. Schrauf. EEG alpha spindle measures as indicators of driver fatigue under real traffic conditions. *Clin. Neurophysiol.*, 122(6):1168–1178, 2011.